

Space Science Reviews \_\_\_\_\_  
<https://doi.org/10.1007/s11214-021-00839-2>

# Pre-flight Calibration and Near-Earth Commissioning Results of the Mercury Plasma Particle Experiment (MPPE) Onboard MMO (Mio)

Yoshifumi Saito · Dominique Delcourt · Masafumi Hirahara · Stas Barabash · Nicolas André · Takeshi Takashima et al. *[full author details at the end of the article]*

Received: 17 June 2020 / Accepted: 19 June 2021  
© The Author(s), under exclusive licence to Springer Nature B.V. 2021

## Abstract

BepiColombo Mio (previously called MMO: Mercury Magnetospheric Orbiter) was successfully launched by Ariane 5 from Kourou, French Guiana on October 20, 2018. The Mercury Plasma/Particle Experiment (MPPE) is a comprehensive instrument package onboard Mio spacecraft used for plasma, high-energy particle and energetic neutral atom measurements. It consists of seven sensors including two Mercury Electron Analyzers (MEA1 and MEA2), Mercury Ion Analyzer (MIA), Mass Spectrum Analyzer (MSA), High Energy Particle instrument for electron (HEP-ele), High Energy Particle instrument for ion (HEP-ion), and Energetic Neutrals Analyzer (ENA). Significant efforts were made pre-flight to calibrate all of the MPPE sensors at the appropriate facilities on the ground. High voltage commissioning of MPPE analyzers was successfully performed between June and August 2019 and in February 2020 following the completion of the low voltage commissioning in November 2018. Although all of the MPPE analyzers are now ready to begin observation, the full service performance has been delayed until Mio's arrival at Mercury. Most of the fields of view (FOVs) of the MPPE analyzers are blocked by the thermal shield surrounding the Mio spacecraft during the cruising phase. Together with other instruments on Mio including Magnetic Field Investigation (MGF) and Plasma Wave Investigation (PWI) that measure plasma field parameters, MPPE will contribute to the comprehensive understand-

---

The BepiColombo mission to Mercury  
Edited by Johannes Benkhoff, Go Murakami and Ayako Matsuoka

---

BepiColombo Mio/MPPE Team: Y. Saito, M. Hirahara, S. Barabash, D. Delcourt, A. Coates, N. André, T. Takashima, K. Asamura, C. Aoustin, J.-A. Sauvaud, P. Louarn, M. Blanc, C. Jacquy, C. Mazelle, I. Dandouras, V. Genot, D. Toubanc, C. Peymirat, A. Fedorov, E. Amata, R. Bruno, M.B. Cattaneo, G. Consolini, M.F. Marcucci, Z. Němeček, B. Lavraud, L. Griton, S. Aizawa, H.-C. Seran, J. Rouzaud, Q.M. Lee, E. Le Comte, E. Penou, M. Petiot, D. Moirin, S. Machida, I. Shinohara, W. Miyake, T. Terasawa, C. Owen, A. Fazakerley, T. Nagatsuma, K. Seki, T. Nagai, A. Ieda, H. Hasegawa, J.-M. Illiano, J.-J. Berthelier, D. Fontaine, N. Krupp, J. Woch, S. Yokota, M. Fraenz, H. Krueger, H. Michalik, L. Hadid, R. Modolo, B. Fiethe, B. Ktra, F. Leblanc, C. Verdel, H. Fischer, J.-D. Techer, D. Reisenfeld, R. Elphic, H. Funsten, D. McComas, M. Grande, H. Matsumoto, T. Yanagimachi, T. Obara, Y. Miyoshi, Y. Ebihara, M. Nose, F. Tsuchiya, T.A. Fritz, Q. Zong, T. Mitani, S. Kasahara, M. Shimoyama, Y. Kazama, M. Yamauchi, M. Holmström, Y. Futaana, R. Lundin, P. Wurz, M. Wieser, H. Andersson, S. Karlsson, W. Benz, W.-H. Ip, L.-N. Hau, M. Hoshino, M. Fujimoto, K. Maezawa, N. Terada, P. Trávníček, R. Smets, R. Modolo, F. Leblanc, R. Lallemand, L. Zelenyi, H. Malova, M.N. Nishino, Y.-C. Wang, M. Oka, M. Yagi, Y. Harada, L. Xie, J. Zhong, J. Vaverka, K. Keika, W. Sun, L. Wang

ing of the plasma environment around Mercury when BepiColombo/Mio begins observation after arriving at the planet Mercury in December 2025.

**Keywords** Mercury · Magnetosphere · Solar wind · Exosphere · Ion · Electron · Energetic neutral atom

## 1 Introduction

Our knowledge of Mercury’s plasma environment has significantly increased during the past decade owing to new observations made by the Mercury orbiter MESSENGER. However, many questions remain. To provide greater detail on this plasma environment, BepiColombo Mio was successfully launched by Ariane 5 from Kourou, French Guiana on October 20, 2018 as part of a joint mission between European Space Agency (ESA) and Institute of Space and Astronautical Science/Japan Aerospace Exploration Agency (ISAS/JAXA).

When BepiColombo Mission began about 15 years ago, Mercury was one of the least explored planets of our solar system. No spacecraft had visited Mercury since Mariner 10 made three fly-bys past the planet in 1974 and 1975. Mariner 10 discovered that Mercury possesses an intrinsic magnetic field with very weak intensity compared with that of other magnetized planets in our solar system (Ness et al. 1974; Ogilvie et al. 1974). About 30 years after Mariner 10 visited Mercury, MESSENGER made its first fly-by observation in 2008. In 2011, MESSENGER was inserted into Mercury’s orbit to become the world’s first Mercury orbiter, which continued observation for more than four years.

Mariner 10 discovered the dominance of the dipole term in the spherical harmonic expansion of Mercury’s magnetic field. This suggests that the interaction between the solar wind and Mercury’s magnetosphere should be “Earth-like”, in contrast to the cases of Mars and Venus in which the planetary magnetic fields have negligible intensity or have only local effects on the interaction. The MESSENGER observation revealed that the dipole moment of Mercury is deviated from its center northward by about 20% of the planet’s radius (Anderson et al. 2011). Because the magnetic field reflects the internal structure and its dynamics, detailed observation of Mercury’s magnetic field is one of the most important targets of BepiColombo.

Mercury’s small size and low gravity result in environmental characteristics that differ significantly from those of Earth. MESSENGER clearly showed the extremely dynamic behavior of Mercury’s magnetosphere where substorm-like phenomena repeat with very short time scales (Imber and Slavin 2017). MESSENGER also proved the existence of large amounts of heavy elements in the magnetosphere (Zurbuchen et al. 2011). BepiColombo/Mio will make exhaustive measurements of Mercury’s magnetosphere including comprehensive measurements of plasma and particles. Such observation of plasma and particles from spinning spacecraft covering a  $4\pi$  FOV with a time resolution as high as a few seconds will reveal the mechanism of the substorm-like phenomena occurring in Mercury’s magnetosphere to clarify similarity and difference between Earth and Mercury. In addition, the ion energy mass spectrometer on Mio has high mass resolution that can distinguish between the species of planetary heavy ions. This will help to explain the contribution of heavy ions on the magnetospheric processes in Mercury’s magnetosphere.

The Mercury Plasma/Particle Experiment (MPPE) is a comprehensive instrument package used for plasma, high-energy particle and energetic neutral atom measurements. It consists of seven sensors including two Mercury Electron Analyzers (MEA1 and MEA2), Mercury Ion Analyzer (MIA), Mass Spectrum Analyzer (MSA), High Energy Particle instrument for electron (HEP-ele), High Energy Particle instrument for ion (HEP-ion), and Energetic Neutrals Analyzer (ENA).

101 Together with other instruments onboard Mio including Magnetic Field Investigation  
102 (MGF) and Plasma Wave Investigation (PWI) that measure plasma field parameters, MPPE  
103 will contribute to the comprehensive understanding of the plasma environment around Mer-  
104 cury when BepiColombo/Mio begins observation after arriving at the planet Mercury in  
105 December 2025.

106

107

## 108 **2 Science Objectives of MPPE**

109

### 110 **2.1 Structure, Dynamics, and Physical Processes Occurring in Mercury's** 111 **Magnetosphere**

112

113 Because the intrinsic magnetic field is weaker and the dynamic pressure of the solar wind  
114 is stronger at Mercury than at Earth, solar wind can sometimes directly interact with the  
115 dayside planetary surface in the low-latitude region. Recent MESSENGER observations  
116 indicate that the high dynamic pressure of the solar wind causes the compression and mag-  
117 netic flux transfer by reconnection, which can completely erode the dayside magnetosphere  
118 (Slavin et al. 2019). Even when the solar wind dynamic pressure is not so strong, the solar  
119 wind plasma can directly penetrate until reaching the planetary surface through the cusp  
120 regions. Another important characteristic of Mercury's magnetic field is the offset of the  
121 dipole. The fly-bys by Mariner 10 suggested the possibility of northward offset of the mag-  
122 netic dipole by  $0.2 R_M$  (Whang 1977), which was confirmed by MESSENGER observations  
123 (Anderson et al. 2011). This means that the planetary magnetic field at the surface is stronger  
124 at the northern pole than at the southern pole, and that the solar wind plasma can more easily  
125 access the planetary surface in the southern polar region. In addition, heavy ions and neutrals  
126 sputtered from the planetary surface are major observation targets of MPPE. The effects of  
127 the direct interaction of the space plasma and the planetary surface on the remaining plane-  
128 tary processes can be investigated only in Mercury's environment.

129 Despite the qualitative similarities of the global structures of the Mercury and Earth mag-  
130 netospheres, many differences remain between them. The small dimensions of Mercury's  
131 magnetosphere imply short time scales of the dynamic phenomena occurring therein. The  
132 magnetospheric convection, potentially driven by dayside reconnection, is expected to com-  
133 plete its circulation within just a few minutes, which is only  $1/30$  of the corresponding time  
134 scale at Earth (e.g., Slavin 2004). Flux transfer events (FTEs) are frequently detected in  
135 rapid succession at Mercury's magnetopause with much shorter time scales than those at  
136 Earth (Slavin et al. 2012; Imber et al. 2014). The small magnetosphere also implies that  
137 kinetic behavior of plasma is particularly important. Because the typical scale of Mercury's  
138 magnetospheric structures are on the order of the proton Larmor radius, the ideal mag-  
139 netohydrodynamics (MHD) approximation could be inadequate for describing the global  
140 dynamics of the magnetosphere. This is exemplified by MESSENGER observations, which  
141 showed that a typical proton gyroradius in Mercury's plasma sheet is  $\sim 380$  km (DiBraccio  
142 et al. 2015) and that the thickness of the plasma sheet is comparable to the proton gyroradi-  
143 us (Sun et al. 2017). For zero or weak guide magnetic fields, ion scale current sheets with  
144 a thickness comparable to the ion inertia length or the ion Larmor radius are predicted to  
145 become highly unstable for the current driven instabilities, which lead to quick triggering of  
146 magnetic reconnection (Shinohara and Fujimoto 2005).

147 Many questions remain about the substorms in Mercury's magnetosphere. Because the  
148 concept of storage and sudden release of energy is likely universal, efforts to answer these  
149 questions enable us to examine the ubiquitous problems of magnetized plasmas. One of  
150 these questions is related to the dawn-dusk asymmetry in the plasma sheet associated with

substorm activities (Sun et al. 2017). In particular, proton energization and heating through substorm activities occur more often on the dawnside than on the duskside, which is opposite that occurring in Earth's magnetosphere. The cause of the dawn-dusk asymmetry remains to be studied using BepiColombo data. The questions related to the Mariner 10 observation events such as drift echoes have been considered in the context of substorms. These particle phenomena need to be studied with an unbiased attitude and a complete field of view. Specifically, all substorm-like events at Mercury should be studied in the context of solar wind-magnetosphere interaction and particle acceleration processes. In this context, measurements such as those by MPPE will be of paramount importance.

Recent theoretical studies suggest that efficient plasma transport can be achieved within highly rolled-up vortices that form owing to the velocity shear at the tail-flank boundary (Hasegawa et al. 2004; Nakamura et al. 2017). It is widely accepted that Kelvin–Helmholtz (K-H) instability operates at Earth's magnetopause and plays a significant role in transporting mass and energy from the solar wind to the magnetosphere. MESSENGER observations showed that K-H vortices develop predominantly on the duskside (Gershman et al. 2015). K-H waves as sources of these vortices are also detected mainly at dusk (Liljeblad et al. 2014). A possible contribution of heavy ions to K-H instability will be explored by analyzing the BepiColombo data.

The study of large amplitude electromagnetic waves around the magnetopause is also important in terms of particle transport, diffusion and acceleration. Anisotropic particle distribution and accelerated particle beams can excite various electromagnetic waves. The mapping of characteristic waves and particle velocity distribution functions, and their comparison with those found on other planets are also important.

The existence of Na ions in Mercury's magnetosphere is another interesting factor. The heavy mass of these ions combined with the weak magnetic field result in large Larmor radii in the Mercury magnetosphere. The turbulence discussed here is basically of MHD nature but the large Larmor radius is comparable to the scale of the vortices and efficient heating of Na ions by turbulence is expected. Heated Na ions carry non-negligible pressure and thus play a role in determining the shape and dynamics of the magnetosphere (Gershman et al. 2014). Such a significant contribution of heavy ions would be an analog to large storms in Earth's magnetosphere although this could be the average state of the Mercury magnetosphere. Comprehensive observations of both the tail-flank turbulence and the large-scale convection powered by the reconnection in the small-scale magnetosphere are thus quite interesting from the perspectives of basic magnetohydrodynamics and magnetospheric physics. MPPE includes required plasma detectors with good time resolution and a mass spectrometer with sufficiently wide energy coverage.

The energization mechanism of magnetospheric plasma at Mercury has been unsolved since the Mariner 10 era. Although intense bursts of energetic charged particles  $> 35$  keV likely associated with substorm activities have been detected by Mariner 10 (Simpson et al. 1974), their species, flux, and energy spectrum for the events were not precisely determined owing to instrument limitations. Recent observations by EPS onboard MESSENGER revealed that the bursts of energetic charged particles are composed of high-energy electrons (Ho et al. 2011). This finding combined with the indications of MESSENGER/GRNS data suggest that the major components of the energetic bursts are electrons of several tens to  $\sim 100$  keV (Slavin et al. 2018). Although the most plausible mechanism of the electron energization is magnetic reconnection in Mercury's magnetotail associated with substorm activities, the lack of low-energy electron observations by MESSENGER prevents us from making a conclusion on this topic. However, observations of electrons in a wide energy range by MPPE and other instruments will enable us to identify the generation mechanisms of the high-energy electrons around Mercury.

## 2.2 Interaction Among Magnetosphere, Exosphere, Surface, and Interior of Mercury

The Mercury environment can be characterized by complicated interaction among the surface, exosphere, and magnetosphere (Milillo et al. 2005). The lack of a thick atmosphere allows the space plasma to directly reach the surface. The surface materials are then ejected into space to form the exosphere, part of which is ionized and governed by the electromagnetic environment of Mercury or magnetosphere. This complex system occurs in all objects in the Solar System with no atmosphere. In particular, the Moon provides an appropriate environment for understanding this coupling (e.g., Futaana et al. 2018). Although it does not have a global magnetic field, the Moon's lack of atmosphere and strong ionosphere affects the plasma-surface interaction, exosphere formation, and interaction with the upstream plasma. However, part of the Moon is magnetized where the dynamic plasma physics is in operation. Recent measurements of the Moon by several orbiters and fly-bys (e.g., Nozomi, Lunar Prospector, Kaguya, Chang'E, Chandrayaan-1, ARTEMIS, and LADEE) have significantly increased our knowledge of the lunar environment, part of which can be applied to understand these interactions at Mercury.

Mercury's surface releases Na, O, H, He, K, Ca, and possibly other compositions by photon-stimulated desorption, thermal desorption, micrometeoritic impacts, chemical sputtering, and ion sputtering, to form a highly extended tenuous atmosphere or exosphere. The exosphere of Mercury will be investigated by instruments on MPO with a relatively lower orbiting altitude. However, the exospheric ions circulate along the convection of the magnetosphere and then partially re-enter Mercury's surface-exosphere system to further sputter the surface material. Conversely, the exospheric ions affect the magnetospheric convection. These facts indicate that Mercury's exosphere is not a single system, rather it strongly interacts with other regions, constituting a surface-exosphere-magnetosphere system. Among the release processes, ion sputtering is mostly related to magnetospheric processes. As a result of magnetospheric dynamics, the magnetospheric and solar wind ions precipitate on Mercury's surface resulting in atom and ion sputtering (Killen et al. 2001). The sputtered ions and exospheric photoions feed the magnetosphere, which affects its dynamics.

Ions originating directly from solar wind, those accelerated in the tail, and energized planetary ions, all precipitate onto Mercury's surface, which results in extensive sputtering (Grande 1997; Wurz and Lammer 2003; Mura et al. 2009). No reservoir of trapped particles exists near Mercury because the planet occupies a large portion of its inner magnetosphere; in this case, accelerated energetic particles hit the surface easily and become lost quickly (Delcourt et al. 2003; Yagi et al. 2017). The Mercury magnetosphere does not include a ring current region such as that present in Earth's inner magnetosphere which enables quasi-trapped Na ions to exist in the low-latitude region near the planet as indicated by simulation (Yagi et al. 2010) and MESSENGER observation (Schriver et al. 2011). The energetic particles in the magnetosphere should precipitate to the planetary surface/exosphere directly through pitch angle scattering by wave-particle interactions and field line curvature. The sputtering by particle precipitation is an escape process of heavy ions from the planetary surface: the direct interaction of precipitating particles with the planetary surface is important for the evolution of particle circulation in the Mercury magnetosphere (Ip 1986). Therefore, investigation of the loss processes of high-energy particles and the relationship between the energetic particle and the planetary surface is also an important objective of the MPPE observations. The integrated energy spectrum of the sputtered products falls off as  $E^{-2}$ , reflecting the Thompson-Sigmund formula (e.g., Sigmund et al. 1982) and results in relatively high fluxes at energies greater than 10–100 eV (Masseti et al. 2003). Measuring these low-energy neutral atoms (LENA) by MPPE-ENA while monitoring precipitating ions

251 by MPPE-MSA and MPPE-MIA are crucial for understanding the contribution of sputtering  
252 to the formation of Mercury's exosphere, which reveals dynamical and spatial variations of  
253 the sputtering source (Fatemi et al. 2020).

254 In addition to magnetosphere-exosphere coupling, MESSENGER observation revealed  
255 a possible magnetosphere-exosphere-interior system. The MESSENGER/MAG observation  
256 provided evidence of field aligned currents (FACs) at Mercury, where a weak Region 1  
257 current system exists but no Region 2 current does (Anderson et al. 2014). The existence  
258 of a Region 1 current system suggests the possibility of electric current closure through  
259 conductive material at the depth of the outer core, which strongly depends on the electric  
260 conductivity at the planet's surface and interior region. Direct measurement of FAC carriers  
261 by MPPE is highly anticipated. In addition, the balance between the magnetic reconnec-  
262 tion and induction at the dayside magnetopause could provide clues for understanding the  
263 planetary interior (Heyner et al. 2016).

264 The dynamic response of the Mercury magnetosphere to solar wind variation is some-  
265 times regarded as a possible explanation for the variability in the Na exosphere both spatially  
266 and temporally on timescales less than one day as observed by ground-based remote sensing  
267 measurement. Model calculations show that solar wind ions and the exospheric ions ener-  
268 gized in the magnetosphere very non-uniformly affect Mercury's surface, which includes  
269 various impact regions such as auroral impact, cusp impact, and nose impact regions (Kallio  
270 and Janhunen 2003; Delcourt et al. 2003). However, such calculations also indicate that the  
271 impact regions and the effects of ion flux are rather sensitive to the magnetospheric dynam-  
272 ics and particle environment. MESSENGER discovered an X-ray aurora accompanied by  
273 electron precipitation (Lindsay et al. 2016; Dewey et al. 2017). Observation of precipitat-  
274 ing electrons by MPPE-MEA and MPPE-HEP-ele will also contribute to understanding the  
275 magnetosphere-exosphere coupling.

276 The highly eccentric orbit of Mercury generates significant variation in the planetary en-  
277 vironment between the perihelion and aphelion. Recent MESSENGER observations have  
278 shown that the Na exosphere is surprisingly constant in terms of annual variation, with no  
279 strong episodic variation or surface dependence noted (Cassidy et al. 2015). However, the Na  
280 intensity showed a strong seasonal variation that contradicts previous ground-based observa-  
281 tion reported by Leblanc and Johnson (2010). The ionization frequencies of the exospheric  
282 neutrals by photoionization, electron impact ionization, and charge exchange interaction,  
283 which depend on the solar flux and the solar wind density and velocity, vary by a factor  
284 of two. These differences can cause a significant alteration of the dynamics of Mercury's  
285 magnetosphere-exosphere-surface-interior system. To understand this system, it is neces-  
286 sary to observe the planet's particle environment by MPPE observation for at least a few  
287 Mercury years.

### 288 2.3 Shocks and the Inner Heliosphere

289 A new era of inner heliosphere exploration began with the launch of the Parker Solar Probe  
290 in 2018 (Fox et al. 2016), followed by that of the Solar Orbiter in 2020 (Müller et al. 2013).  
291 Mio will play an important role in this heliosphere-wide, multi-mission exploration by its  
292 placement in Mercury's orbit. Following the successes of other missions such as Helios  
293 1 and 2 in the 1980s, MESSENGER in 2008–2015, and the recent Parker Solar Probe,  
294 Mio is expected to achieve comprehensive in-situ measurement of plasmas in the inner-  
295 heliosphere by taking advantage of the spin-stabilized configuration of the spacecraft and a  
296 suite of modern instruments. Mio is expected to make a wide range of discoveries regarding  
297 collisionless shocks, solar wind, pickup ions of interstellar-origin, solar energetic particles  
298 (SEPs), the modulation of galactic cosmic rays and other phenomena.

300

301 Particles are accelerated to very high, non-thermal energies at astrophysical shocks, as  
302 evidenced by emission from astrophysical sources such as supernova remnants, extragalactic  
303 jets, and galaxy clusters. Particles are also accelerated at shocks in space such as planetary  
304 bow shocks and interplanetary shocks. In-situ measurement of shocks in various plasma en-  
305 vironments is thus crucial for understanding of the generality and scaling-law of particle  
306 acceleration at shocks. Mercury is unique in that it is closer than any other planet to the Sun.  
307 Thus its orbit offers the greatest chance of detecting very fast interplanetary shocks particu-  
308 larly in extreme cases of solar eruptive events such as coronal mass ejection (CME) and  
309 solar flares. The shock speed can reach up to 4000 km/s and the Alfvén Mach number can  
310 exceed several tens in value, as demonstrated combined observations and modeling (Smart  
311 and Shea 1985; Cliver et al. 1990). In fact, statistical analysis of MESSENGER data has  
312 confirmed that the shock transit speed is substantially higher in Mercury’s orbit (Winslow  
313 et al. 2015) than that of Earth, which is consistent with earlier reports (Wang et al. 2005).  
314 Therefore, MPPE data combined with information obtained from other instruments on Mio  
315 will likely provide opportunities to study high-speed and/or high-Mach-number shocks well  
316 before they are substantially decelerated.

317 A key point in this research is that previously observed features of particle acceleration at  
318 shocks are often inconsistent with the standard diffusive shock acceleration (DSA) scenario.  
319 In DSA, the particle flux increases exponentially prior to the arrival of the shock, reaches  
320 its maximum at the shock front, and exhibits a power law with the power-law index as a  
321 function of the compression ratio only. In reality, however, shocks often do not exhibit a  
322 significant flux increase and, even if they are present, the power-law index does not match  
323 that predicted from the observed compression ratio. Such discrepancies have been reported  
324 for both ion acceleration (e.g., van Nes et al. 1984; Lario et al. 2003; Desai et al. 2004;  
325 Lario 2005; Fisk and Gloeckler 2012) and electron acceleration (Shimada et al. 1998; Ho  
326 et al. 2008). Moreover, for electrons, pre-energizing to non-thermal energies is required  
327 for the DSA process to begin, although the precise mechanism of such a process remains  
328 unclear (e.g., Tsurutani and Lin 1985; Oka et al. 2019; Amano et al. 2020). To address these  
329 problems, MPPE will provide comprehensive analyses of ion/electron velocity and pitch-  
330 angle distributions, associated waves and turbulence, ion composition, and ion charge states  
331 before, during and after shock/CME passages.

332 The bow shock and magnetosheath signatures in Mercury’s orbit are important targets of  
333 BepiColombo. The solar wind flow in Earth’s orbit is usually super-Alfvénic with typical  
334 Alfvén Mach numbers of  $5 < M_A < 10$ . According to the standard solar wind model by  
335 Parker (1958), the Alfvén Mach number in Mercury’s orbit is statistically lower than that in  
336 Earth’s orbit (e.g., Slavin et al. 2018). We expect to detect super-Alfvénic solar wind with  
337 very low  $M_A$  ( $1 < M_A < 2$ ) and sub-Alfvénic solar wind ( $M_A < 1$ ) in Mercury’s orbit be-  
338 cause BepiColombo will arrive at Mercury in 2025 when the solar activity is likely to be at  
339 its peak in Solar Cycle 25. For the bow shock under the lower but still super-Alfvénic solar  
340 wind ( $M_A > 1$ ), the MESSENGER mission has already revealed significantly smaller mag-  
341 netic “overshoots” (i.e., intensifications of the magnetic field magnitude within the shock  
342 transition layer) at Mercury’s bow shock compared with that at Saturn (Masters et al. 2014).  
343 The differences in overshoot structure of the bow shocks is consistent with the expectations,  
344 which demonstrates the applicability of the scaling law based on the solar wind model. In ad-  
345 dition, the lower  $M_A$  solar wind yields unusual interaction between the magnetosheath and  
346 the magnetosphere, that depends strongly on the direction of the interplanetary magnetic  
347 field (IMF) (Lavraud and Borovsky 2008; Nishino et al. 2008). If the solar wind becomes  
348 sub-Alfvénic, the bow shock will alter to a slow-mode shock, and its shape and structure  
349 could differ significantly from that normally expected for a fast-mode bow shock (Hund-  
350 hausen et al. 1987). An irregular bow shock can be detected by comparing the data with

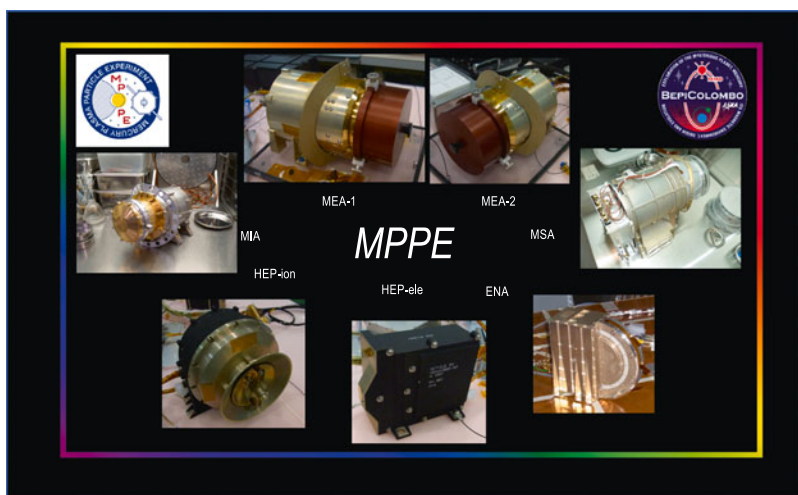


Fig. 1 Photo of the seven MPPE sensors

the typical shape/location of the bow shock established by MESSENGER (Winslow et al. 2013). Another candidate for sub-Alfvénic interaction of Mercury’s magnetosphere with the extreme solar wind is the formation of Alfvén wings (Sarantos and Slavin 2009), which can be compared with sub-Alfvénic interaction of the Galilean moons with Jupiter’s magnetosphere.

### 3 Instrument Description and Pre-flight Calibration

#### 3.1 Overview of MPPE Instrument Suite

##### 3.1.1 MPPE Instrument Suite for Plasma/Particle Measurements

As illustrated in Fig. 1, the MPPE suite is a comprehensive instrument package developed to achieve the scientific objectives described in Sect. 2. As previously discussed, it consists of seven sensors including MEA1, MEA2, MIA, MSA, HEP-ele, HEP-ion, and ENA (Saito et al. 2010a). These sensors measure plasma, high-energy particles and energetic neutral atoms with sufficiently high time resolution, wide energy and dynamic ranges, wide angle coverage, and high mass resolution.

Specifically, MEA1 and MEA2 measure the 3D phase space density of low energy electrons between 3 eV and 26 keV and were developed by the Research Institute in Astrophysics and Planetology (IRAP) in France. MIA measures 3D phase space density of low energy ions between 15 eV/q and 29 keV/q and was developed by ISAS/JAXA in Japan. MSA measures the mass identified 3D phase space density of low energy ions between 1 eV/q and 38 keV/q and was developed by the Laboratory of Plasma Physics (LPP) in France, the Max Planck Institute for Solar System Research (MPS) and Institute of Computer and Network Engineering (IDA)/Technical University of Braunschweig in Germany and ISAS/JAXA in Japan. HEP-ele and HEP-ion measure the energy spectra of high energy electrons between 30 keV and 700 keV and the mass identified ion energy spectra of high energy ions between 30 keV and 1.5 MeV, respectively, and were developed by Institute for

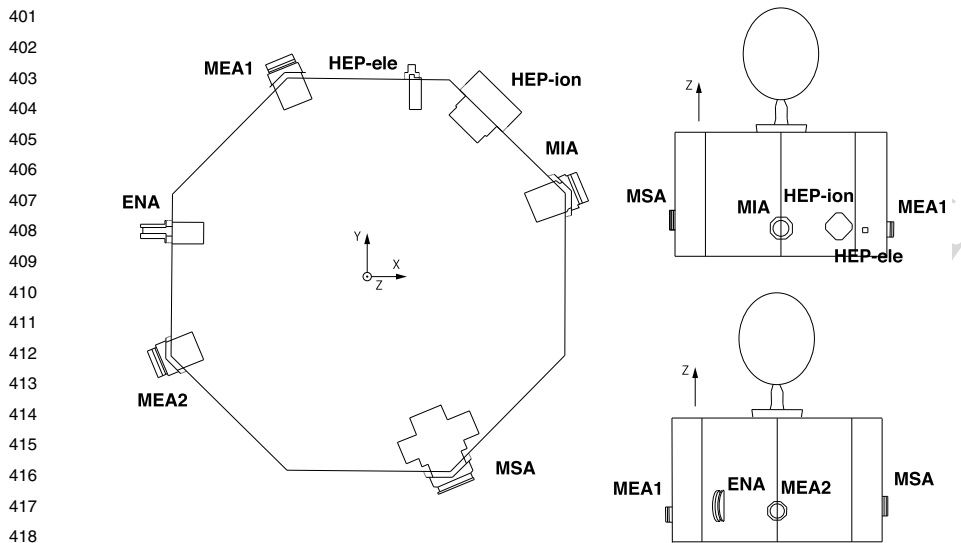


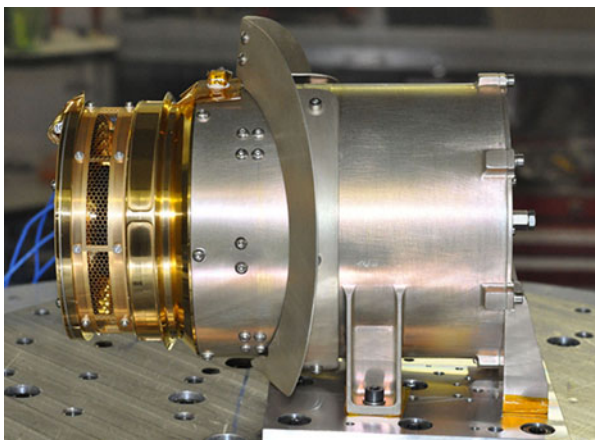
Fig. 2 Locations of the seven MPPE sensors

Space-Earth Environmental Research (ISEE)/Nagoya University and ISAS/JAXA in Japan. ENA measures the mass identified energetic neutral atoms between 10 eV and 3.3 keV and was developed by the Swedish Institute of Space Physics (IRF)-Kiruna in Sweden, University of Bern in Switzerland and ISAS/JAXA in Japan.

Figure 2 shows the locations of the MPPE sensors on Mio. The four low-energy sensors MEA1, MEA2, MIA, and MSA are referred to as low-energy particle (LEP) sensors. The LEP sensors have ring shaped FOVs in which the center axis is perpendicular to the spin axis of the spinning Mio spacecraft. The LEP sensors are installed on the four diagonal corners of the octagonal Mio spacecraft to minimize the interference of the spacecraft body in measuring low energy charged particles. MEA1 and MEA2, the two electron sensors, and MIA and MSA, the two ion sensors, are installed 90° apart to fulfill the requirements of the high time resolution measurements. The other MPPE sensors, including HEP-ion, HEP-ele and ENA are installed on the side panels of the Mio spacecraft. HEP-ion has a conical FOV, whereas HEP-ele and ENA have radial FOVs. To minimize the thermal input under the severe thermal conditions of Mercury's orbit, all the MPPE sensors are equipped with individual thermal shields in which the surface is coated with electrically conductive white paint.

A commonly used data processor Mission Data Processor 1 (MDP1) (Kasaba et al. 2020) controls all of the MPPE sensors and is responsible for processing the data sent from them. In addition, it formats the telemetry data, calculates the velocity moments (VMs), and reduces the quantity of data by adding, selecting, or compressing the data. Depending on the total telemetry rate of the Mio spacecraft, three different data rates of high, medium, and low are defined. The MPPE sensors are allocated to 72.5, 5.5, and 0.8 kbps as high, medium, and low data rates, reflected by H-mode, M-mode, and L-mode, respectively. The L-mode data are continuously available during the orbital period of about 9.4 h. The LEP sensors produce VMs of electrons and ions (density, velocity, temperature), and compressed E-t spectrograms with limited angle, mass, energy, and time resolution as L-mode data. The HEP sensors also produce count data with limited angle, mass, and energy resolution as L-mode data. ENA

451 **Fig. 3** View of the MEA2 sensor  
452 during vibration tests



453  
454  
455  
456  
457  
458  
459  
460  
461  
462  
463  
464  
465  
466  
467  
468  
469  
470  
471  
472  
473  
474  
475  
476  
477  
478  
479  
480  
481  
482  
483  
484  
485  
486  
487  
488  
489  
490  
491  
492  
493  
494  
495  
496  
497  
498  
499  
500

produces only L-mode data. The M-mode data are available during only about 25% of the entire observation period. The LEP and HEP sensors produce 3D counts with selected angle and time resolution or 2D counts as M-mode data. Although full 3D counts are produced as H-mode data, this mode is available only during limited periods.

## 3.2 MEA

### 3.2.1 Instrument Description of MEA

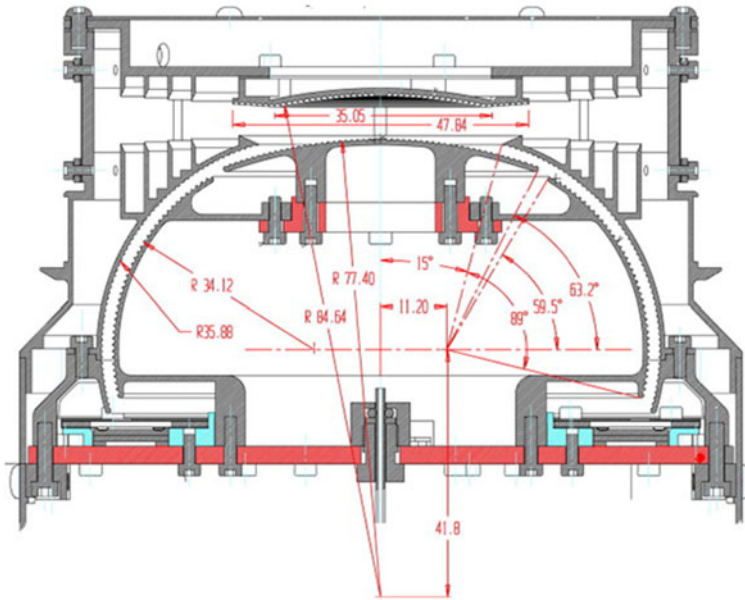
The MEA instrument is composed of two sensors MEA1 and MEA2, which combine the selection of incoming electrons according to their energies by electrostatic deflection in symmetrical toroidal analyzers. These instruments provide a uniform angle energy response with a fast imaging particle detection system (Sauvaud et al. 2010). MEA2 is illustrated in Fig. 3. One of the key and novel features of the MEA sensors is the implementation of an electronic device that enables the geometrical factor (G-factor) to vary by a factor of 1000 in the top-hat electrostatic analyzer to measure the solar wind and magnetospheric electron fluxes within more than six decades.

Figure 4 illustrates the identical electron optic design of MEA1 and MEA2 except for the entrance aperture, which is discussed subsequently. The electrostatic analyzer (ESA) consists of a  $95^\circ$  toroidal deflector with two concentric electrodes and a spherical top section. Whereas the outer electrode and the top-hat are at signal ground, the two parts of the inner electrode can be set at the same voltage ( $U_{an} = U_{top}$ ) as for a classical top-hat analyzer with an analyzer constant  $k = E/V = 9.6$ . When the central part of the inner electrode ( $U_{top}$ ) is biased with voltages lower than those applied to the toroidal part ( $U_{an}$ ), the energy and angular acceptance are both reduced leading reduction of the G-factor.

Figure 5 shows the microchannel plate (MCP) in a chevron stack configuration, which are used to multiply the incident electrons. Figure 6 shows the 16 discrete anodes of  $22.5^\circ$  each of which is used for position encoding that are connected to amplifiers/discriminators followed by Amptek A111F counters with a detection threshold of  $10^5$  electrons.

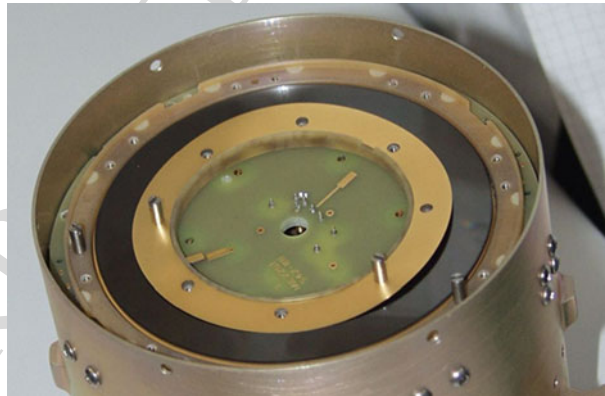
Figure 7 shows the entrance of the electrostatic analyzer of MEA, which includes four baffles for reducing the penetration of ultraviolet light (UV) in the hemispherical spheres.

501  
502  
503  
504  
505  
506  
507  
508  
509  
510  
511  
512  
513  
514  
515  
516  
517  
518  
519  
520  
521  
522  
523  
524  
525  
526  
527  
528  
529  
530  
531  
532  
533  
534  
535  
536  
537  
538  
539  
540  
541  
542  
543  
544  
545  
546  
547  
548  
549  
550



**Fig. 4** Electron optic design of MEA

**Fig. 5** View of the MCPs located inside the MEA2 sensor head

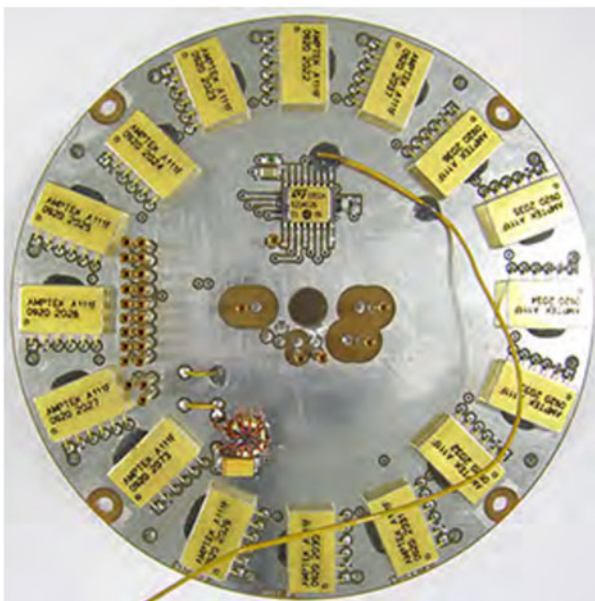


The generation of photoelectrons inside the instrument is further limited by the use of golden, polished parts that also serve to decrease the heat flux into the instrument.

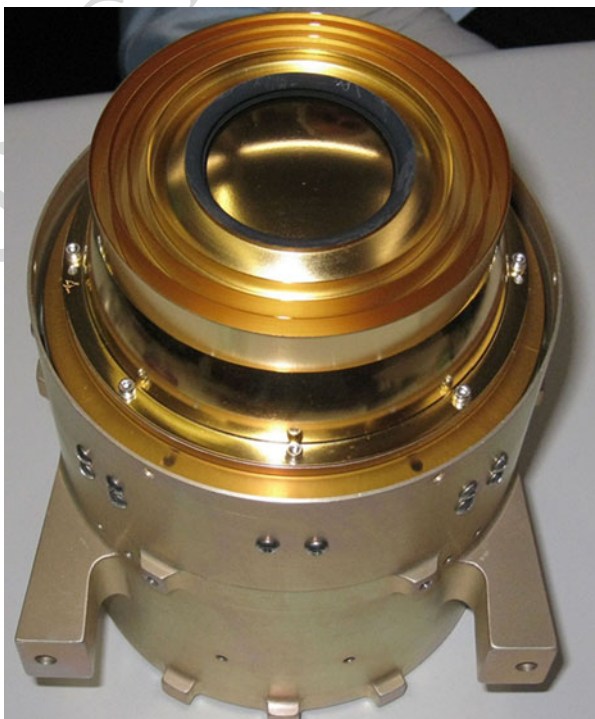
Figure 8 illustrates the use of scalloping on the outer and inner plates of the toroidal deflector and the top-hat, for reducing the transmission of secondary electrons and UV photons. The analyzer plates are further coated with  $\text{Cu}_2\text{S}$  black to efficiently absorb stray light, as obtained from Collini (<https://www.collini.eu>).

Figure 9 shows the high voltage board which provides two sweeping voltages of 0–3000 V for the analyzer, and a static power supply from 0–3400 V for the MCPs. To select the energy of incident electrons, we vary the deflection voltages of the inner plates of the electrostatic analyzer logarithmically with 128 equally spaced steps in synchronization with the spacecraft spin period. MEA measures the full  $4\pi$  electron distributions with

551 **Fig. 6** Anode board of MEA2



570  
571  
572  
573  
574  
575  
576 **Fig. 7** View of the entrance of  
577 the electrostatic analyzer of MEA



601  
602  
603  
604  
605  
606  
607  
608  
609  
610  
611  
612  
613  
614  
615  
616  
617  
618  
619  
620  
621  
622  
623  
624  
625  
626  
627  
628  
629  
630  
631  
632  
633  
634  
635  
636  
637  
638  
639  
640  
641  
642  
643  
644  
645  
646  
647  
648  
649  
650

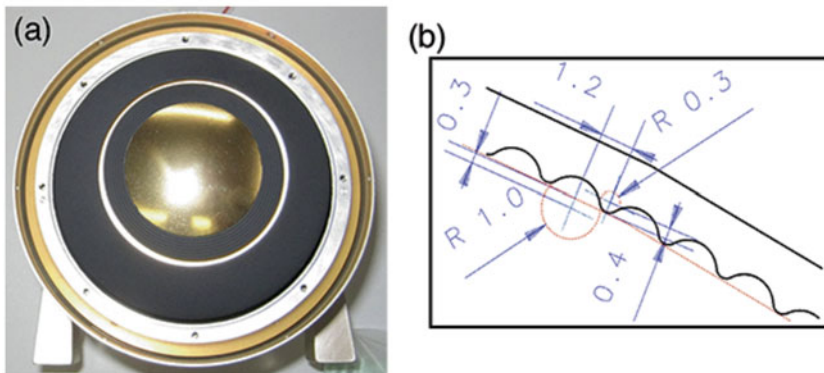
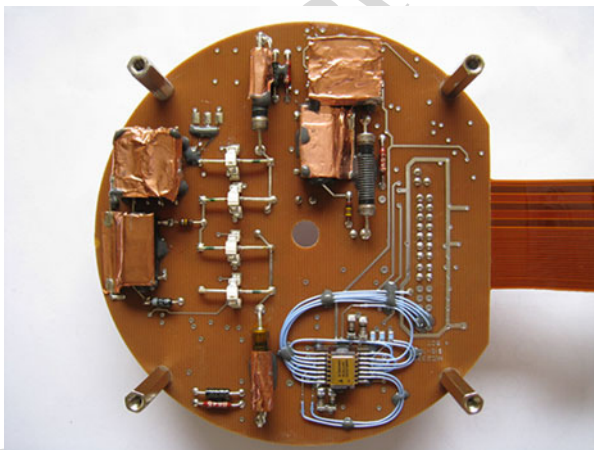


**Fig. 8** (a) View of the toroidal inner sphere of MEA2. (b) Dimensions of the scalloping used

**Fig. 9** High-voltage board of MEA2



a single analyzer in 1/2 of the spacecraft spin period or with the two analyzers in 1/4 of the period.

Figure 10 shows the field-programmable gate array (FPGA) board with two Actel RT54SX72SU components used to control all functionalities of the instrument. The first controls the sensor head and accumulates the counting rates, and the second transmits/receives data/commands from the data processing unit (MDP1) shared by all MPPE instruments using the spacewire protocol.

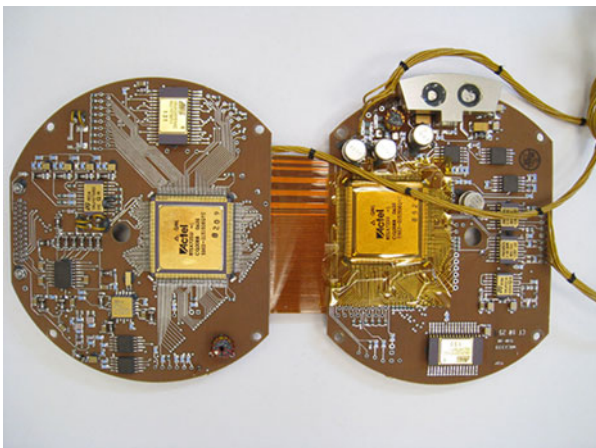
A multi-layer insulator (Fig. 11) and a thermal shield (Fig. 12) coated with white paint are used to ensure the thermal protection of the sensors. The peak temperatures near Mercury reach 140 °C on the thermal shield, 85 °C on the spheres, and 60 °C on the MCPs and electronic boards when operating.

Table 1 summarizes the key parameters of the MEA sensors, and Fig. 13 shows a block diagram of the instrument.

### 3.2.2 Operation Mode and Data Products of MEA

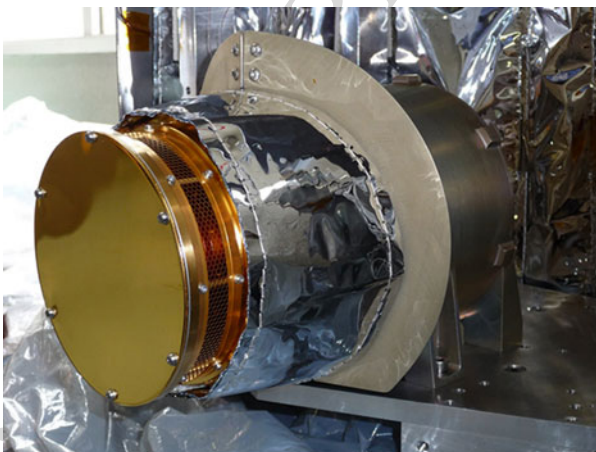
MEA includes versatile and easily programmable operating modes and data processing routines for optimizing the data collection for specific scientific studies and widely varying

651 **Fig. 10** FPGA board of MEA2



652  
653  
654  
655  
656  
657  
658  
659  
660  
661  
662  
663  
664  
665  
666  
667  
668  
669  
670  
671  
672  
673  
674  
675  
676  
677  
678  
679  
680  
681  
682  
683  
684  
685  
686  
687  
688  
689  
690  
691  
692  
693  
694  
695  
696  
697  
698  
699  
700

**Fig. 11** MEA2 with its multi-layer insulator integrated with the Mio spacecraft



plasma regimes. Depending on the telemetry mode, MEA can transmit several MDP1 data products, including those listed below.

1. Electron omnidirectional fluxes (Et-OMN).
2. Electron VM. The instrument transmits the temperature, heat flux vector, and number density calculated in several energy bands. The position of the boundaries of each energy band is defined by commands.
3. Electron pitch angle distribution for four selected energies (Et-PAP). MEA uses the magnetic field vector as the external input for this mode and transmits the 2D angle-energy distribution.
4. Full 3D electron distribution. The instrument transmits a complete angular-energy spectrum accumulated for a minimum of 1/4 of the spacecraft spin.

MEA uses different energy tables to adapt to the various space environment conditions encountered by the Mio spacecraft. The choice of energy table used is defined by commands. The four energy tables available for MEA include

1. 3–300 eV

Fig. 12 Thermal shield of MEA2

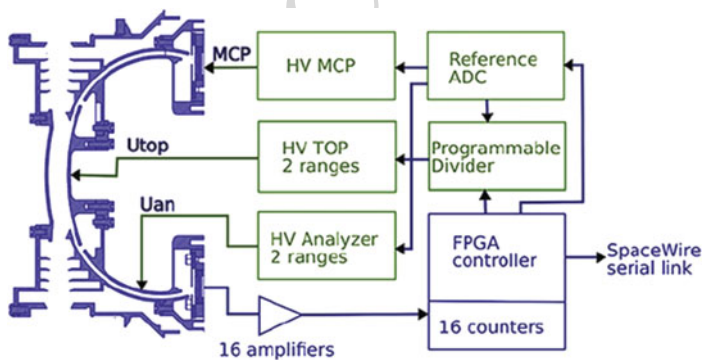


Fig. 13 Block diagram of MEA

2. 3–25000 eV
3. 3–3000 eV
4. 3000–25000 eV

In addition, MEA has unique data modes that can be defined by commands, depending on the number of channels (16 or 32) and energies (16, 32 or 64).

Table 2 shows the various MPPE data mode names and the corresponding data products of MEA1 and MEA2 together with the time resolution depending on the telemetry mode of

751 **Table 1** Summary of MEA performance

752	Field of view	$8^\circ \times 360^\circ$
753		
754	Angular resolution	$22.5^\circ \times 11.25^\circ$
755		
756	Energy range	3 eV–25,500 eV (Mercury mode)
757		3 eV–3000 eV (solar wind mode)
758	Energy resolution	$\Delta E/E \sim 10\%$ (at full G-factor)
759		
760	Stepping energies and cadence	Full energy sweep with 64 contiguous energy channels every 16 or 32 times per 4 s spin
761		
762	Time resolution to obtain the full 3D velocity distribution function	Half a spin period, 2 s (using a single analyzer)
763		Quarter of a spin period, 1 s (using the two analyzers)
764	Geometrical factor	
765	MEA1 max./min.	$4.0 \times 10^{-3} / 6.7 \times 10^{-5} \text{ cm}^2 \text{ sr eV/eV}$
766	MEA2 max./min.	$2.0 \times 10^{-4} / 4.0 \times 10^{-6} \text{ cm}^2 \text{ sr eV/eV}$
767		
768	Mass	2.598 kg for MEA1 + MEA2
769		+0.460 kg for their thermal shields
770	Power	2.260 W (average for MEA1 + MEA2)
771		3.460 W (peak for MEA1 + MEA2)
772		1.880 W (stand-by for MEA1 + MEA2)
773		
774	Dimensions	177 mm $\times$ 120 mm $\phi$ (MEA1, MEA2)
775		
776	Data rate	0.1 kbits/s (L-mode)
777		2.5 kbits/s (M-mode)
778		11 kbits/s (H-mode)
779		after factor 3 compression
780		for MEA1 + MEA2

781  
782  
783 the Mio spacecraft. Tables 3, 4, and 5 detail the properties of MEA data products for each  
784 Mio telemetry mode.

785 All MEA data products will be available in Common Data Format (CDF, <https://cdf.gsfc.nasa.gov>) files.

### 788 3.2.3 Pre-flight Calibration of MEA

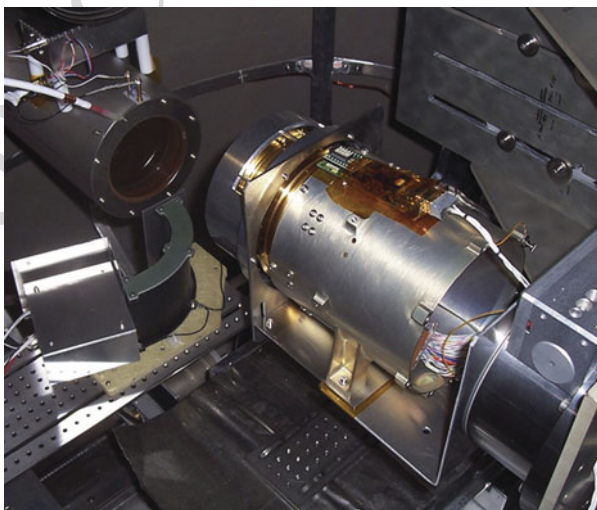
789  
790 The calibration of the two MEA sensors and a flight spare model was conducted at the IRAP  
791 Toulouse vacuum facilities. The parameters shown in Table 6 will be used to describe the  
792 various calibration setups, procedures, and results.

793 The pre-flight calibration of the MEA sensors consisted of full calibration of the sensors,  
794 the characterization of the MCP detectors of the sensors, and sensor testing for UV con-  
795 tamination. To derive the calibration parameters for a configuration as close as possible to  
796 that of the sensors in space, full calibration was performed with a realistic simulator of the  
797 instrument thermal shield and with the magnetic field of Earth inside the vacuum chamber  
798 compensated by Helmholtz coils. Figure 14 shows the MEA1 sensor installed in the setup  
799 and its simulator for the thermal shield, the beam monitor, and the magnetometer, which  
800

**Table 2** MEA data products with time resolution as a function of MPPE mode and Mio telemetry mode

MPPE mode name	L-mode data products	M-mode data products	H-mode data products
	<b>MEA1</b>	<b>MEA1</b>	
1. Default Observation Mode	Et-OMN (4s)	Et-OMNm (4s)	N.A.
	Et-PAP (16s)	Et-PAP (4s)	
	VM (16s)	VM (4s)	
	3D-LL (640s)	3D-M (8s) or 3D-M (4s)	
	<b>MEA2</b>	<b>MEA2</b>	
	Et-OMN (4s)	Et-OMNm (2s)	
	Et-PAP (16s)	Et-PAP (2s)	
	VM (16s)	VM (2s)	
	<b>MEA1</b>	<b>MEA1</b>	<b>MEA1</b>
2. Exospheric Mode	Et-OMN (4s)	Et-OMNm (4s)	3D-H (4s)
3. Solar Wind Mode	Et-PAP (16s)	Et-PAP (16s)	
/IP Shock Local Mode	VM (16s)	VM (4s)	
4. IP Shock Macro Mode	3D-LL (640s)	3D-M (8s)	
/Bow Shock Mode		or 3D-M (4s)	
5. Reconnection Mode			
6. Magnetospheric Mode	<b>MEA2</b>	<b>MEA2</b>	<b>MEA2</b>
	Et-OMN (4s)	Et-OMNm (2s)	3D-H (2s)
	Et-PAP (4s)	Et-PAP (2s)	
	VM (16s)	VM (2s)	

**Fig. 14** MEA1 installed in the vacuum chamber. A magnetometer is glued to the sensor housing. The instrument is turned by 90° in elevation. The simulator for the thermal shield of the sensor is shown above the aperture of the sensor



continuously measures the residual magnetic field in the vicinity of the sensor. The measurements of the magnetometer are automatically used to adjust the residual magnetic field below a maximum value of 0.5  $\mu\text{T}$ . For each calibration step, absolute measurements of the properties of the employed electron beam were taken.

**Table 3** MEA1 and MEA2 data products for the low-resolution telemetry mode (L-mode)

L-mode			
MEA1			
Data product name	Description	Time resolution (s)	Note
Et-OMN	E-t count data	4	
	16 energy		
Et-PAP	E-t pitch angle data	16	
	4 energy × 16 pitch angle		
VM	velocity moment	16	6 energy ranges
	n (density)		
	nVx, nVy, nVz (velocity)		
	Pxx, Pyy, Pzz		
	Pxy, Pyz, Pzx (pressure)		
3D-LL	qx, qy, qz (heat flux)	640	0: all energy steps above satellite potential * 2; 1–5: 5 energy steps below satellite potential * 2
	3D count data		
	88 direction × 16 energy		
MEA2			
Data product name	Description	Time resolution (s)	Note
Et-OMN	E-t count data	4	
	16 energy		
Et-PAP	E-t pitch angle data	16	
	4 energy x 16 pitch angle		
VM	velocity moment	16	6 energy ranges
	n (density)		
	nVx, nVy, nVz (velocity)		
	Pxx, Pyy, Pzz		
	Pxy, Pyz, Pzx (pressure)		
	qx, qy, qz (heat flux)		0: all energy steps above satellite potential * 2; 1–5: 5 energy steps below satellite potential * 2

The counts for each MCP anode as a function of MCP HV are shown in Fig. 15. The working point of both MCP detectors for MEA1 and MEA2 was set to 2750 V as delineated by the red vertical line in the figure. The working point is defined here by the bias voltage applied to the MCP needed for reaching a plateau in the MCP counts.

The UV contamination test results are shown in Fig. 16. The strong count at the small energies show the photoelectrons emitted inside the instrument and the vacuum chamber. The maximal background was less than 1 per second per anode.

Full calibration of the MEA1 and MEA2 sensors was conducted in the coordinate frame shown in Fig. 17. The electron beam properties are given below.

- For each azimuth angle  $\Phi$ , a scan was made over elevation angle  $\Theta$ .
- For each angular position, the set of G-factors was tested.
- For each value of G-factor, the analyzer voltage was scanned.

Figures 18 and 19 show the energy, elevation and azimuthal responses for different anodes and G-factor levels. The dashed curves in these plots show the polynomial fit that

**Table 4** MEA1 and MEA2 data products for the medium-resolution telemetry mode (M-mode)

M-mode

MEA1

Data product name	Description	Time resolution (s)	Note
Et-OMNm	E-t count data 32 energy	4	
Et-PAP	E-t pitch angle data 4 energy × 16 pitch angle	4	4 starting energy steps and width are selectable by commanding
VM	velocity moment n (density) nVx, nVy, nVz (velocity) Pxx, Pyy, Pzz Pxy, Pyz, Pzx (pressure) qx, qy, qz (heat flux)	4	6 energy ranges 0: all energy steps above satellite potential * 2; 1–5: 5 energy steps below satellite potential * 2
3D-M (8s)	3D count data 88 direction × 16 energy	8	(MPPE mode = 0 1 2 3 5)
3D-M (4s)	3D count data 88 direction × 16 energy	4	(MPPE mode = 4 6 7 8)

MEA2

Data product name	Description	Time resolution (s)	Note
Et-OMNm	E-t count data 32 energy	2	
Et-PAP	E-t pitch angle data 4 energy × 16 pitch angle	2	
VM	velocity moment n (density) nVx, nVy, nVz (velocity) Pxx, Pyy, Pzz Pxy, Pyz, Pzx (pressure) qx, qy, qz (heat flux)	2	6 energy ranges 0: all energy steps above satellite potential * 2; 1–5: 5 energy steps below satellite potential * 2

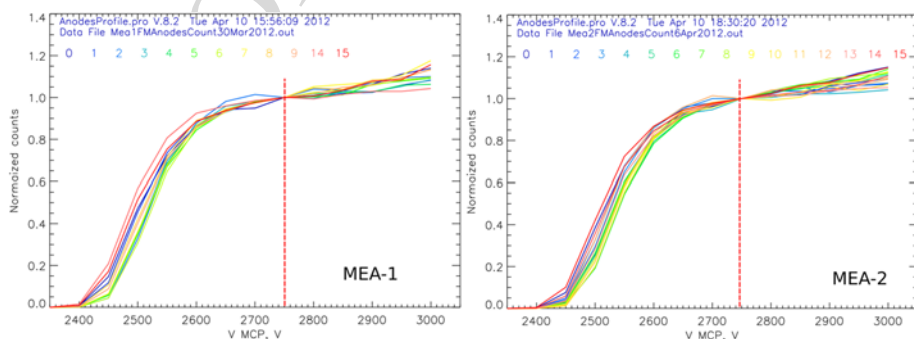


**Fig. 15** MCP counts as a function of MCP bias voltage. Each of the 16 anodes is represented by a different color, with the anode number printed in the same color at the top of the plot

**Table 5** MEA1 and MEA2 data products for the high-resolution telemetry mode (H-mode)

H-mode

MEA1

Data product name	Description	Time resolution (s)	Note
3D-H	3D count data 88 direction × 32 energy	4	16 sectors, 8 channels

MEA2

Data product name	Description	Time resolution (s)	Note
3D-H	3D count data 88 direction × 32 energy × 2	2	16 sectors, 8 channels + 16 sectors, 8 channels

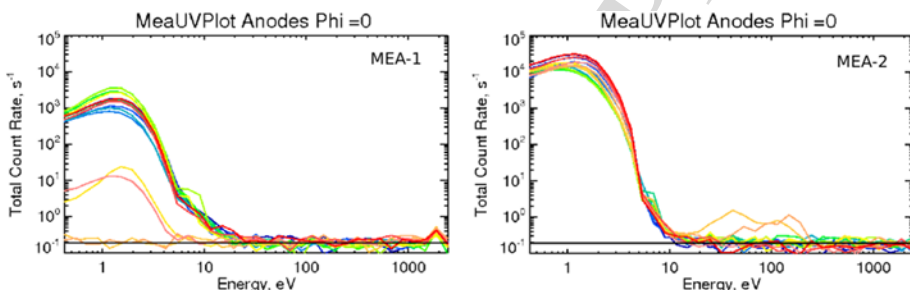


**Fig. 16** UV contamination test results for MEA1 and MEA2. Each of the 16 anodes is represented by a different color as described in Fig. 15

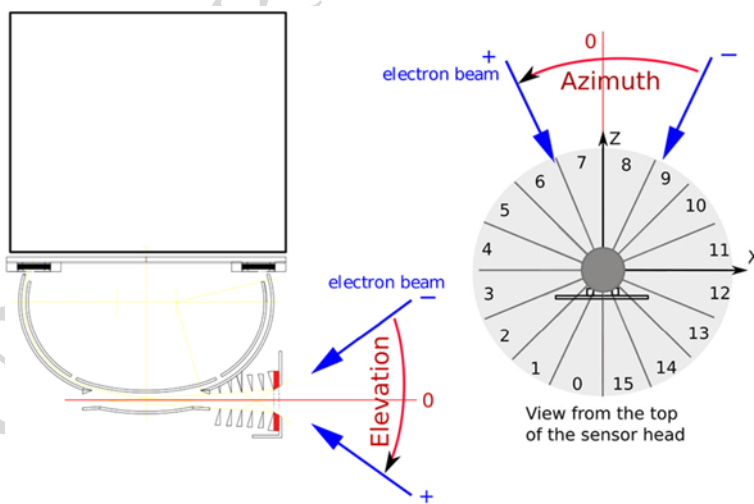


**Fig. 17** Definition of the elevation and azimuth angles for full calibration of the MEA sensors

**Table 6** Parameters used to describe the various calibration setups, procedures, and results

1001		
1002	E	Incident electron energy, eV
1003	$\Theta$	Elevation angle
1004	$\Phi$	Azimuth angle
1005	Uan	Analyzer voltage
1006	Utop	Top part of analyzer voltage
1007	K	$E = U_{an} \cdot K$
1008	K0	Best K for the current $\Theta$ and $\Phi$
1009	$\Delta E/E$	Energy resolution of the analyzer
1010	$P_{BEAM}$	Electron beam flux $\text{cm}^{-2} \text{s}^{-1}$ as a function of the elevation angle
1011	$\Omega_i$	One azimuthal sector aperture, $\text{cm}^2$ for fixed $\Theta$ , $\Phi$ , Uan and Utop
1012	Ci	Count rate, $\text{s}^{-1}$ of one azimuthal sector
1013	Gi	One sector G-factor, $\text{cm}^2 \text{sr eV/eV}$
1014	G	Total G-factor of the instrument, $\text{cm}^2 \text{sr eV/eV}$ (used for numerical simulation)
1015	HV <sub>MCP</sub>	MCP high voltage, V, measured at the HV unit level
1016		

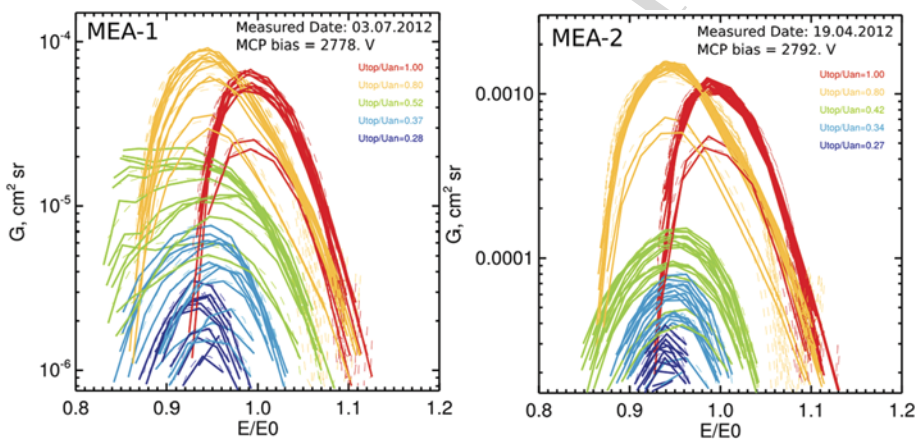


**Fig. 18** Energy responses of different anodes for various G-factor levels. Each of the 16 anodes is represented for each G-factor level

enabled definition of  $\Delta E/E$  and  $\Delta\Omega$  with high accuracy. When the central part of the inner electrode (Utop) is biased with voltages lower than those applied to the toroidal part (Uan), the analyzer accepts particles coming from a slightly higher azimuth. The energy and angular acceptance are both reduced leading to a reduction of the G-factor. The G-factor for each anode versus the value of Utop/Uan is shown in Fig. 20, where the theoretical profile obtained from the numerical simulation is represented by a dashed curve. MEA2 has a maximum GF0/GF ratio of 1000, whereas that of MEA1 is only 60 because it includes a grid attenuator with 5% transparency at its entrance. Table 7 summarizes the calibration results for MEA1 and MEA2.

### 3.2.4 Near-Earth Commissioning Results of MEA

On July 1 and 2, 2019, the two MEA sensors were turned on, respectively, when the Bepi-Colombo spacecraft was about 29 million km from Earth. MEA1 and MEA2 have per-

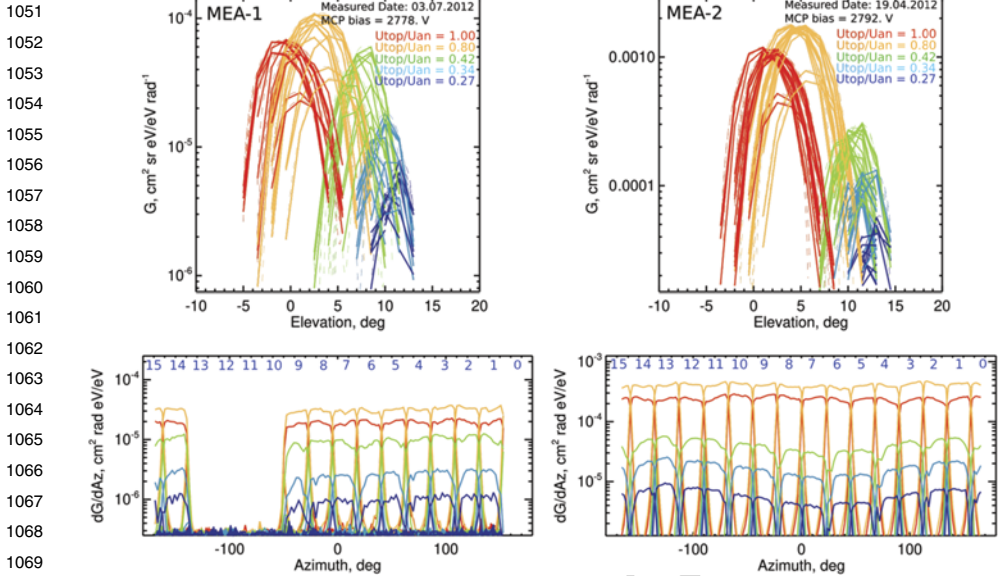


**Fig. 19** Top: Elevation response of the 16 anodes for various G-factor levels (in color). Each of the 16 anodes is represented for each G-factor level. Bottom: azimuthal response of the 16 anodes for various G-factor levels (in color, same color code as used on the top panel)

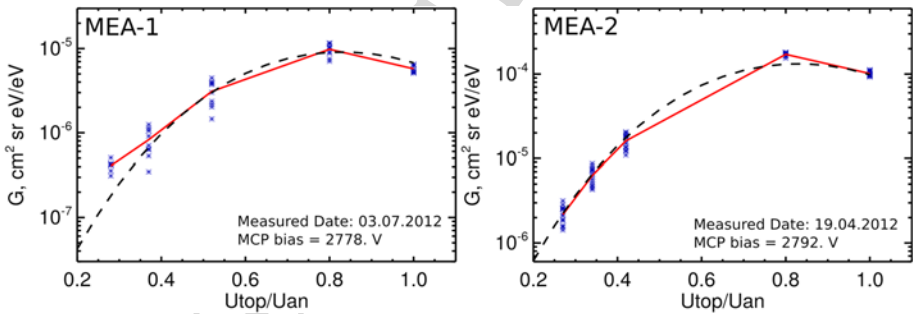
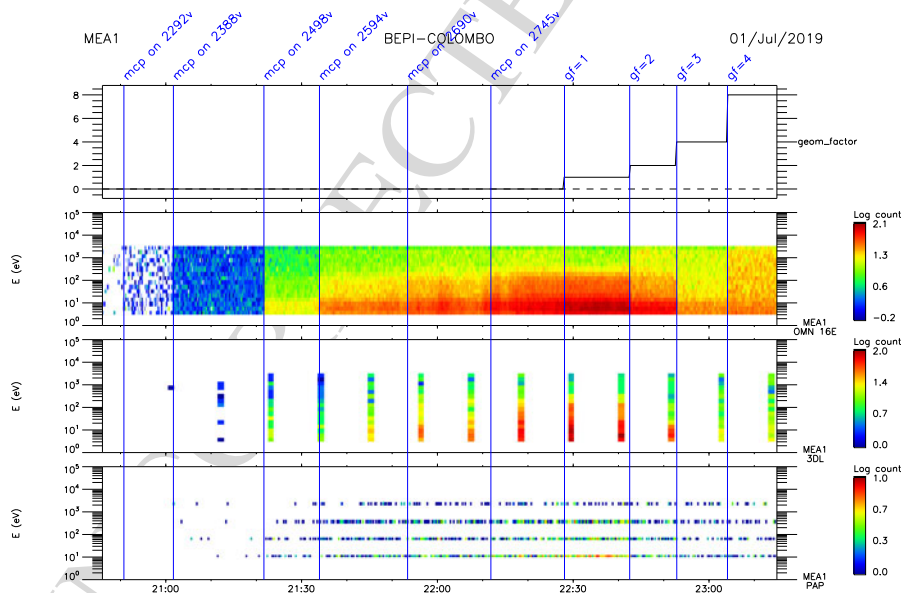


**Fig. 20** Anodes G-factors as a functions of  $U_{top}/U_{an}$ . The dashed lines show the theoretical profile scaled with the appropriate factor

fectly responded to our commands up to their nominal working point of 2750 V applied to their MCPs. Hence, the very first electron spectra in the solar wind have been successfully obtained, even though Mio is behind the MOSIF thermal shield. Figures 21 and 22 show the MEA1 and MEA2 data, respectively. The solar wind electron moments were estimated from MEA1 3D data after noise removal (Fig. 23). The density calculated from the MEA1 data when integrated over all energies, including both core and halo (above 100 eV) solar wind electrons ( $1.9 \text{ cm}^{-3}$ ), and the first eleven energies for the core solar wind electrons ( $0.9 \text{ cm}^{-3}$ ), and the temperature (13 eV), agree well with expected values at the location

**Table 7** Summary of MEA1 (top) and MEA2 (bottom) calibration. GF corresponds to the geometrical factor of the instrument ( $\text{cm}^2 \text{sr eV/eV}$ ), and GF0 corresponds to the GF when  $U_{\text{top}} = U_{\text{an}}$ .  $\Delta\theta$  is the elevation FWHM. The remaining parameters are defined in Table 6

MEA1				
Utop/Uan	0.8	0.42	0.34	0.27
GF $\text{cm}^2 \text{sr eV/eV}$	4e-3	6.7e-3	2.0e-3	6.7e-5
GF0/GF	1	6	20	60
$\Theta$ deg	1.8	7.0	8.2	9.0
$\Delta\Theta$ deg	5.9	4.5	3.0	3.6
K	8.67	8.48	8.57	8.51
$\Delta E/E$	0.11	0.16	0.11	0.09
MEA2				
Utop/Uan	0.8	0.52	0.37	0.28
GF $\text{cm}^2 \text{sr eV/eV}$	2e-4	6.7e-5	1.6e-5	4.0e-6
GF0/GF	20	60	250	1000
$\Theta$ deg	1.8	6.3	7.5	9.0
$\Delta\Theta$ deg	5.9	5.0	3.0	3.5
K	8.67	8.62	8.57	8.51
$\Delta E/E$	0.11	0.13	0.11	0.08



Produced by CLWeb

**Fig. 21** First MEA1 data obtained in the solar wind on July 1, 2019. The first panel is the GF of the sensor that was varied by decreasing the ratio  $U_{\text{top}}/U_{\text{an}}$  from 1 to its lowest value at the end of the interval (for corresponding values of the GF see Fig. 20 from right to left). The vertical lines delineate the commands sent to MEA1 during the time period, particularly when the HV was raised to nominal values of 2750 V. The three following panels indicate the energy-time spectrogram of Et-OMN data (in counts), 3D data, and pitch-angle distributions for four selected energies, in L-mode

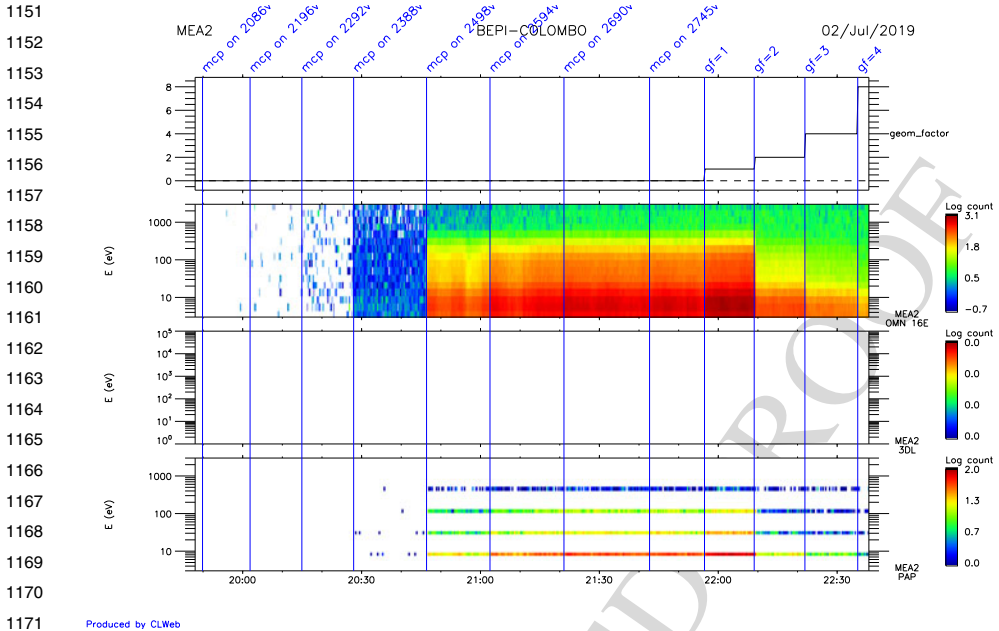
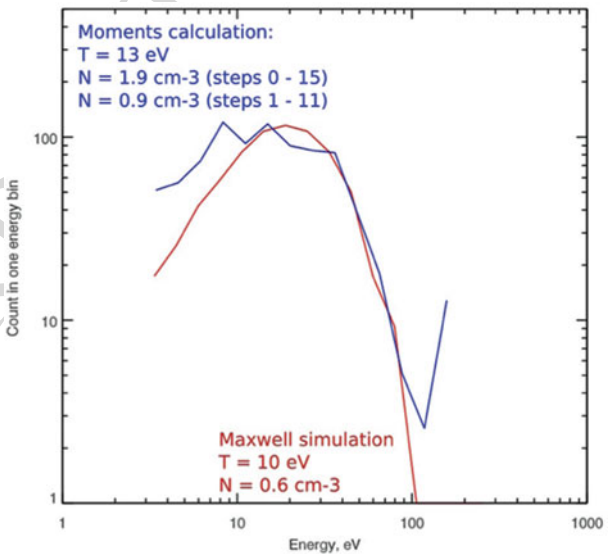


Fig. 22 First MEA2 data obtained in the solar wind on July 2, 2019. The description is presented in Fig. 21

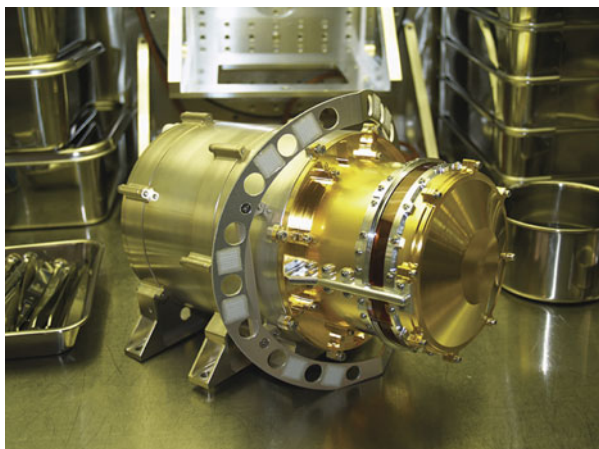
Fig. 23 MEA1 moment (density, temperature) estimated from 3D data (blue) and compared with a Maxwellian distribution function (red), after noise removal. The spike observed above 100 eV corresponds to part of the halo solar wind electron distribution function



of the Mio spacecraft as well as those with a Maxwellian distribution with a density of  $0.6 \text{ cm}^{-3}$  and temperature of 10 eV.

The very first data obtained during the near-Earth orbit phase commissioning of the MEA instrument confirm that both MEA1 and ME2 are working normally. In the near future the MEA instrument will be turned on again during Earth, Venus, and Mercury fly-bys

1201 **Fig. 24** MIA flight model  
1202 delivered to the Mio system in  
1203 June 2014  
1204  
1205  
1206  
1207  
1208  
1209  
1210  
1211  
1212  
1213  
1214  
1215  
1216



1217 and during the cruise phase to enable multipoint measurements of electrons in the solar  
1218 wind together with electron spectrometers onboard the Solar Orbiter and Parker Solar Probe  
1219 missions.  
1220

### 1221 **3.3 MIA**

#### 1222 **3.3.1 Instrument Description of MIA**

1223 MIA as shown in Fig. 24 was developed to understand the structure and plasma dynamics of  
1224 Mercury’s magnetosphere; Mercury–solar wind interaction; atmospheric abundances, struc-  
1225 tures, and generation/loss processes; and the solar wind between 0.3 and 0.47 AU (Miyake  
1226 et al. 2009). To achieve these research objectives, MIA should be able to measure both  
1227 the 3D distribution function of solar wind ions around Mercury (0.3–0.47 AU) and the  
1228 planet’s magnetospheric ions. Figure 25 shows a block diagram of MIA, which consists  
1229 of the (A) spacecraft interface board, (B) positive high voltage board, (C) negative high  
1230 voltage board, and (D) analyzer. As shown in Fig. 25(D), MIA is a top-hat type electro-  
1231 static analyzer with toroidal deflectors (Saito et al. 2010a). Figure 26 shows the “top-cap”  
1232 and upper part of the entrance collimator (panel (a)) and inner sphere and lower part of the  
1233 entrance collimator (panel (b)). The surface of the analyzer is gold plated or blackened by  
1234 copper sulfide black. The blackening process “Ultraviolet Absorbing Black plating” was de-  
1235 veloped by Mitsuya Co. Ltd. in Japan (<https://www.mitsuya-plating.com>). In addition, the  
1236 inner and outer spheres are serrated with the tip-to-root length and tip angle of the sawtooth  
1237 serrations at 0.5 mm and 60°, and the light traps are placed at the top part of the outer sphere  
1238 to minimize the solar UV entering the detector (MCP). MIA measures 3D ion distribution  
1239 function utilizing the spin motion of the spacecraft. The diameters of the inner and outer  
1240 toroidal electrodes are 32 mm and 35 mm, respectively, with the center shifted 5 mm toward  
1241 the radial direction. The resultant analyzer constant is 5.66.  
1242  
1243

1244 Stepping high voltage between 0 V and  $-5$  kV is applied to the inner toroidal electrode.  
1245 Figure 27 shows the spacecraft interface board. On the rear side (panel (a)), two MDM  
1246 connectors are shown including a 9-pin checkout connector and a 25-pin SpaceWire/power  
1247 supply interface connector. On the front side (panel (b)), two Hypertac connectors are placed  
1248 including one connected to the high voltage boards and the other connected to the applica-  
1249 tion specific integrated circuit (ASIC) on the MCP anode. Figure 28 shows the negative  
1250

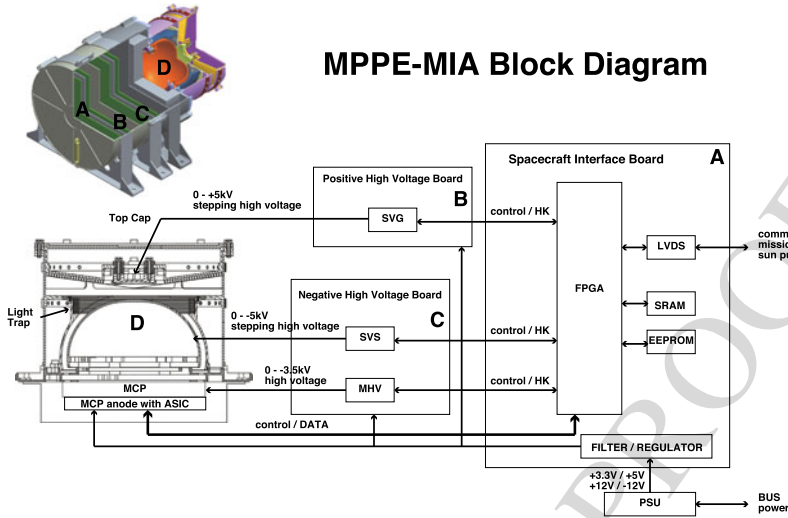


Fig. 25 MIA block diagram

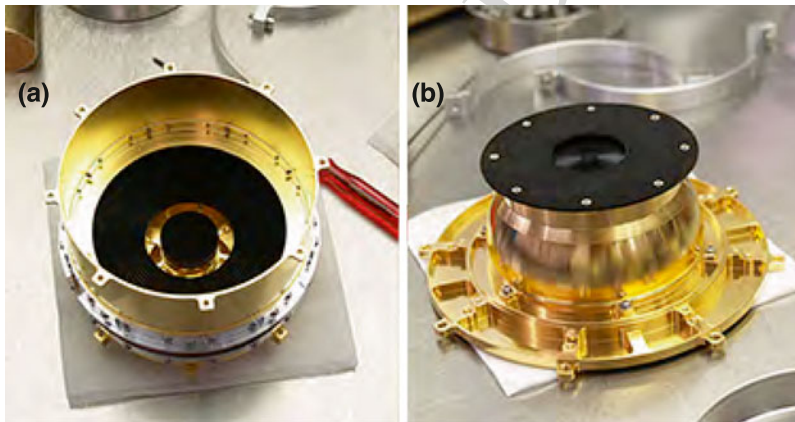
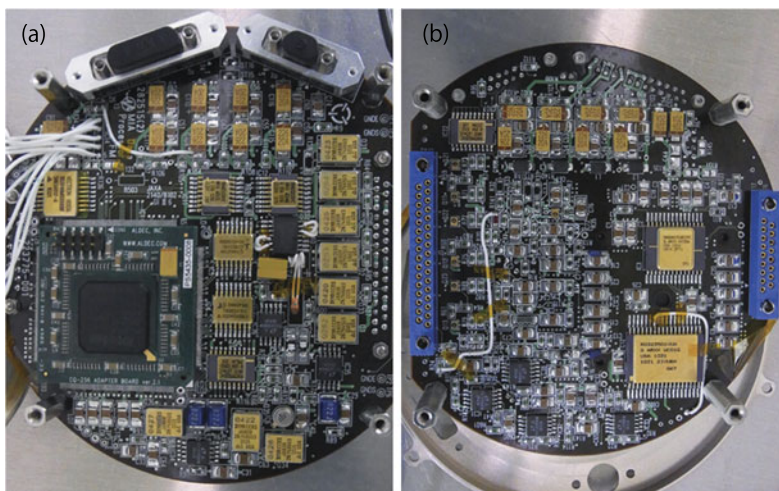


Fig. 26 (a) “Top-cap” and upper part of the entrance collimator of MIA. (b) Inner sphere and bottom part of the entrance collimator of MIA. The parts are gold plated or blackened by copper sulfide black

high voltage board installed in the chassis of MIA (Fig. 25(C)). Among the three electronics boards (Fig. 25(A)–(C)) shielding plates are installed to reduce the electrical noise and the risk of electrical discharge among the electronics boards. Ions enter the analyzer by passing through the collimator and are attracted down toward the inner electrode by receiving Coulomb force from the electric field between the “top-cap” and the inner electrode. Ions with specific energy ranges determined by the high voltage applied to the inner electrode can pass through the toroidal analyzer, enter the Z-stack MCP and become multiplied to generate detectable amounts of charge clouds. A grid having the same voltage as the input surface of the MCP is placed between the MCP and the toroidal analyzer.

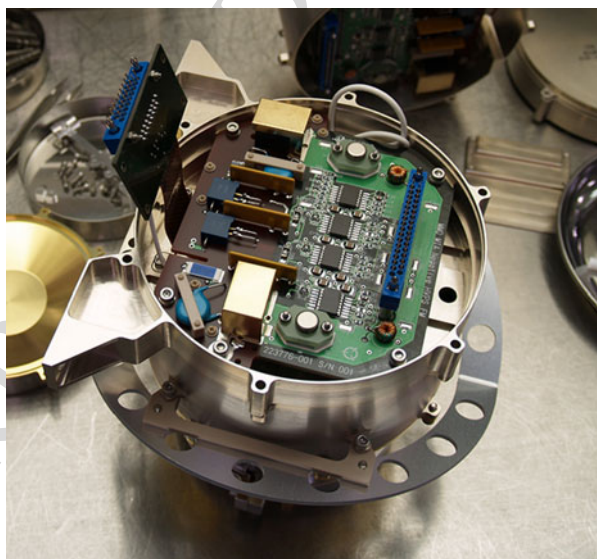
The charge clouds from the MCP are detected by a 63-channel discrete anode (Saito et al. 2017). The incident azimuthal directions of the ions correspond to the positions at which

1301  
1302  
1303  
1304  
1305  
1306  
1307  
1308  
1309  
1310  
1311  
1312  
1313  
1314  
1315  
1316  
1317  
1318  
1319  
1320  
1321  
1322  
1323  
1324  
1325  
1326  
1327  
1328  
1329  
1330  
1331  
1332  
1333  
1334  
1335  
1336  
1337  
1338  
1339  
1340  
1341  
1342  
1343  
1344  
1345  
1346  
1347  
1348  
1349  
1350



**Fig. 27** Digital interface board of MIA. (a) Rear side, (b) front side

**Fig. 28** Negative high voltage board installed in the chassis of MIA. A Hypertac connector from ASIC on the MCP anode is also shown



the charge clouds are detected. The detected charge clouds are fed into a newly developed ASIC of which the bare chip is installed at the back side of the discrete MCP anode. The ASIC consists of 64-channel discriminators, 64-channel fast preamplifiers, and 64-channel counters (Saito et al. 2017).

MIA should measure both intense solar wind ions and tenuous Mercury magnetospheric ions. Therefore, the required dynamic range for detecting low-energy ion flux is as wide as  $10^6$  (Mukai et al. 2004). To measure both solar wind ions without saturation and Mercury magnetospheric ions with sufficient counting statistics, MIA includes an attenuation grid with 10% transmission placed at limited channels (one of the two  $\pm 60^\circ$  angular ranges

1351  
1352  
1353  
1354  
1355  
1356  
1357  
1358  
1359  
1360  
1361  
1362  
1363  
1364  
1365  
1366  
1367  
1368  
1369  
1370  
1371  
1372  
1373  
1374  
1375  
1376  
1377  
1378  
1379  
1380  
1381  
1382  
1383  
1384  
1385  
1386  
1387  
1388  
1389  
1390  
1391  
1392  
1393  
1394  
1395  
1396  
1397  
1398  
1399  
1400

**Fig. 29** Attenuation grid of MIA. (a) The relationship between the spin axis and the entrance of MIA with the mechanical attenuation grid. (b) Ion entrance of MIA with the mechanical attenuation grid. (c) Pattern of attenuation grid

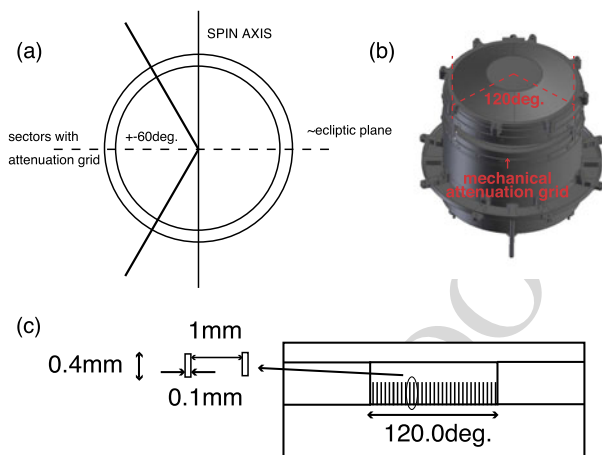
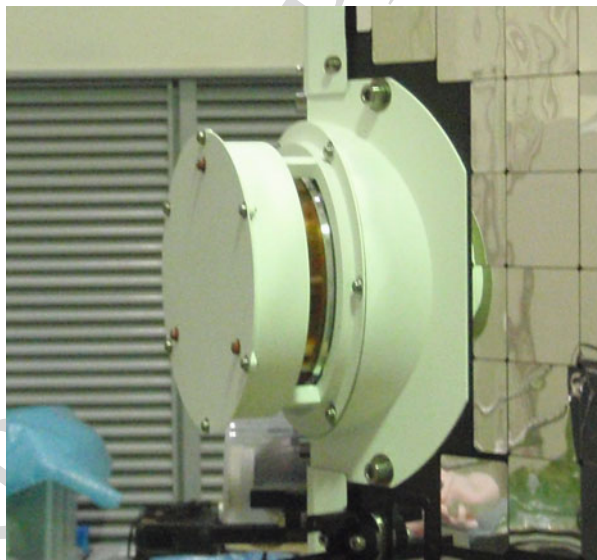


**Fig. 30** MIA with thermal shield installed on one of the eight corners of the Mio spacecraft. The entrance aperture is covered by a Kapton sheet that was removed before the launch



centered at the spin plane) of the entrance part of the analyzer. Figure 29 shows a schematic diagram of the attenuation grid pattern.

In addition, MIA includes a function for reducing the geometrical factor electrically for solar wind ion measurement. The sensitivity of the analyzer can be reduced by applying positive high voltage to the “top-cap” insulated from the surrounding structures. By applying stepping high voltage between 0 V and +5 kV and synchronizing with the inner sphere voltage, the G-factor can be reduced to  $\sim 1/50$  (Miyake et al. 2009).

To reduce the strong thermal input to MIA on Mercury orbit, MIA is equipped with its own thermal shield (Fig. 30). The thermal shield is composed of titanium and the surface is painted with electrically conductive white paint.

According to our knowledge of Earth’s magnetosphere, full 3D measurements of low-energy ions with high time resolution are indispensable for understanding the structure and dynamics of the magnetosphere. Because no full 3D low-energy ion data have been obtained

around Mercury, the low-energy ion data obtained by MIA together with MSA on Mio will provide unique opportunity for understanding the detailed structure and dynamics of the Mercury magnetosphere.

### 3.3.2 Operation Mode and Data Products of MIA

After its insertion into Mercury's orbit, MIA will continue its observation during all orbital phases except for periods in which MIA should be turned off owing to thermal/power constraints. Because the operation of all science instruments on Mio should be synchronized, the scientific operation of MIA obeys that of the Mio instrument suite. MIA has three operational modes: solar wind (SW), magnetospheric ion high angular resolution (MIHAR), and magnetospheric ion low angular resolution (MILAR) modes. The SW mode is used for fine angular resolution measurement of the solar wind around Mercury; the MIHAR mode is used for high angular resolution measurements of the Mercury magnetospheric ions; and the MILAR mode is used for low angular resolution measurements of the Mercury magnetospheric ions. These modes are changed depending on the satellite position and telemetry data rate by real-time commanding or stored commands. The MDP1 onboard software can also be used to change the mode. Table 8 shows the MIA operation mode and the data rate sent from MIA to MDP1. MIA always acquires data with a fixed sampling time of  $\sim 2$  ms, a fixed spin angular sector of  $5.625^\circ$  (64 equally divided spin sectors:  $360^\circ/64$  sectors =  $5.625^\circ$ ), and 64 ASIC channels. The 64 ASIC channels are connected to the 62-channel discrete anode that detects the position of the energy analyzed ions and an annular anode that is used for monitoring the high-energy particle background (Saito et al. 2017). One ASIC channel is left open to monitor the electrical background noise (Fig. 36). Therefore MIA always acquires  $64$  channels  $\times$   $64$  spin sectors  $\times$   $32$  energy steps =  $131072$  data for 1 spin.

Since this data quantity is too large for processing by MDP1, the FPGA in MIA will add adjacent counts (spin sectors and ASIC channels) depending on the MIA's data mode (modes 0, 1 and 2). The data sent from MIA to MDP1 are processed by MDP1 and the telemetry data are transmitted to the ground according to the MPPE data mode described in Sect. 4.

Table 9 shows six different MIA energy sweep modes. Mode 0 and 1 are used mainly for solar wind ion observation. The energy range between  $\sim 100$  eV/q and  $\sim 10$  keV/q is exponentially divided into 128 energy steps. To cover the full energy range, four spin-periods (nominally 16 s) are necessary. The difference between energy sweep modes 0 and 1 is that the sensitivity control function is either OFF or ON. For mode 1, the sensitivity is controlled by applying positive high voltage to the "top-cap" to reduce the G-factor. Energy sweep mode 2 is referred to as the MCP protection mode, which is used for protecting part of the MCP that detects ions from the analyzer azimuthal sector with no mechanical attenuation grid. The energy range is determined not to measure intense main component of the solar wind. Energy sweep modes 3, 4, and 5 are used mainly for magnetospheric ion observation. Energy sweep mode 3 is a "wide energy range mode" that covers the full energy range between  $\sim 20$  eV/q and  $\sim 25$  keV/q with 32 exponentially divided steps. Energy sweep mode 4 is a low energy range mode that covers the low energy range between  $\sim 20$  eV/q and  $\sim 5$  keV/q with 32 exponentially divided steps. Energy sweep mode 5 is a high energy range mode that covers the high-energy range between  $\sim 5$  keV/q and  $\sim 25$  keV/q with 32 exponentially divided steps. Different energy sweep modes can be selected for eight spin sector groups, where spin sector group 0 is from spin sector 0 to 7, group 1 is from spin sector 8 to 15, ..., and group 7 is from spin sector 56 to 63. Spin sector 0 occurs when the axis of rotational symmetry of MIA is pointing away from the Sun (Fig. 31). In this case, the

**Table 8** MIA operation mode

Mode	Produced data	Raw data rate
Solar Wind Mode (DATA MODE 1)	Count data 1) $(8 + 8^{*1}(22.5^\circ))$ polar sectors +2 background counters) $\times 8(22.5^\circ)$ equatorial sectors $\times 32$ energy steps/spin	Max. 245760 bps Average 98304 bps
	2) $(8 + 8^{*1}(22.5^\circ))$ polar sectors +2 background counters) $\times 8(11.25^\circ)$ equatorial sectors $\times 32$ energy steps/spin	16 bits/data
	3) $(8 + 4^{*2}(22.5^\circ))$ polar sectors +2 background counters) $\times 16(5.625^\circ)$ equatorial sectors $\times 32$ energy steps / spin (excluding 90 deg. $\times$ 90 deg. solar wind sector)	
	4) 16 polar sectors $\times$ 16 equatorial sectors $\times$ 128 energy steps/4spins (90 deg. $\times$ 90 deg. solar wind sector)	
Magnetospheric Ion High Angular Resolution Mode (DATA MODE 2)	count data $(16 + 16^{*3}$ polar sectors +2 background counters) $\times 32$ equatorial sectors $\times 32$ energy steps/spin	139264 bps 16 bits/data
Magnetospheric Ion Low Angular Resolution Mode (DATA MODE 3)	count data $(8 + 8^{*1}$ polar sectors +2 background counters) $\times 16$ equatorial sectors $\times 32$ energy steps/spin	36864 bps 16 bits/data

\*1 Sensitivity of about  $120^\circ$  in the eight polar sectors is reduced down to 1/50 with mechanical attenuation grid

\*2 Sensitivity of about  $30^\circ$  in the four polar sectors is reduced down to 1/50 with mechanical attenuation grid

\*3 Sensitivity of about  $120^\circ$  in the 16 polar sectors is reduced down to 1/50 with mechanical attenuation grid

solar wind channel with the mechanical attenuation grid observes solar wind at spin sector groups 1 and 2. Table 10 shows examples of the energy sweep mode allocated to the spin sector group. Numbers from 0 to 5 in the “waveform allocation” correspond to energy sweep modes 0 to 5 in Table 9.

The energy sweep of MIA is as follows: (1) 1 spin (4 s) is equally divided into 64 spin angle sectors; (2) 32 energy steps are swept in each spin angle sector resulting in a sampling time of  $4 \text{ s}/64 \text{ spin sectors}/32 \text{ energy steps} = \sim 2 \text{ ms}$ ; and (3) 128 energy steps are swept by accumulating 4-spin sets of 32 energy steps/spin. Figure 32 (left) shows an energy sweep waveform of MIA, specifically the voltage applied to the inner sphere for solar wind observation (energy sweep mode 0 or 1). In the solar wind, 4 spins are necessary to cover the full

1501 **Table 9** MIA energy sweep

Mode	Measurement	Sensitivity control	Spin/cycle	Energy range	
1504	0	Solar wind	OFF	4 (128 steps)	107 eV/q–10.3 keV/q
1505	1	Solar wind	ON	4 (128 steps)	123 eV/q–11.6 keV/q
1506	2	Solar wind	OFF	2 (64 steps)	28.0 eV/q–300 eV/q (32 steps)
1507			2 (64 steps)	3.10 keV/q–25.8 keV/q (32steps)	
1508	3	Magnetosphere	OFF	1 (32 steps)	24.0 eV/q–25.8 keV/q
1509	4	Magnetosphere	OFF	1 (32 steps)	21.0 eV/q–5.15 keV/q
1510	5	Magnetosphere	OFF	1 (32 steps)	5.17 keV/q–25.8 keV/q

1513 **Table 10** Examples of energy sweep—sector allocation of MIA

Sector group	0	1	2	3	4	5	6	7		
1515										
1516	Sector	0–7	8–15	16–23	24–31	32–39	40–47	48–55	56–63	
1517	No.	Waveform allocation <sup>a</sup> (Mode)								
1518										
1519	1	Solar wind	0	1	1	0	0	1	1	0
1520	2	Solar wind	0	1	1	0	0	2	2	0
1521	3	Magnetosphere	3	3	3	3	3	3	3	3
1522	4	Magnetosphere	4	4	4	4	4	4	4	4
1523	5	Magnetosphere	5	5	5	5	5	5	5	5

1525 <sup>a</sup>One spin is divided equally into 64 sectors. Half of the MIA with (without) the mechanical attenuation grid  
 1526 faces the solar wind direction in sectors 8–23 (40–55)

1529 energy range with 128 steps. The full energy range with 32 steps is covered in each spin (en-  
 1530 ergy coverage has some gaps). In this case, 32 steps in 4 different spins are slightly shifted so  
 1531 that 64 energy steps are covered with 2 consecutive spins, and 128 energy steps are covered  
 1532 with 4 consecutive spins. Concerning the attenuation factor, only one pre-defined “top-cap”  
 1533 voltage/inner sphere voltage ratio ( $V_i/|V_i| = 1.0$ ) is used because the G-factor varies too  
 1534 rapidly when the ratio exceeds 1.0. When we use energy sweep mode 1, the attenuation is  
 1535 applied to all energy steps to reduce the flux of the solar wind ions. Figure 32 (right) shows  
 1536 the voltage applied to the inner sphere and the “top-cap” for solar wind observation (energy  
 1537 sweep mode 1). Electrical attenuation is enabled by applying the same voltage to the inner  
 1538 sphere and the “top-cap”.

1539 According to the MIA mode (modes 1–3; Table 8), the MIA application in the MDPI  
 1540 continuously computes the VM data and energy spectra (Et) for the mission packets of the  
 1541 L-mode, whereas medium-resolution 3D distribution functions (3D-L2 or SW-L2) are gener-  
 1542 ated for the M-mode. The L-mode mission packets also contain 3D distribution functions  
 1543 (3D-LL), although they are provided in long intervals of (600–3600 s) (Table 11). For the H-  
 1544 mode mission packets, high-resolution 3D distribution functions (SW-L, 3D-L2, or 3D-H)  
 1545 are generated each spin (4 s). The VM consists of the density (n), net flux vector (nV), and  
 1546 pressure tensor (P), which are computed using a lookup table. The detailed format, size and  
 1547 rate of each data product shown in Table 11 are shown in Table 12. For the 3D count data  
 1548 products in the M-mode mission packets, 3D-L2-M1 and 3D-L2-M3, and in the H-mode  
 1549 mission packets, 3D-L2-M1, 89 directions (DIR) are selected from eight spin sectors (SC)

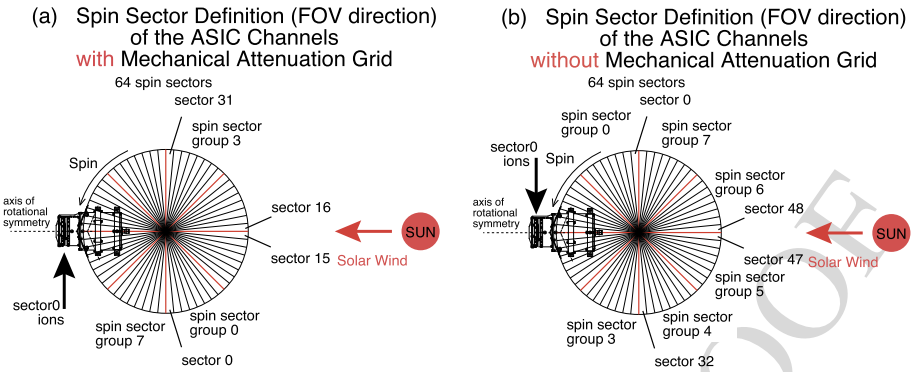


**Fig. 31** Definition of the spin sector 0. Spin Sector 0 is defined when the axis of the rotational symmetry of MIA (dashed line) is pointing away from the Sun. The ion flow direction observed at Spin Sector 0 is indicated by a black arrow and the solar wind ion flow direction is indicated by a red arrow. (a) The solar wind channel with mechanical attenuation grid observes solar wind at spin sector group 1 (from spin sector 8 to 15) and spin sector group 2 (from spin sector 16 to spin sector 23). (b) The other channels without the mechanical attenuation grid observe solar wind at spin sector group 5 (from spin sector 40 to 47) and spin sector group 6 (from spin sector 48 to spin sector 55)

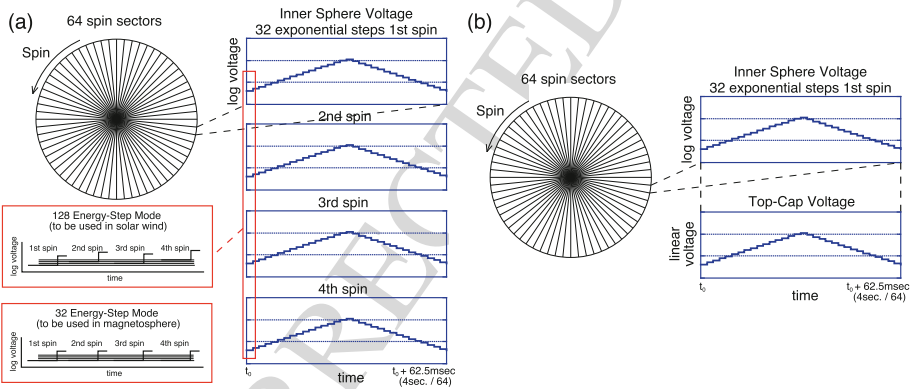


**Fig. 32** Energy sweep waveform of MIA. (a) When observing solar wind ions, 128 energy steps are swept by using 4 different 32 energy steps during 4 consecutive spins. (b) When electrical attenuation is enabled, the same voltages are applied to the inner sphere and the top-cap part

$\times 17$  channel (CH) directions. The VM consists of density  $n$ ; net flux vectors  $nV_x$ ,  $nV_y$ ,  $nV_z$ ; and pressure tensors  $P_{xx}$ ,  $P_{yy}$ ,  $P_{zz}$ ,  $P_{xy}$ ,  $P_{yz}$ ,  $P_{xz}$ . EN in the table represents energy.

### 3.3.3 Pre-flight Calibration of MIA

Pre-flight calibration of the MIA sensor was performed at a calibration facility at the Institute of Space and Astronautical Science/Japan Aerospace Exploration Agency (Wüest et al. 2007). MIA was installed in a vacuum chamber and nitrogen ions were injected. Figure 33 shows schematic diagram of the calibration experiment configuration. The sensor under calibration was installed on a rotation Table 1, which had a rotation axis parallel to the sensor's axis of rotational symmetry. This rotation table was installed on another rotation table ro-

1601 **Table 11** MIA mission data products in the L-mode, M-mode, and H-mode mission packets. Format of each  
 1602 product is shown in Table 12

1603 MIA operation mode

	MIA Mode 1	MIA Mode 2	MIA Mode 3
1606 L-mode	Et-M1 (32s), VM-M1 (4s, 16s)	Et-M2 (4s), VM-M2 (4s)	Et-M3 (4s), VM-M3 (4s)
1607	3D-LL-M1 (3600s)	3D-LL-M2 (3600s)	3D-LL-M3 (600s)
1608 M-mode	3D-L2-M1 (8s)	3D-L2-M2 (8s)	3D-L2-M3 (4s)
1609	(MPPE mode = 0-5)		(MPPE mode = 0-5)
1610 M-mode	SW-L2-M1 (4s)	3D-L2-M2 (8s)	3D-L2-M3 (8s)
1611	(MPPE mode = 6-8)		(MPPE mode = 6-8)
1612 H-mode	SW-L-M1 (4s), 3D-L2-M1 (4s)	3D-H-M2 (4s)	3D-H-M3 (4s)

1614 **Table 12** Format, size and rate of the MIA data products. For the 3D count data products, 89 directions  
 1616 (DIR) are selected from 8 spin sectors (SC) × 17 channel (CH) directions. Velocity moments (VM) consist of  
 1617 density (n), net flux (nV) (x, y, z), and pressure (P) (xx, yy, zz, xy, yz, xz). EN represents energy

1619 Products	1619 Format (16 bits)	1619 Size/rate
1620 Et-M1 (32s)	1621 8 bits × 128 (EN) 1622 (Solar wind direction)	640 B/160 bps
1623	1623 8 bits × 128 (EN) × 4 1624 (4-divided Omni direction)	
1625 Et-M2, 3 (4s)	1625 8 bits × 16 (EN) × 4 1626 (4-divided Omni direction)	64 B/128 bps
1627 VM-M1 (4s)	1627 16-bit float × 10 (VM) × 2 1628 (Solar wind and Omni)	40 B/80 bps
1629 VM-M2, 3 (4s)	1629 16-bit float × 10 (VM)	20 B/40 bps
1630 3D-LL-M1 (3600s)	1630 16-bit counter × 16 × 17 × 32 (SC, CH, EN)	17 kB/39 bps
1631 3D-LL-M2 (3600s)	1631 16-bit counter × 32 × 17 × 32 (SC, CH, EN)	35 kB/77 bps
1632 3D-LL-M3 (600s)	1632 16-bit counter × 16 × 9 × 32 (SC, CH, EN)	8 kB/110 bps
1633 3D-L2-M1 (8s)	1633 16-bit counter × 89 × 32 (DIR, EN) 1634 (Omni)	6 kB/6 kbps
1635 SW-L2-M1 (4s)	1635 16-bit counter × 4 × 17 × 32 (SC, CH, EN) 1636 (Solar wind)	4 kB/9 kbps
1637 3D-L2-M2 (8s)	1637 16-bit counter × 16 × 9 × 32 (SC, CH, EN)	9 kB/9 kbps
1638 3D-L2-M3 (8s)	1638 16-bit counter × 89 × 32 (DIR, EN)	6 kB/6 kbps
1639 3D-L2-M3 (4s)	1639 16-bit counter × 89 × 16 (DIR, EN)	3 kB/6 kbps
1640 SW-L-M1 (4s)	1640 16-bit counter × 16 × 17 × 32 (SC, CH, EN)	17 kB/35 kbps
1641 3D-L2-M1 (4s)	1641 16-bit counter × 89 × 32 (DIR, EN)	6 kB/11 kbps
1642 3D-H-M2 (4s)	1642 16-bit counter × 32 × 17 × 32 (SC, CH, EN)	35 kB/70 kbps
1643 3D-H-M3 (4s)	1643 16-bit counter × 16 × 17 × 32 (SC, CH, EN)	17 kB/34 kbps

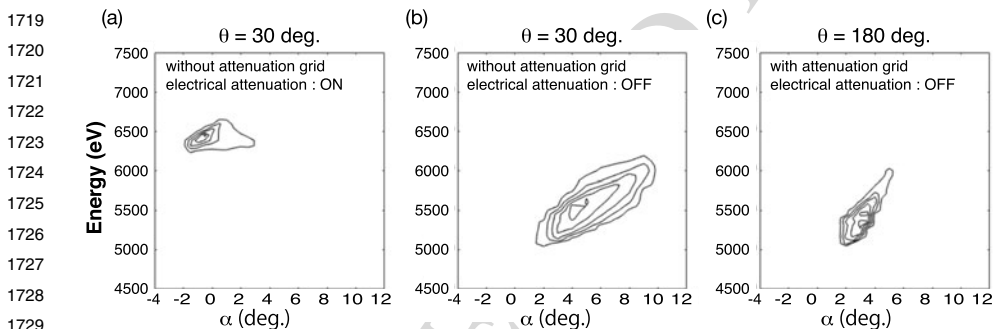
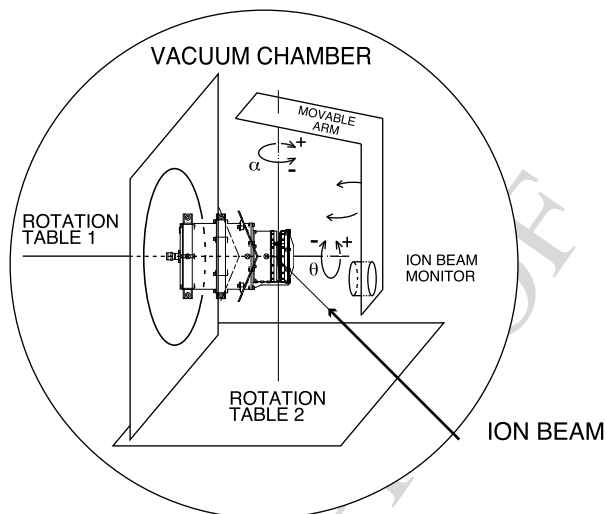
1644  
 1645  
 1646  
 1647 tation Table 2 in which the rotation axis was perpendicular to both the beam line and the  
 1648 rotation axis of rotation Table 1. Most of the data were obtained using 6 keV nitrogen ion  
 1649 beams because the beam profile was uniform and stable.

**Table 13** Summary of MIA performance

1651		
1652	Field of view	$3.8^\circ \times 90^\circ$ (high G-factor, solar wind)
1653		$5.1^\circ \times 90^\circ$ (low G-factor, solar wind)
1654		$9.6^\circ \times 270^\circ$ (high G-factor, Mercury ion)
1655		$6.4^\circ \times 270^\circ$ (low G-factor, Mercury ion)
1656		
1657	Angular resolution	$5.625^\circ \times 5.625^\circ$ (solar wind)
1658		$22.5^\circ \times 22.5^\circ$ (Mercury ion)
1659		
1660	Energy range	15 eV/q–29 keV/q
1661	Energy resolution	$\Delta E/E \sim 8.3\%$ (FWHM, high G-factor, solar wind)
1662		$\Delta E/E \sim 2.2\%$ (FWHM, low G-factor, solar wind)
1663		$\Delta E/E \sim 12.7\%$ (FWHM, high G-factor, Mercury ion)
1664		$\Delta E/E \sim 3.6\%$ (FWHM, low G-factor, Mercury ion)
1665		
1666	Time resolution	(32 energy steps) 4 s/3D distribution function
1667		(128 energy steps) 16 s/3D distribution function
1668		
1669	Geometrical factor	
1670	High G-factor mode	$3.39 \times 10^{-6} \text{ cm}^2 \text{ sr eV/eV}$ (solar wind)
1671	( $5.625^\circ$ :SW $22.5^\circ$ :MI)	$4.64 \times 10^{-4} \text{ cm}^2 \text{ sr eV/eV}$ (Mercury ion)
1672	Low G-factor mode	$2.81 \times 10^{-7} \text{ cm}^2 \text{ sr eV/eV}$ (solar wind)
1673	( $5.625^\circ$ :SW $22.5^\circ$ :MI)	$1.23 \times 10^{-5} \text{ cm}^2 \text{ sr eV/eV}$ (Mercury ion)
1674	Mass	1.57 kg
1675	Power	2.96 W
1676		
1677	Dimensions	180 mm $\times$ 254 mm $\times$ 146 mm
1678		
1679	Data rate	0.11 kbits/s (L-mode)
1680		2.5 kbits/s (M-mode)
1681		17 kbits/s (H-mode)
1682		after factor 3 compression

Table 13 gives a summary of MIA performance data determined by pre-flight calibration. The definition for the quantities in this table is general and is the same as that used by Wüest et al. (2007). Figure 34(a) and (b) compares the E- $\alpha$  characteristics of MIA with and without electrical attenuation. When electrical attenuation is enabled, both the angular spread and energy spread become narrower and the measured ion energy increases. Since angular resolution and energy resolution become higher, electrical attenuation is appropriate for solar wind ion observation. The G-factor is reduced to about 1/50 where the mechanical attenuation grid is installed. Figure 34(b) and (c) compares the E- $\alpha$  characteristics of MIA with and without a mechanical attenuation grid. It is clear that part of the E- $\alpha$  contour with large  $\alpha$  angle is reduced by the mechanical attenuation grid. Because the attenuation grid is placed only at the bottom part of the entrance aperture and the upper part is closed as shown in Fig. 29, the ions entering MIA with large  $\alpha$  angles are blocked. Consequently, the center of the measured  $\alpha$  angle becomes smaller and that of the measured energy becomes lower compared to those without a mechanical attenuation grid.

1701 **Fig. 33** Schematic diagram  
 1702 showing the configuration of  
 1703 MIA calibration. Rotation  
 1704 Table 1 is installed on Rotation  
 1705 Table 2. The ion entrance angles  
 1706  $\alpha$  and  $\theta$  with the definitions of  
 1707 their positive and negative  
 1708 directions are shown

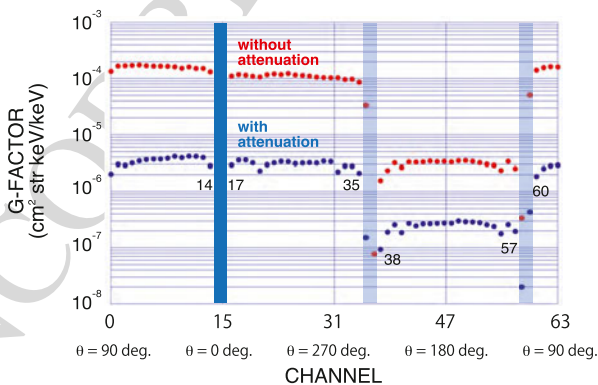
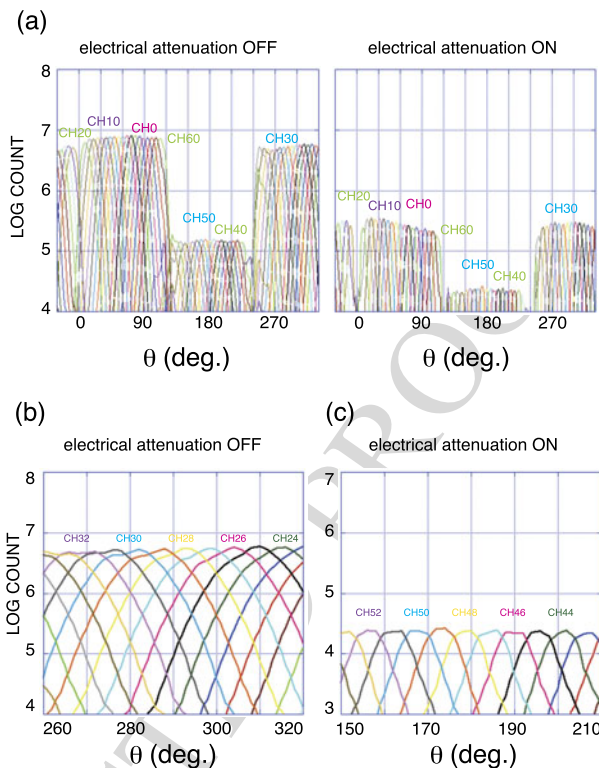


1720 **Fig. 34** Examples of  $E$ - $\alpha$  contour. An ion beam with a sufficiently large area was injected at  $\theta = 30^\circ$  for  
 1721 panels (a) and (b) and  $\theta = 180^\circ$  for panel (c). The counts are normalized by the maximum count in each  
 1722  $E$ - $\alpha$  contour; five contour lines with levels of 0.1, 0.3, 0.5, 0.7 and 0.9 are shown. (a) Without the mechanical  
 1723 attenuation grid; the electrical attenuation is ON. (b) Without the mechanical attenuation grid; the electrical  
 1724 attenuation is OFF. (c) With the mechanical attenuation grid; the electrical attenuation is OFF

1736 Figure 35(a) shows the  $\theta$  (azimuthal angle) resolution of MIA. The  $\theta$  angle coverage  
 1737 of all anode channels are shown when electrical attenuation is OFF (left panel) and ON  
 1738 (right panel). It is clear that the sensitivity is reduced where the mechanical attenuation grid  
 1739 is installed at the entrance of the analyzer (CH38–CH57). Figure 35(b) and (c) shows the  
 1740  $\theta$  angle coverage in greater detail. When the electrical attenuation is ON (panel (c)), the  
 1741  $\theta$  angular resolution becomes much higher than that when the electrical attenuation OFF  
 1742 (panel (b)).

1743 Figure 36 shows the G-factor of MIA for all 64 channels. MIA has physical supports  
 1744 across the entrance aperture every  $120^\circ$ . The light and thick blue boxes indicate the chan-  
 1745 nels affected by these physical supports (CH15, CH16, CH36, CH37, CH58 and CH59).  
 1746 The G-factor is reduced to about  $1/50$  where the mechanical attenuation grid is installed  
 1747 (CH38–CH57). Although the geometrical attenuation factor of the mechanical grid is  $1/10$   
 1748 (Fig. 29(c)), the G-factor reduction is  $\sim 1/50$  because the mechanical grid also changes  
 1749 the angular and energy characteristics of MIA as shown in Fig. 34. Slight variation of the

1751 **Fig. 35**  $\theta$  (azimuthal angle)  
 1752 resolution of MIA. (a) The  $\theta$   
 1753 angle coverage of each anode  
 1754 channel is shown (left panel:  
 1755 electrical attenuation OFF; right  
 1756 panel: electrical attenuation ON).  
 1757 (b) The  $\theta$  angle coverage of  
 1758 anode channels CH23–CH34  
 1759 without the mechanical  
 1760 attenuation grid and the electrical  
 1761 attenuation is OFF. (c) The  $\theta$   
 1762 angle coverage of anode channels  
 1763 CH42–CH53 with the  
 1764 mechanical attenuation grid and  
 1765 the electrical attenuation is ON



1791 **Fig. 36** Geometrical factor of MIA. Red dots show G-factor without electrical attenuation. Blue dots show G-  
 1795 factor with electrical attenuation (energy sweep mode 1). The light and thick blue boxes indicate the channels  
 1796 affected by the physical supports across the entrance aperture. Channel 15 is connected to an annular anode  
 1797 where no ions from the analyzer are expected to enter for monitoring the background count (Saito et al.  
 1798 2017). Channel 16, which is not connected to an anode is used to monitor the electrical background noise.  
 1799 The relationship between the ion entrance angle  $\theta$  (Fig. 33) and the corresponding ASIC channel is also  
 1800 shown

1801 G-factor also exists among the different channels without the mechanical attenuation grid  
1802 with large values around CH0 and small values around CH31. The variation of the analyzer  
1803 constant was also occurred simultaneously with the variation of the G-factor. This variation  
1804 can be explained by the slight inclination of the inner sphere with respect to the outer sphere  
1805 where the inclination angle was as small as  $0.2^\circ$  that is within the manufacturing tolerance.  
1806

### 1807 3.3.4 Near-Earth Commissioning Results of MIA

1808

1809 The low voltage part of MIA was turned on for the first time on November 25, 2018, about  
1810 one month after the launch. No problems were identified during the low voltage function  
1811 tests, which included calibration pulse injection into all channels of the pre-amplifier.

1812 The high voltage tests were performed on July 3 and 4, 2019, about eight months after  
1813 the launch when Mio was in the solar wind. High voltage up to +2500 V, -3610 V, and  
1814 -2471 V were successfully tested for stepping high voltage power supply connected to the  
1815 “top-cap” (SVG), stepping high voltage power supply connected to the inner sphere (SVS),  
1816 and high voltage power supply connected to the MCP detector (MHV), respectively. Dark  
1817 counts of the MCP were observed indicating that the detector part of MIA was function-  
1818 ing normally. Because Mio is surrounded by the MMO Sunshield and Interface Structure  
1819 (MOSIF) during the cruise phase, most parts of the MIA’s FOV is blocked by MOSIF. Al-  
1820 though all of the high voltage necessary for observation were successfully applied to MIA,  
1821 no solar wind ion signature was observed because the solar wind ion thermal velocity was  
1822 much lower than its bulk velocity, and MOSIF blocked the solar wind ions to enter MIA.

1823 Because MIA is able to measure hot plasmas in the magnetospheres of Earth and Mercury  
1824 and near-Venus when the plasma thermal velocity is higher than its bulk velocity, MIA  
1825 will be turned on during the Earth fly-by and the Venus/Mercury fly-bys before arriving at  
1826 Mercury in December 2025.  
1827

## 1828 3.4 MSA

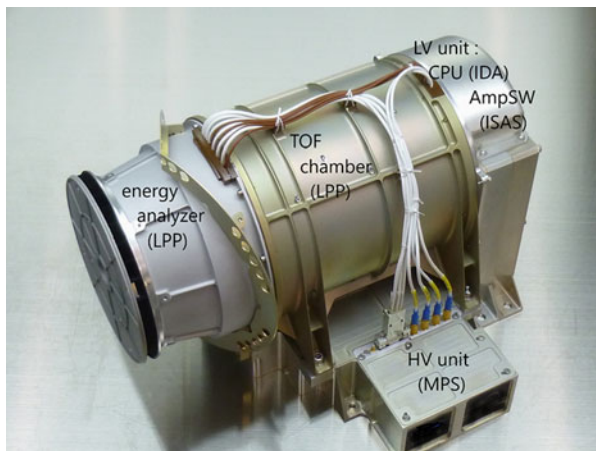
1829

### 1830 3.4.1 Instrument Description of MSA

1831

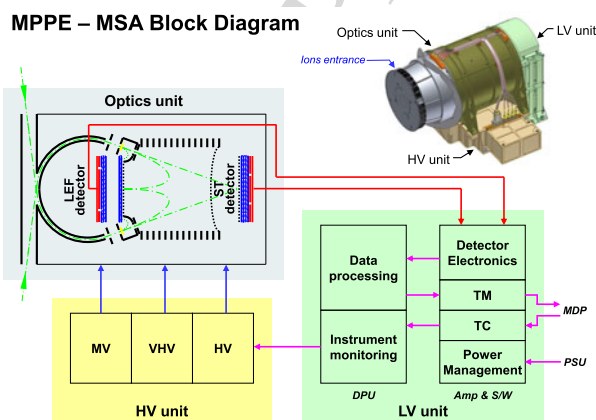
1832 MSA, part of the MPPE particle consortium, is dedicated to plasma composition measure-  
1833 ment onboard Mio (Delcourt et al. 2016). The main objectives of this instrument are (1) to  
1834 study the role and efficiency of the solar wind and planetary surface as sources of plasma  
1835 for the Hermean magnetosphere; (2) to study the transport, acceleration and loss of plasma  
1836 in the Hermean magnetosphere, particularly for investigating the dynamics of heavy ions of  
1837 planetary origin that have large gyroradii and large gyroperiods as compared to the charac-  
1838 teristic scales of the magnetosphere; (3) to contribute to the understanding of magnetosphere  
1839 electrodynamics, substorms, and the nature of current carriers; (4) to analyze the interaction  
1840 of magnetospheric plasma with the planetary surface and to study the processes by which  
1841 particles escape from the surface and access the magnetosphere; (5) to provide data that  
1842 will help to identify Mercury’s surface composition; (6) to monitor the solar wind and to  
1843 study interstellar pick-up ions. To achieve these issues, MSA will provide 3D distribution  
1844 functions in one Mio spin (4 s). In addition, in contrast to Earth where ions of planetary  
1845 origin are essentially  $O^+$  and  $He^+$ , a wide variety of species populate Mercury’s magneto-  
1846 sphere owing to various interaction processes with the planet surface (such as solar wind  
1847 sputtering, micro-meteoritic bombardment, and thermal desorption). To characterize these  
1848 populations, a spectrometer with enhanced mass resolution capability is necessary; hence,  
1849 the “reflectron” design was adopted for MSA.  
1850

1851 **Fig. 37** MSA flight model  
 1852 delivered to Mio system in June  
 1853 2014



1854  
1855  
1856  
1857  
1858  
1859  
1860  
1861  
1862  
1863  
1864  
1865  
1866

1867 **Fig. 38** Block diagram of MSA

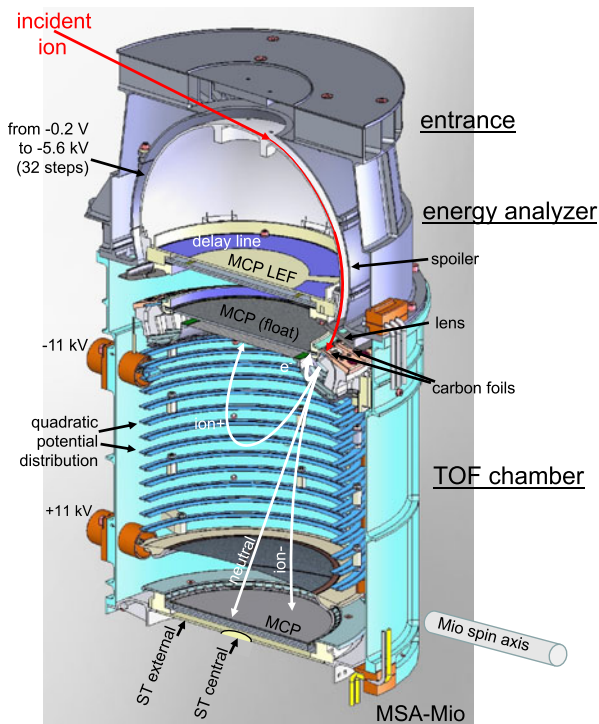


1868  
1869  
1870  
1871  
1872  
1873  
1874  
1875  
1876  
1877  
1878  
1879  
1880  
1881  
1882

1883 As summarized in Fig. 37, MSA is the result of collaboration of four different teams:  
 1884 (1) ISAS (Sagamihara, Japan; PI), which provided the amplifier board and spacewire  
 1885 interface; (2) LPP (Palaiseau, France; Co-PI), which provided the electrostatic optics;  
 1886 (3) MPS (Göttingen, Germany), which provided the high voltage power supplies; and  
 1887 (4) IDA (Braunschweig, Germany), which provided the dedicated central processing unit  
 1888 (CPU) board. A block diagram of MSA is shown in Fig. 38. MSA has dimensions of  
 1889 325 mm × 287 mm × 232 mm, a weight of 4.46 kg, and medium telemetry mode power  
 1890 of 9.1 W.

1891 This instrument, which is derived from CAPS-IMS onboard CASSINI (Young et al.  
 1892 2004), consists of a 2D mass spectrometer of cylindrical symmetry with respect to the  
 1893 main axis as illustrated in Fig. 39. It operates over a large energy range of  $\sim 1$  eV/q to  $\sim 38$  keV/q  
 1894 with an instantaneous FOV of  $5^\circ \times 260^\circ$ . The MSA entrance (blackened for UV rejection)  
 1895 features 32 angular sectors of  $11.25^\circ$ , 9 of which are blinded by the Mio magnetometer mast.  
 1896 After MSA entrance, a spherical analyzer enables measurement of the full range of ion en-  
 1897 ergies in 1/32 of Mio spin. The grounded external electrode of this analyzer is designed  
 1898 in three mechanical parts, including polarization of the central one leading to de-focusing  
 1899 (thus, effective control) of the incoming ion flux. After the energy analysis, ions are ac-  
 1900

**Fig. 39** Schematic illustration of MSA principles

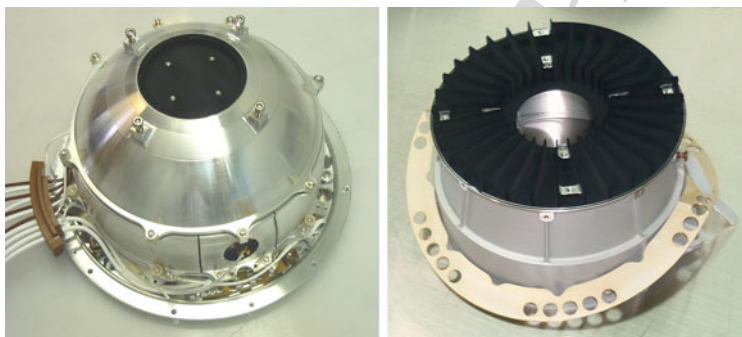
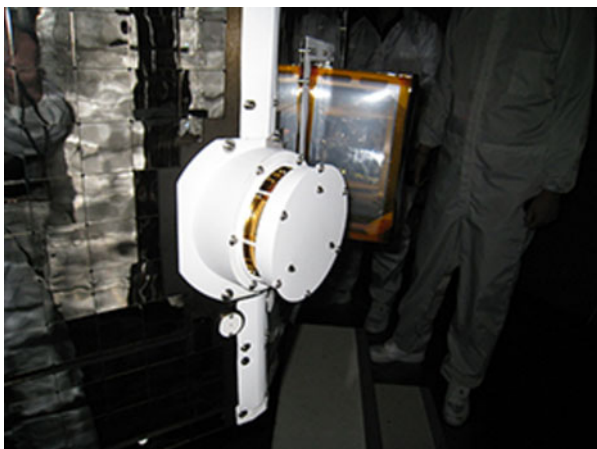


celerated ( $\pm 12$  kV in maximum operation voltage) toward a time of flight (TOF) chamber polarized with a linear electric field (LEF) along the instrument's main axis. This leads to isochronous (independent of energy) TOF for reflected ions up to  $\pm 12$  keV for maximum operation voltage (Delcourt et al. 2016), hence, enhanced mass resolution ( $m/\Delta m > 40$ ) over a large range of masses up to 60 amu. The straight-through (ST) particles are collected at the bottom end of the MSA TOF chamber, and a lower mass resolution is obtained that is somewhat improved using the central detector with reduced path lengths rather than the external one (Fig. 39). Details of the TOF signal of MSA has been described by Saito et al. (2017).

Figure 40 shows the thermal shield of MSA. Some selected parts of the MSA electrostatic optics are shown in Figs. 41 and 42. In particular, Fig. 42 shows the 21 angular sectors of entry equipped with carbon foils at the TOF chamber entrance. This figure also shows the bi-metallized Hamamatsu MCP at the back of the energy analyser, which enables differentiation of the MCP gain on the outer edge, where START electrons are collected, from that in the inner part, where LEF counts are obtained.

The MSA high voltage power Supply (HVPS Figs. 43 and 44) has 10 different sub-units supplying voltages of 30 V to  $\pm 12$  kV. These voltages can be individually modified by commands during flight. A radiation hard Actel RTSX FPGA controls the output-voltage of each sub-unit, whereas monitoring and commanding of the voltages are performed by the MSA CPU. The sub-units comprise the power supplies for (i) the 2 MCP stacks of MSA, (ii) the adjustable MCP anode-voltages, (iii) the two flux spoilers, (iv) MSA reflectron with an operational voltage range up to  $\pm 12$  kV, and (v) a stepping voltage for the energy analyzer with a dynamic range between 0.1 V and 5.6 kV and a settling time  $< 1$  ms.

1951 **Fig. 40** Thermal shield of MSA



1979 **Fig. 41** Copper sulfide blackened energy analyzer (left) and entrance section (right)

1980  
1981  
1982 **Fig. 42** Energy analyzer (left,  
1983 viewed from the back), and TOF  
1984 chamber (right, view from top)



1997 The CPU (Figs. 45 and 46) performs instrument control and dedicated data process-  
1998 ing. The advanced design is based on the AT697, a 48 MHz LEON2-FT fault tolerant  
1999 SPARC processor architecture implemented in radiation hard ASIC, including Triple Mod-  
2000

2001  
2002  
2003  
2004  
2005  
2006  
2007  
2008  
2009  
2010  
2011  
2012  
2013  
2014  
2015  
2016  
2017  
2018  
2019  
2020  
2021  
2022  
2023  
2024  
2025  
2026  
2027  
2028  
2029  
2030  
2031  
2032  
2033  
2034  
2035  
2036  
2037  
2038  
2039  
2040  
2041  
2042  
2043  
2044  
2045  
2046  
2047  
2048  
2049  
2050

**Fig. 43** MSA HPVS (top view)

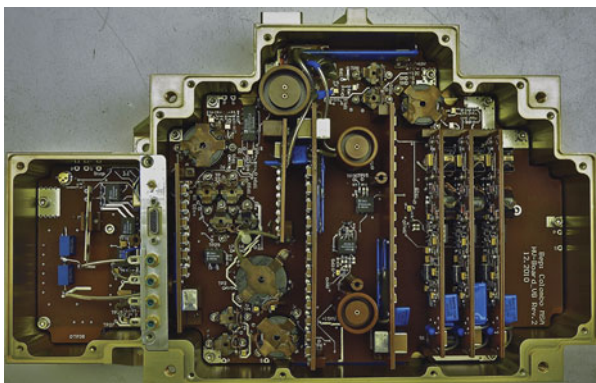


**Fig. 44** MSA HVPS (bottom view)

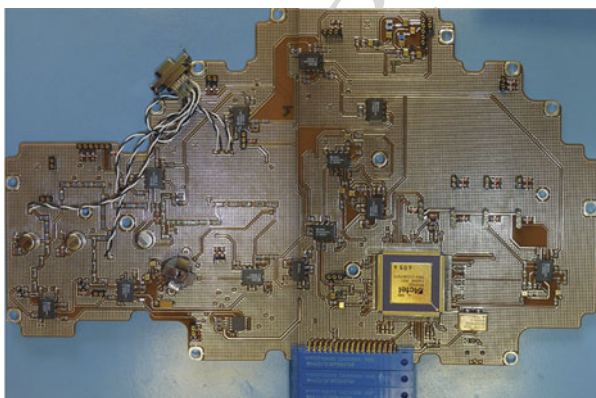
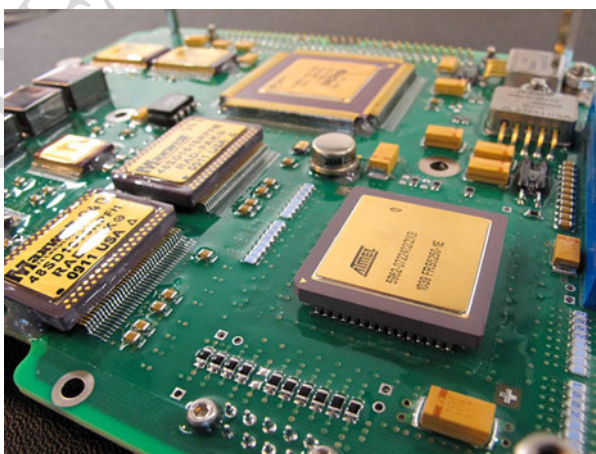
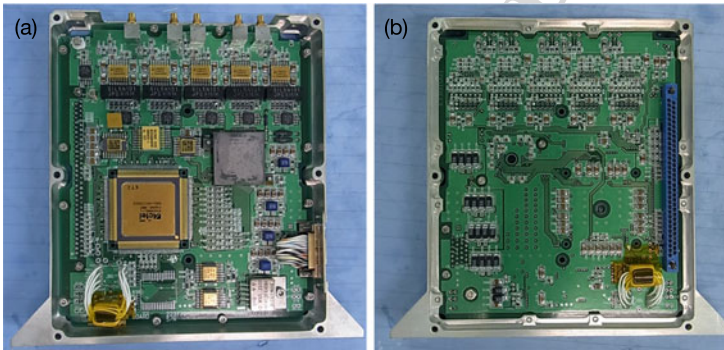
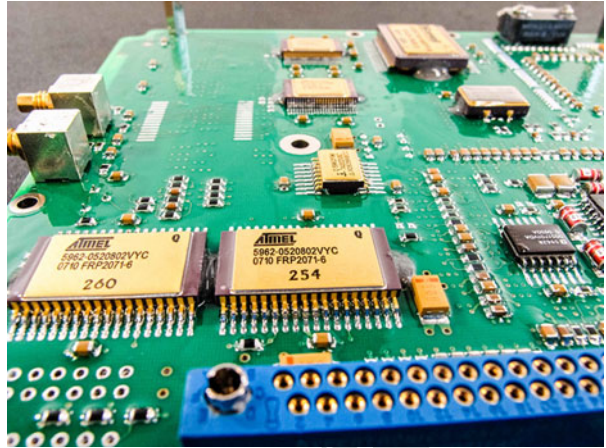


**Fig. 45** MSA CPU (top view)



ular Redundancy (TMR) and advanced Error Detection And Correction (EDAC) against SEU errors. Together with a radiation hardened, one-time programmable FPGA (Microsemi RTAX), the processor is employed for high-level instrument control and monitoring, control of sensor electronics and compression of scientific data. All internal interfaces and glue

2051 **Fig. 46** MSA CPU (bottom  
2052 view)



2068 (a) 2069 (b)  
2070  
2071  
2072  
2073  
2074  
2075  
2076  
2077  
2078  
2079 **Fig. 47** MSA TOF signal amplifiers and SpaceWire interface. (a) top view (b) bottom view

2080  
2081  
2082  
2083 logic are embedded in the radiation hardened RTAX system FPGA to achieve the highest  
2084 reliability. Program code images can be uploaded to the non-volatile memory and executed  
2085 in the EDAC protected SDRAM module.

2086 Figure 47 shows the top view (panel (a)) and bottom view (panel (b)) of the amplifier  
2087 board and spacewire interface. Five charge signals from the MCP anodes are fed into five  
2088 fast transistor amplifiers and the amplified signals are discriminated by constant fraction  
2089 discriminators. A custom gate array with a titanium radiation shield calculates and buffers  
2090 the signal timing with a time resolution of 781.25 ps. An FPGA Actel RTAX2000 that  
2091 communicates with the CPU interfaces with MDP1, controls the custom gate array, and  
2092 processes the signal timing calculated by the custom gate array.

2093 The performance of the MSA instrument are given in Table 14. Its capability is summa-  
2094 rized as follows. (1) ST data: high temporal resolution, high sensitivity measurements and  
2095 medium mass resolution ( $m/\Delta m$  up to  $\sim 10$ ) to focus on major ion species and allow rapid  
2096 analysis of magnetospheric phenomena, which makes MSA appropriate for plasma analysis.  
2097 (2) LEF data: high mass resolution measurements with  $m/\Delta m$  up to 60 for ions with ener-  
2098 gies smaller than the MSA operation voltage, up to a maximum of 12 kV because ions with  
2099 larger energies cannot be turned around by the LEF and are detected on the ST MCP. This  
2100

**Table 14** Summary of MSA performance

2101	Field of view	$5^\circ \times 260^\circ$
2102	Angular resolution	$5^\circ \times 11.25^\circ$
2103	Energy range	1 eV/q–38 keV/q
2104	Energy resolution	$\Delta E/E = 8\%$
2105	k-factor	6.85
2106	Mass range	1–60 amu
2107	Mass resolution	$m/\Delta m > 40$ (< 13 keV/q)
2108		$m/\Delta m = 10$ (> 13 keV/q)
2109	Time resolution	3D distribution function in 4 s
2110		(32 energy steps)
2111		3D distribution function in 8 s
2112		(64 energy steps)
2113	Geometrical factor (21 windows)	$7 \times 10^{-3} \text{ cm}^2 \text{ sr eV/eV (ST)}$
2114		$5 \times 10^{-4} \text{ cm}^2 \text{ sr eV/eV (LEF)}$
2115	Mass	4.46 kg
2116	Power	9.1 W
2117	Dimensions	325 mm $\times$ 287 mm $\times$ 232 mm
2118	Data rate	0.15 kbits/s (L-mode)
2119		1.4 kbits/s (M-mode)
2120		25 kbits/s (H-mode)
2121		after factor 10 compression
2122		
2123		
2124		

process focuses on ions of planetary origin and enables precise composition measurement, which demonstrates the appropriateness of MSA for planetology studies.

### 3.4.2 Operation Mode and Data Products of MSA

MSA energy sampling features 32 energy steps over the full energy range (1 eV/q to 38 keV/q) of the instrument during one spin sector:  $1/32$  spin = 125 ms. To more effectively cover the wide energy range of MSA, two distinct sets of interleaved energy steps are used during two consecutive spins. At the exit of the energy analyzer, ions enter the TOF chamber, and secondary electrons collected as START pulses are emitted upon crossing the carbon foils. Upon impact of the ions on either the LEF or ST detectors, STOP pulses are recorded and the resulting coincidences (i.e., the given STOP signal associated with the given START signal) provide information on the particle TOF or, equivalently, on their mass to charge (m/q) ratio.

Owing to the differences in ST and LEF spectra, two different approaches are implemented. For LEF particles, TOF spectra with  $2 \times 32$  energies (corresponding to the two distinct sets of interleaved steps described above) are produced every 16 spins (64 s). For ST particles, once the STOP-START calculations are completed, allocation of the ion mass is performed onboard using fixed mass groups. In total, 15 count rate matrices are built. The first four are “all ions” or “all START counts”,  $\text{H}^+$ ,  $\text{He}^{2+}$ , and heavy ions including all ions with m/q ratios larger than 2. These matrices are produced at each 4 s interval and only these first four count rate matrices are transmitted in the Mio low telemetry mode. The next 11 count rate matrices relate to  $\text{He}^+$ ,  $\text{C}^-$ ,  $\text{O}^-$ , C, N, O, Na, Si, S, K, and Fe ions and are produced at each 16 spins (64 s). Please note that negative ions here are not external ions (the voltage configuration of MSA energy analyzer does not admit negative ions) but ions

2151  
2152  
2153  
2154  
2155  
2156  
2157  
2158  
2159  
2160  
2161  
2162  
2163  
2164  
2165  
2166  
2167  
2168  
2169  
2170  
2171  
2172  
2173  
2174  
2175  
2176  
2177  
2178  
2179  
2180  
2181  
2182  
2183  
2184  
2185  
2186  
2187  
2188  
2189  
2190  
2191  
2192  
2193  
2194  
2195  
2196  
2197  
2198  
2199  
2200

**Table 15** MSA normal operation mode. M#: count rate matrix of given ion species; A: anode (or entrance window); S: spin sector (32 in one spin); E: energy step (32 in one spin sector); V: velocity direction (36 view directions); T: time of flight

Name	Content	Internal (32 bit)		External (16 bit)		Time resolution	
		Dimension	kbit	Dimension	kbit	Int	Med
M0	Starts	32S×32E×21A	688	36V×64E	37	4 s	24 s
A0	Starts			21A×32S	11	64 s	256 s
M1	Protons	32S×32E×21A	688	36V×64E	37	4 s	24 s
M2	He <sup>++</sup>	32S×32E×21A	688	36V×64E	37	4 s	48 s
M3	HeavyIons	32S×32E×21A	688	36V×64E	37	4 s	48 s
M4	OtherIons	32S×64E×21A	1376	36V×64E	37	64 s	256 s
M5	OtherIons	32S×64E×21A	1376	36V×64E	37	64 s	256 s
M6	OtherIons	32S×64E×21A	1376	36V×64E	37	64 s	256 s
M7	OtherIons	32S×64E×21A	1376	36V×64E	37	64 s	256 s
M8	OtherIons	32S×64E×21A	1376	36V×64E	37	64 s	256 s
M9	OtherIons	32S×64E×21A	1376	36V×64E	37	64 s	256 s
M10	OtherIons	32S×64E×21A	1376	36V×64E	37	64 s	256 s
M11	OtherIons	32S×64E×21A	1376	36V×64E	37	64 s	256 s
M12	OtherIons	32S×64E×21A	1376	36V×64E	37	64 s	256 s
M13	OtherIons	32S×64E×21A	1376	36V×64E	37	64 s	256 s
M14	OtherIons	32S×64E×21A	1376	36V×64E	37	64 s	256 s
M15	OtherIons	32S×64E×21A	1376	36V×64E	37	64 s	256 s
TSTC	STC TOF	64E×1024T	2097	32E×1024T	524	64 s	256 s
TSTE	STE TOF	64E×1024T	2097	32E×1024T	524	64 s	256 s
TLEF	LEF TOF	64E×2048T	4194	8E×2048T	262	64 s	256 s
<b>SUM</b>			<b>27652</b>		<b>1913</b>		

produced via charge exchange during crossing of the carbon foil (e.g., Funsten et al. 2001). Using this mass identification, the moments are subsequently calculated by MSA DPU (assuming Na mass for heavy ions because this latter group of ions corresponds to all ions with m/q ratios larger than 2).

MSA internal products thus contain two types of count rate matrices: (i) TOF matrices with no angular information for LEF data, and (ii) mass matrices as described above for ST data. These internal matrices are then transformed to external matrices for telemetry. In the latter matrices, energy sampling is reduced to eight steps in the LEF data. For ST data, angular resolution is reduced to 36 view directions per spin. These external matrices are then transmitted according to different modes selected on a scientific basis; normal mode (default mode) as described in Table 15, high angular resolution mode (Table 16), and high time resolution mode (Table 17). Other modes (not shown) include event mode and burst mode (similar to Table 17 but with a higher production frequency).

The data downlink includes three distinct telemetry rates for Mio data: L-mode (L) available most of the time, M-mode (M) during ~ 25% of the time, and H-mode (H) in some very limited portions of the Mio orbit. MSA is part of the MPPE particle consortium; thus, the data modes are defined for specific MPPE science research targets (e.g., survey mode, solar wind or exosphere dedicated modes, reconnection mode) which is consistent with the modes adopted for the other particle instruments. Table 18 shows the MSA data that will

**Table 16** MSA high spatial resolution mode

Name	Content	Internal (32 bit)		External (16 bit)		Time resolution	
		Dimension	kbit	Dimension	kbit	Int	Med
M0	Starts	32S×32E×21A	688	21A×32S×2E	21	4 s	16 s
M1	Protons	32S×32E×21A	688	21A×32S×4E	43	4 s	16 s
M2	He <sup>++</sup>	32S×32E×21A	688	21A×32S×4E	43	4 s	48 s
M3	HeavyIons	32S×32E×21A	688	21A×32S×4E	43	4 s	48 s
M4	OtherIons	32S×64E×21A	1376	21A×32S×4E	43	64 s	256 s
M5	OtherIons	32S×64E×21A	1376	21A×32S×4E	43	64 s	256 s
M6	OtherIons	32S×64E×21A	1376	21A×32S×4E	43	64 s	256 s
M7	OtherIons	32S×64E×21A	1376	21A×32S×4E	43	64 s	256 s
M8	OtherIons	32S×64E×21A	1376	21A×32S×4E	43	64 s	256 s
M9	OtherIons	32S×64E×21A	1376	21A×32S×4E	43	64 s	256 s
M10	OtherIons	32S×64E×21A	1376	21A×32S×4E	43	64 s	256 s
M11	OtherIons	32S×64E×21A	1376	21A×32S×4E	43	64 s	256 s
M12	OtherIons	32S×64E×21A	1376	21A×32S×4E	43	64 s	256 s
M13	OtherIons	32S×64E×21A	1376	21A×32S×4E	43	64s	256 s
M14	OtherIons	32S×64E×21A	1376	21A×32S×4E	43	64 s	256 s
M15	OtherIons	32S×64E×21A	1376	21A×32S×4E	43	64 s	256 s
TSTC	STC TOF	64E×1024T	2097	32E×1024T	524	64 s	256 s
TSTE	STE TOF	64E×1024T	2097	32E×1024T	524	64 s	256 s
TLEF	LEF TOF	64E×2048T	4194	8E×2048T	262	64 s	256 s
<b>SUM</b>			<b>27652</b>		<b>1976</b>		

be transmitted in the various Mio telemetry regimes depending upon the targeted research (Medium A for survey, Medium C for solar wind or exosphere analysis). Since the MSA possesses a CPU board that processes the mission data into the mission products such as moment data, the MSA application in the MDP1 relays them to the data recorder. The MSA application removes the dummy data and packs only effective data into the mission packets.

### 3.4.3 Pre-flight Calibration of MSA

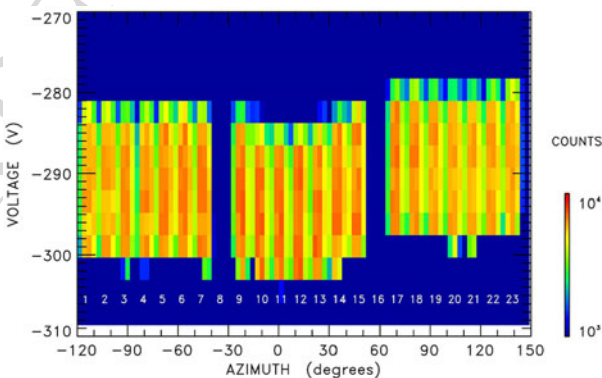
Because the MSA instrument is a collaborative effort between four different teams, both the Flight Model and the Spare Model were assembled at the PI institute (ISAS, Sagami-hara, Japan). Numerous test campaigns including pre-flight calibration were subsequently conducted at this institute. The present section provides a summary of the calibration results.

Downstream of the MSA entrance, ions travel through the spherical energy analyser, which has an external electrode at ground potential. On the inner electrode of the analyzer, the voltage applied varies up to a maximum value of  $-5.6$  kV, which enables selection of ions with specific energy per charge ( $E/q$ ) ratios. This is illustrated in Fig. 48, which shows the voltage applied to this inner electrode for a  $2$  keV  $N^+$  beam. In the figure, the voltage median value is approximately  $-292$  V, yielding an analyzer constant  $k$  of  $\sim 6.85$ . With minimum and maximum voltages of  $-0.2$  V and  $-5.6$  kV, respectively, MSA can thus operate from a few electron volts per charge ( $eV/q$ ) up to  $\sim 38$  keV/ $q$ . The figure also shows a modulation of the ion count rate within each of the 21 entrance windows owing to the partition walls at each  $11.25^\circ$  step. Further analysis of the energy analyzer response revealed

**Table 17** MSA high time resolution mode

Name	Content	Internal (32 bit)		External (16 bit)		Time resolution	
		Dimension	kbit	Dimension	kbit	Int	Med
M0	Starts	32S×32E×21A	688	36V×32E	18	4 s	8 s
A0	Starts			21A×32S	11	64 s	64 s
M1	Protons	32S×32E×21A	688	36V×32E	18	4 s	8 s
M2	He++	32S×32E×21A	688	36V×16E	9	4 s	12 s
M3	HeavyIons	32S×32E×21A	688	36V×16E	9	4 s	12 s
M4	OtherIons	32S×64E×21A	1376	36V×16E	9	64 s	64 s
M5	OtherIons	32S×64E×21A	1376	36V×16E	9	64 s	64 s
M6	OtherIons	32S×64E×21A	1376	36V×16E	9	64 s	64 s
M7	OtherIons	32S×64E×21A	1376	36V×16E	9	64 s	64 s
M8	OtherIons	32S×64E×21A	1376	36V×16E	9	64 s	64 s
M9	OtherIons	32S×64E×21A	1376	36V×16E	9	64 s	64 s
M10	OtherIons	32S×64E×21A	1376	36V×16E	9	64 s	64 s
M11	OtherIons	32S×64E×21A	1376	36V×16E	9	64 s	64 s
M12	OtherIons	32S×64E×21A	1376	36V×16E	9	64 s	64 s
M13	OtherIons	32S×64E×21A	1376	36V×16E	9	64 s	64 s
M14	OtherIons	32S×64E×21A	1376	36V×16E	9	64 s	64 s
M15	OtherIons	32S×64E×21A	1376	36V×16E	9	64 s	64 s
TSTC	STC TOF	64E×1024T	2097	4E×1024T	65	64 s	64 s
TSTE	STE TOF	64E×1024T	2097	4E×1024T	65	64 s	64 s
TLEF	LEF TOF	64E×2048T	4194	2E×2048T	65	64 s	64 s
<b>SUM</b>			<b>27652</b>		<b>368</b>		

**Fig. 48** Color-coded count rate as functions of azimuth and voltage applied on the inner sphere of the energy analyzer for a 2 keV N<sup>+</sup> beam



energy resolution of  $\sim 8.5\%$ . Finally, the figure shows the MSA response as a function of azimuth or, equivalently, the entrance windows. In the other dimension (i.e., elevation or polar angle), the MSA FOV is centered at  $\sim 5^\circ$  with an angular resolution (full width at half maximum, FWHM) of  $\sim 5^\circ$ . This is illustrated in Fig. 49, which shows particle counts versus voltage and polar angle (elevation).

At exit of the energy analyzer, ions are accelerated toward the entrance of the TOF chamber with nominal operation voltages of  $\pm 11$  kV corresponding to 85% of the MSA quali-

2301 **Table 18** MSA data for the different Mio telemetry regimes

2302	Mode	Products	bits/spin	bits/64 s	Compressed		
2303					/64 s(TBC)	/spin	/s
2305	Low	P0L-P3L, SP	357	5712	5712		
2306		M1L-M3L	192	3072	300 (L10)		
2307		TSTL	2048	32768	3300 (LL-10)		
2308		<b>DataOut</b>			<b>9312</b>	<b>582</b>	<b>145</b>
2309	Med A	P0-P3, SP	645	10320	10320		
2310		P4-P15	60	960	960		
2311		M0, M1	12288	196608	19700 (L10)		
2312		A0	184	2944	290 (L10)		
2313		M2, M3	6144	98304	9800 (L10)		
2314		M4-M15	7135	114160	11400 (L10)		
2315		TSTC		131072	13100 (LL-10)		
2316		TSTE		131072	13100 (LL-10)		
2317		TLEF		65536	6500 (LL-10)		
2318		<b>DataOut</b>			<b>85190</b>	<b>5324</b>	<b>1331</b>
2319	Med C	P0-P3, SP	645	10320	10320		
2320		P4-P15	60	960	960		
2321		M0, M1	17664	282624	28300 (L10)		
2322		M2, M3	8832	141312	14100 (L10)		
2323		M4-M15	8832	141312	14100 (L10)		
2324		TSTC		131072	13100 (LL-10)		
2325		TSTE		131072	13100 (LL-10)		
2326		TLEF		65536	6500 (LL-10)		
2327		<b>DataOut</b>			<b>100480</b>	<b>6280</b>	<b>1570</b>
2328		Med D	P0-P3, SP	645	10320	10320	
2329	P4-P15		60	960	960		
2330	M0, M1		18432	294912	29500 (L10)		
2331	A0		736	11776	1200 (L10)		
2332	M2, M3		6144	98304	9800 (L10)		
2333	M4-M15		7135	114160	11400 (L10)		
2334	TSTC			131072	13100 (LL-10)		
2335	TSTE			131072	13100 (LL-10)		
2336	TLEF			65536	6500 (LL-10)		
2337	<b>DataOut</b>				<b>96280</b>	<b>6017</b>	<b>1504</b>
2338	Med E	P0-P3, SP	645	10320	10320		
2339		P4-P15	60	960	960		
2340		M0, M1	14592	233472	23500 (L10)		
2341		M2, M3	6144	98304	9800 (L10)		
2342		TLEF		69905	3500 (L20)		
2343	Events	2618	41900	41900			
2344	<b>DataOut</b>			<b>86480</b>	<b>5405</b>	<b>1351</b>	

**Table 18** (Continued)

Mode	Products	bits/spin	bits/64 s	Compressed		
				/64 s(TBC)	/spin	/s
High B	P0-P3, SP	645	10320	10320		
	P4-P15	60	960	960		
	M0, M1	29184	466944	46700 (L10)		
	M2, M3	18432	294912	29500 (L10)		
	M4-M15		442370	44200 (L10)		
	TSTC		1048576	52500 (L20)		
	TSTE		1048576	52500 (L20)		
	TLEF		1048576	52500 (L20)		
	Events	26187	419000	419000		
	<b>DataOut</b>			<b>708180</b>	<b>44261</b>	<b>11065</b>

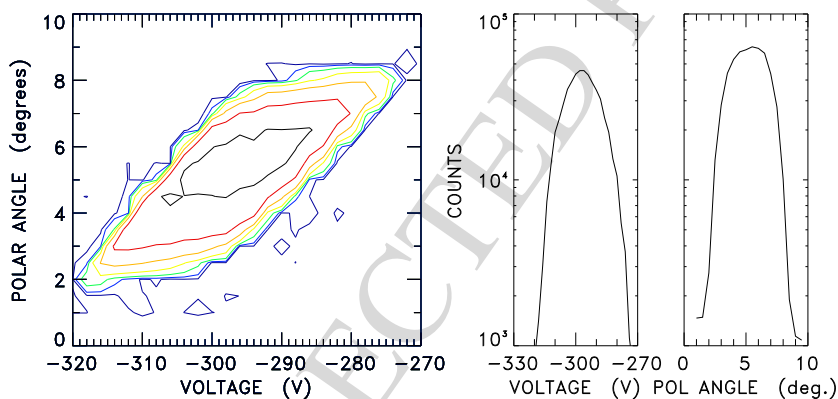
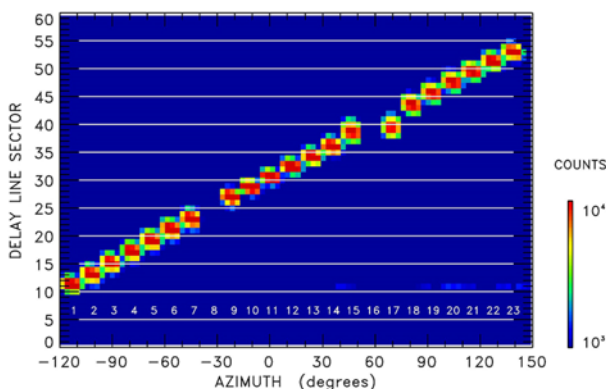


**Fig. 49** Count rate contours as functions of the polar angle (elevation) and voltage (energy) for MSA entrance window No. 11 using a 2 keV N<sup>+</sup> beam (left). Integrated counts versus voltage and integrated counts versus elevation (right) (after Delcourt et al. 2016)

fication voltages; the maximum operation voltages are  $\pm 12$  kV. Notably a grid, effectively acting as an electrostatic lens polarized at 1 kV located near the exit of the energy analyzer prevents the large accelerating electric field from penetrating deep into this analyzer and has a detrimental effect on ion trajectories. Upon entry to the TOF chamber, ions interact with thin ( $\sim 1 \mu\text{g}/\text{cm}^2$ ) carbon foils, which leads to emission of one or several secondary electrons in both forward and backward directions. With the help of an electrode tailored for this purpose, forward electrons are deflected toward the outer part of the LEF MCP (Fig. 39). At the back of this MCP, electrons are collected on a delay line and the START pulse obtained is used to trigger TOF measurement. That is, the START pulse opens a TOF window of  $\sim 1560$  ns during which a STOP pulse is expected; in practice, up to three STOP pulses can be recorded. Moreover, the position of the electron impact on the delay line provides information on the azimuthal sector of the incoming ion. This is illustrated in Fig. 50, where the color map shows data obtained between the 60 delay line sectors and the 21 entrance windows (or azimuth). Similar to that shown in Fig. 48, the modulation of the ion count rate is

**Fig. 50** Color-coded count rate as functions of azimuth and delay line sector for a 2 keV  $N^+$  beam



attributed to the regularly spaced partition walls at the entrance of the instrument. Measurements of the START rate in the different delay line sectors yield the 3D angular and energy distributions of the ions without mass identification but with high temporal resolution.

To protect MCP from the potentially intense solar wind flux, a “spoiler” capability has been included in the design of the energy analyzer. As previously mentioned, the external electrode of this analyzer has been designed in three mechanical parts, with the capability to polarize the central one independently from the other two for de-focusing or spoiling the incoming ion beam. When the ion count rate over one spin exceeds  $10^3$  START events in one energy bin and one entrance window, the voltage on the central electrode is increased by one step at the end of the spin. Conversely, when the count rate drops below  $5 \times 10^2$  START events, the spoiler voltage is decreased by one step. At the first switch-on of the spoiler, the voltage value used is that corresponding to 10% efficiency (56% of the inner electrode voltage) to effectively protect the MCP. Subsequently, the spoiler voltage is further increased (decreased) if the count rate is excessively high (low).

After crossing the carbon foils, the ions travel inside the TOF chamber and impact either the LEF MCP or ST MCP depending on their charge state; hence, a STOP pulse can be associated with the corresponding START to derive the particle TOF and its  $m/q$  ratio. As previously mentioned, LEF data are characterized by low count rates owing to the small fraction of ions that remain positively charged after crossing the carbon foils but a high mass resolution, which is of primary interest for planetology science. In contrast, ST data are characterized by high count rates (owing to the large fraction of ions neutralized during carbon foil crossing) but lower mass resolution, although this mass resolution can be improved to some degree by considering a small collection area at the center of the ST MCP. An example of the TOF data obtained is provided in Fig. 51. The top panel in the figure shows LEF data for different ion species of  $N^+$ ,  $O^+$ ,  $Na^+$  and  $K^+$ . Notably, the width of the measured spectra is narrow regardless of the ion mass. The bottom panel of the figure shows ST data for conditions similar to those in the top panel. These ST spectra, which resemble those of MESSENGER FIPS, clearly contrast with those of LEF (top panel) with larger count rates and much lower mass resolution. In particular, the spectrum achieved for  $K^+$  ions that spreads over a large TOF interval, owing to large angular diffusion and energy straggling upon crossing the carbon foils, cannot be clearly identified in the long TOF tail. As expected, the center panel of Fig. 51 that shows the TOF spectra obtained on the central ST exhibits a somewhat enhanced mass resolution and lower count rates. Moreover, different ghost peaks appearing in the figure are attributed to secondary emissions inside the TOF

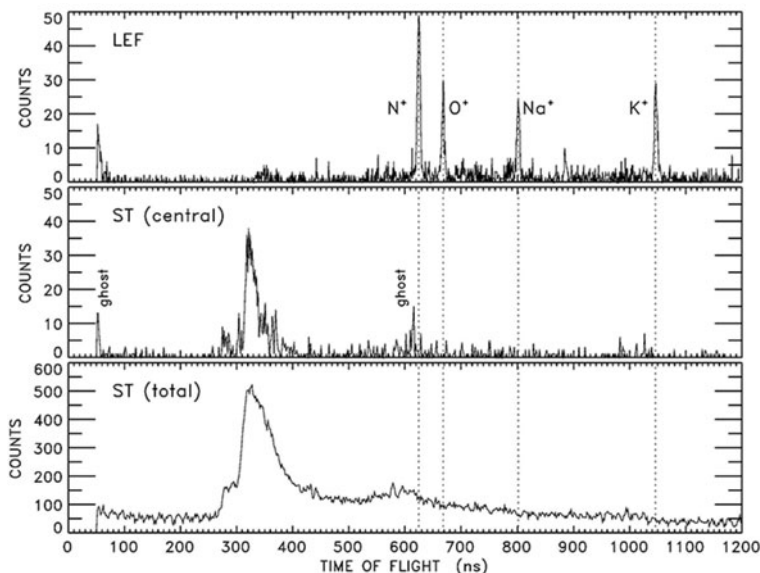


**Fig. 51** TOF spectra for a 5 keV beam of  $N^+$ ,  $O^+$ ,  $Na^+$  and  $K^+$  ions with TOF chamber high voltage set to  $\pm 11$  kV. From top to bottom: LEF, central ST and total ST (after Delcourt et al. 2016)

chamber (Fig. 10 of Delcourt et al. 2016). Generally, these ghost peaks are less pronounced at larger operation voltages.

Tables 19 and 20 provide a more quantitative view of the results obtained from TOF chamber calibration. As an example, Table 19 shows the TOF parameters obtained for two different energies and two different operation voltages for  $He^+$ ,  $Na^+$  and  $K^+$  ions. For a given operation voltage ( $\pm 8$  kV or  $\pm 11$  kV), the isochronous nature of the LEF spectra is clearly apparent with similar  $T_m$  values regardless of the ion energy. In addition, the narrow width of the spectra led to enhanced mass resolution (computed as  $T_m/\Delta T$ ) of at least 100.

In contrast to that in Table 19, the ST results in Table 20 clearly exhibit  $T_m$  values that decrease with increasing energy, regardless of ion species ( $He^+$  or  $K^+$ ) or operation voltage ( $\pm 8$  or  $\pm 11$  kV). Moreover, the TOF spectra width increased significantly for  $K^+$ , exemplifying the poor mass resolution capability of ST for heavy ions.

A global view of the MSA TOF-mass mapping is provided in Fig. 52, which shows the TOF intervals used to identify the ion species depending upon their energy.

### 3.4.4 Near-Earth Commissioning Results of MSA

In contrast to MPO, the Mio spacecraft will spin (4 s) during the orbit phase at Mercury. During the seven-year cruise, Mio is hidden behind the MOSIF thermal shield to avoid harsh solar radiation. As a result, MPPE particle instruments have narrow FOVs pointing along the Mio spin axis; thus, very limited data are expected throughout the cruise phase. In contrast to electrons that are nearly isotropic, the highly collimated solar wind ions cannot be recorded in the cruise phase configuration, because the solar wind direction is obstructed by MOSIF; only dark counts can be obtained. To simulate ions entering the energy analyzer, MSA features a calibration pulse that can be parameterized with different frequencies and delay line sectors. This START-like calibration pulse was used during near-Earth commissioning to check the MSA status and data flow.

2501 **Table 19** Selected parameters of  
 2502 MSA LEF spectra. The mass  
 2503 resolution is derived from  
 2504  $T_m/\Delta T$  where  $T_m$  is the median  
 2505 value and  $\Delta T$  is the TOF spectra  
 2506 FWHM

2507  
 2508

2509

2510

2511

2512

2513

2514

2515

2516

2517

2518

2519

2520

2521

2522

2523

2524

2525

2526 **Table 20** Sam as Table 19 but  
 2527 for central ST and total ST

2528

2529

2530

2531

2532

2533

2534

2535

2536

2537

2538

2539

2540

2541

2542

2543

2544

2545

2546

2547

2548

2549

2550

He <sup>+</sup>					
TOF voltage	Energy	$T_m$ (ns)	$\Delta T$ (ns)	$T_m/\Delta T$	
±8 kV	1–2 keV	398.1	27.1	14.7	
	4–6 keV	394.9	33.4	11.8	
±11 kV	1–2 keV	336.3	5.5	61.4	
	4–6 keV	335.2	27.2	12.3	
Na <sup>+</sup>					
TOF voltage	Energy	$T_m$ (ns)	$\Delta T$ (ns)	$T_m/\Delta T$	
±8 kV	1–2 keV	957.6	5.8	166.0	
	4–6 keV	955.4	4.3	222.4	
±11 kV	1–2 keV	810.7	6.8	118.7	
	4–6 keV	809.7	4.7	172.7	
K <sup>+</sup>					
TOF voltage	Energy	$T_m$ (ns)	$\Delta T$ (ns)	$T_m/\Delta T$	
±8 kV	1–2 keV	1249.4	11.1	112.5	
	4–6 keV	1247.2	11.2	111.1	
±11 kV	1–2 keV	1057.5	7.2	146.5	
	4–6 keV	1055.5	9.3	113.3	
He <sup>+</sup>					
TOF voltage	ST	Energy	$T_m$ (ns)	$\Delta T$ (ns)	$T_m/\Delta T$
±8 kV	central	4 keV	193.7	8.6	22.4
		10 keV	154.9	7.8	19.8
±11 kV	total	4 keV	195.5	14.1	13.9
		10 keV	158.2	12.8	12.3
±8 kV	central	4 keV	171.3	7.6	22.5
		10 keV	142.5	7.4	19.4
±11 kV	total	4 keV	173.2	12.4	14.0
		10 keV	144.6	9.6	15.0
K <sup>+</sup>					
TOF voltage	ST	Energy	$T_m$ (ns)	$\Delta T$ (ns)	$T_m/\Delta T$
±8 kV	central	4 keV	662.5	322.7	2.1
		10 keV	581.3	342.2	1.7
±11 kV	total	4 keV	681.8	261.4	2.4
		10 keV	609.5	268.2	2.3
±8 kV	central	4 keV	620.4	173.0	3.6
		10 keV	525.0	116.1	4.5
±11 kV	total	4 keV	644.7	236.7	2.7
		10 keV	556.5	251.1	2.2

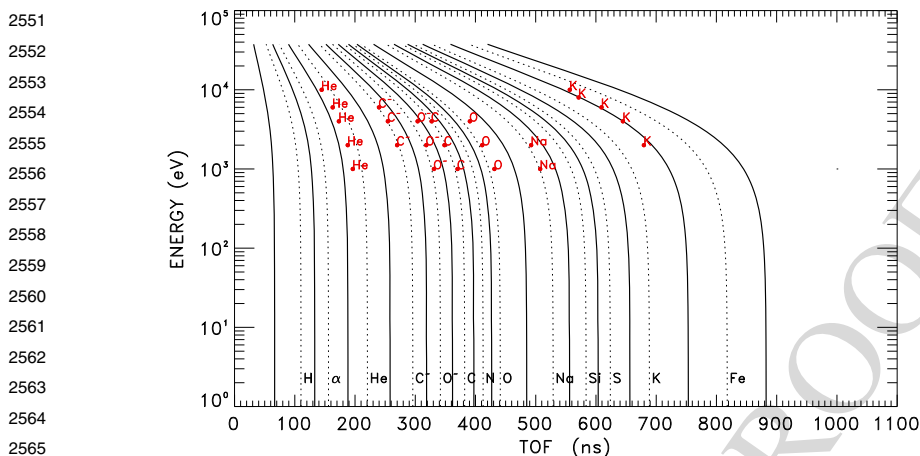


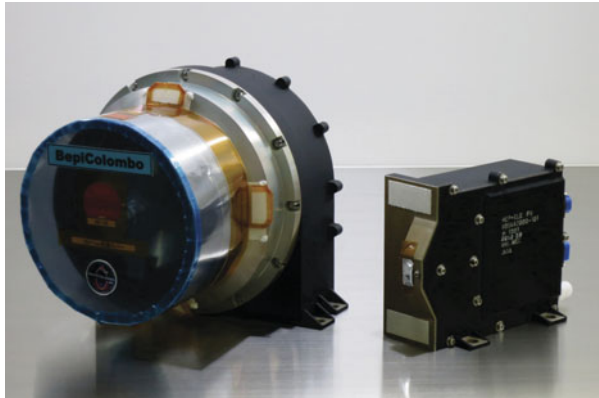
**Fig. 52** TOF variation versus energy for different ion species (dotted lines) as obtained from equation (3) of Delcourt et al. (2016) with  $L = 16$  cm. The solid lines depict the TOF intervals attributed to each species and the red dots show the results of MSA FM calibration. The TOF chamber voltage is set to 11 kV

Similar to that for other MPPE instruments, near-Earth commissioning of MSA has been organized in two sequences, with the first in November 2018 to check basic functionalities, and the second in June 2019 to check high voltages. Owing to the transmission of data via the MPO spacecraft during the cruise, only the L-mode telemetry regime is available. A problem was encountered during the first MSA commissioning sequence that appeared nominal until a calibration pulse triggered was not followed by L-mode data reception. Debriefing was performed and possible causes including hardware failure were explored according to fault tree analysis scheme. The second MSA commissioning sequence provided new information on this problem because the L-mode data acquisition was successful in June 2019 but was contingent upon rebooting of MDP1, the MPPE dedicated DPU, before operating MSA. Although this rules out a hardware failure, the reason for this faulty behavior is not yet understood and still is under investigation.

Throughout the commissioning and operations, voltages are monitored through MSA dedicated CPUs via comparison of HK values with the command values. If both values are not consistent (with 15% margin) after one spin, an error message is produced in the corresponding Mission Data packet, if such an error message is obtained during four consecutive spins, an emergency MSA shutdown is issued. HV monitoring is initiated via upload of the On-board Command Language (OCL) procedure from EEPROM. When this HV monitoring is correctly enabled, the HK return value is “ON”. Prior to HV setup, nine commands are sent to enable measurements and to set thresholds for START and STOP signals. The HV setup procedure is then conducted according to six different procedures corresponding to  $\pm 8$  kV,  $\pm 10$  kV and  $\pm 11$  kV in normal or safe modes with execution times varying among the procedures. As a general rule, safe mode is used during preliminary MSA operations. In chronological order, MSA HVs are set on LEF MCPs, ST MCPs, TOF chamber, and floating MCP. The TOF chamber and floating MCP voltages are then adjusted before triggering the energy analyzer sweep. During the second MSA commissioning sequence in June 2019, the following results were obtained.

- Nominal voltage (1500 V) on the LEF MCP stack
- Nominal voltage (2250 V) on the ST MCP stack

2601 **Fig. 53** HEP-ele and HEP-ion  
2602 with some non-flight items (blue)  
2603 in a clean bench  
2604



2605  
2606  
2607  
2608  
2609  
2610  
2611  
2612  
2613  
2614

- 2615 – Nominal voltage (450 V) on the floating MCP
- 2616 – Half-initial operation voltage ( $\pm 4$  kV) in the TOF chamber
- 2617 – Fixed voltage (500 V) in the energy analyzer
- 2618

2619 To finalize the MSA HV tests, delta commissioning was scheduled in August 2019, but  
2620 was postponed until early 2020. Delta HV commissioning of MSA was performed at ESOC  
2621 on February 4 and 5, 2020. All nominal voltages were successfully applied, including TOF  
2622 chamber VHV ( $\pm 8$  kV), which will be used in the first phase of MSA operations. The energy  
2623 analyzer sweep was also successfully triggered, making MSA ready for operations, although  
2624 L-mode data transmission issue still is under investigation.

2625

### 2626 **3.5 HEP-ele and HEP-ion**

2627

#### 2628 **3.5.1 Instrument Description of HEP**

2629

2630 The high-energy particle instruments for electrons and ions onboard Mio consist of two  
2631 sensor heads, HEP-electron (HEP-ele) and HEP-ion. Figure 53 shows photographs of these  
2632 instruments in a clean bench in the calibration facility at Nagoya University. Non-flight  
2633 items (blue) protected the flight models during transportation before the final calibrations  
2634 in April-May, 2014, as will be discussed in Sect. 3.5.3. The specifications of HEP-ele and  
2635 HEP-ion are summarized in Tables 21 and 22, respectively.

2636 Both instruments are based on the new high-energy particle detection technology devel-  
2637 oped in Japanese research communities, for the X-ray astrophysics and space physics groups  
2638 for space missions. The newest space exploration satellite in Japan, the ERG satellite, is also  
2639 carrying a similar type of high-energy particle detection system using a single-sided strip  
2640 silicon solid-state detector (SSSD) and an ASIC (VA32TA, IDEAS, Norway: Mitani et al.  
2641 2018) as well as the Japanese X-ray Astrophysics mission, Astro-H (Hitomi) (Watanabe  
2642 et al. 2014). In the HEP instruments onboard Mio, the strip system is not used for position  
2643 detection, rather, it is used for noise reduction of SSDs owing to the small capacitance and  
2644 dark current in each strip. In the case of the flight-model HEP-ele onboard Mio, similar to  
2645 HEP onboard ERG, the SSSD-ASIC system is applied to obtain angular directions of inci-  
2646 dent electrons used together with a pinlit type aperture. The SSSD-ASIC system reduces  
2647 the noise level (dark currents) by separating into 158 strip-shaped areas with small capaci-  
2648 tance connected and controlled by 5 ASICs. Figure 54 depicts two sections of HEP-ele, in  
2649 which two separate assemblies of this combination of an SSSD and five ASICs cover up-

2650

**Table 21** Summary of HEP-ele performance

2651	Field of view	$(18^\circ \times 57^\circ) \times 2$
2652	Angular resolution	$18^\circ \times 12^\circ$
2653	Energy range	30–700 keV
2654	Energy resolution	20 keV ( $\leq 20^\circ\text{C}$ )
2655		$\Delta E/E = 50\%$
2656	Time resolution	4 s (1spin) (normal mode)
2657		100 ms (burst mode)
2658	Geometrical factor	$0.036 \text{ cm}^2 \text{ sr}$
2659	Mass	0.27 kg
2660	Power	3.04 W
2661	Dimensions	$82 \text{ mm} \times 134 \text{ mm} \times 115 \text{ mm}$
2662	Data rate	0.0064 kbits/s (L-mode)
2663		1.3 kbits/s (M-mode)
2664		5.1 kbits/s (H-mode)

**Table 22** Summary of HEP-ion performance

2669	Field of view	$11^\circ \times 110^\circ$
2670	Angular resolution	$11^\circ \times 20^\circ$
2671	Energy range	30–1500 keV
2672	Energy resolution	20 keV ( $\leq 20^\circ\text{C}$ )
2673		$\Delta E/E = 50\%$
2674	Time resolution	4 s (1spin) (normal mode)
2675		100 ms (burst mode)
2676	Geometrical factor	$0.36 \text{ cm}^2 \text{ sr}$
2677	Mass	1.71 kg
2678	Power	4.81 W
2679	Dimensions	$212 \text{ mm} \times 169.2 \text{ mm} \times 180 \text{ mm}$
2680	Data rate	0.0085 kbits/s (energy), 0.0064 kbits/s (TOF) (L-mode)
2681		0.77 kbits/s (energy), 0.19 kbits/s (TOF) (M-mode)

and down-looking FOVs from the spacecraft spin plane, respectively. Each SSSD-ASIC assembly has a rectangular SSSD forming a one-layered stack with 158 strips and 5 ASICs to cover  $18^\circ \times 57^\circ$  in total, and an angular resolution of  $18^\circ \times 11^\circ$  is achieved by binning these 158 strips into 5 directions according to their ASIC connections. The accumulated pulse height levels corresponding to the deposited energies in the neighboring three strips are used to calculate the incident particle energy. These slow-shaped pulse height signals from the 10 total ASICs are processed in an analogue-digital converter (ADC) board and an FPGA in the HEP-ele sensor head electronics. Another FPGA is designated for the space-wire interface to the mission data processor (MDP). The analogue-digital conversion of the pulse height for the neighboring three strips is conducted sequentially by the ADC, and their accumulation for the total energy analysis is performed in the FPGA. The incidence direction for each particle detection is also identified and tagged in the FPGA using the ASIC fast-shaped signals. Figure 55 shows the SSSD-ASIC assemblies for HEP-ele in which 158 strips on the SSSDs and 5 ASICs are connected by wire bonding. To avoid contamination by heavier space particles with energies less than several hundreds of kilo electronvolts for

2701  
2702  
2703  
2704  
2705  
2706  
2707  
2708  
2709  
2710  
2711

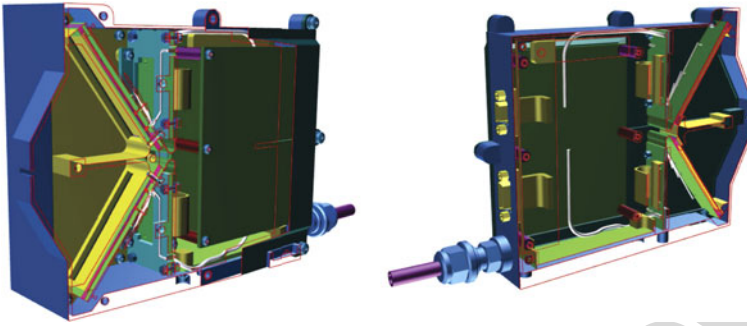


**Fig. 54** Cross sections with slightly oblique cutaway of 3D drawing of HEP-ele from two directions

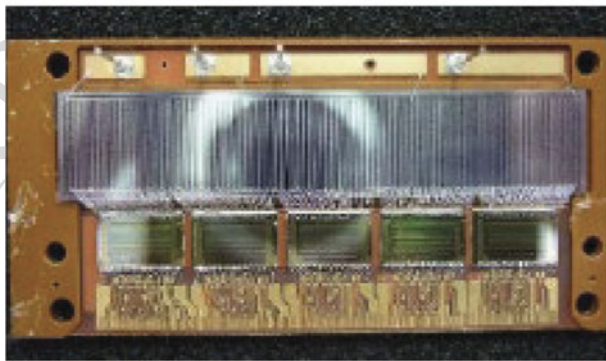
2712  
2713

**Fig. 55** SSSD-ASIC assembly of HEP-ele

2714  
2715  
2716  
2717  
2718  
2719  
2720  
2721  
2722  
2723  
2724  
2725  
2726  
2727  
2728  
2729



2730  
2731  
2732  
2733  
2734  
2735  
2736  
2737  
2738  
2739  
2740



ASIC#4

ASIC#0

2741  
2742  
2743  
2744  
2745  
2746  
2747  
2748  
2749  
2750

protons and stray solar photons, the incident areas of SSSD are coated by Al with an appropriate thickness of 100  $\mu\text{m}$ . The inner walls of the detector section are blackened with conductive paint for decreasing the reflected stray photons (Fig. 56). This black carbon painting was developed by Nishiura Paint Industry in Japan (<https://www.nishiura-p.com>) and was also applied to the plasma particle instruments in the previous Japanese space exploration missions, e.g., PSA-ESA on Nozomi (Planet-B) (Machida et al. 1998) and MAP-PACE on

**Fig. 56** HEP-ele detector section structures blackened with conductive paint

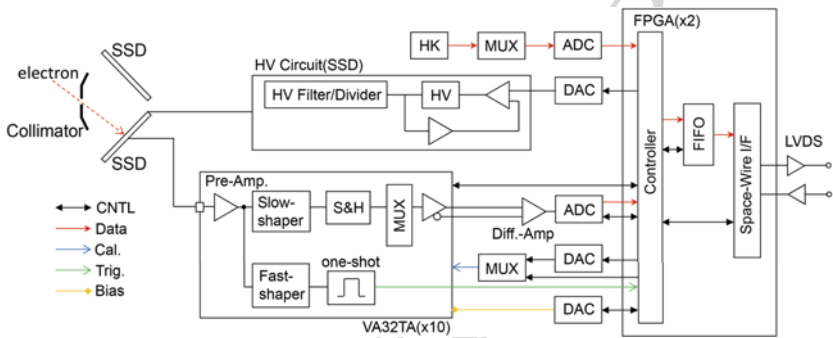
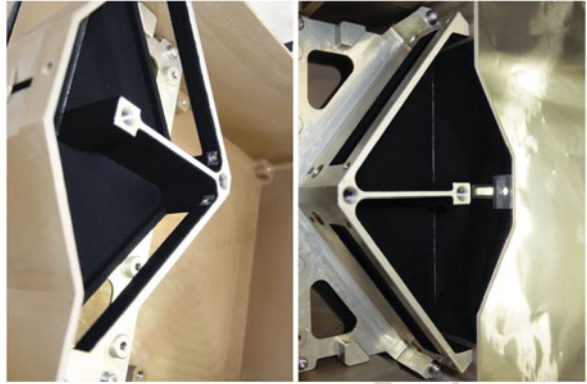
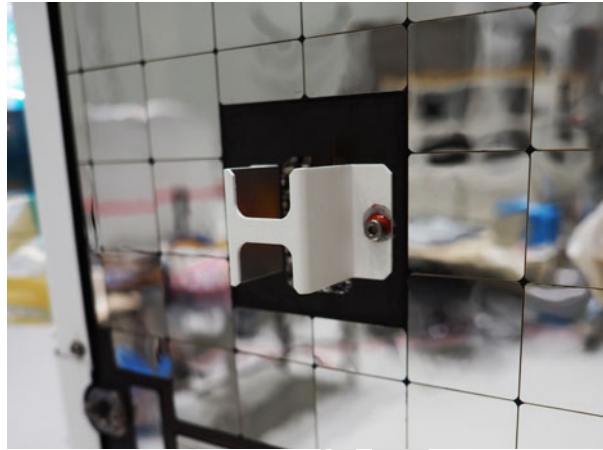


**Fig. 57** Block diagram of HEP-ele

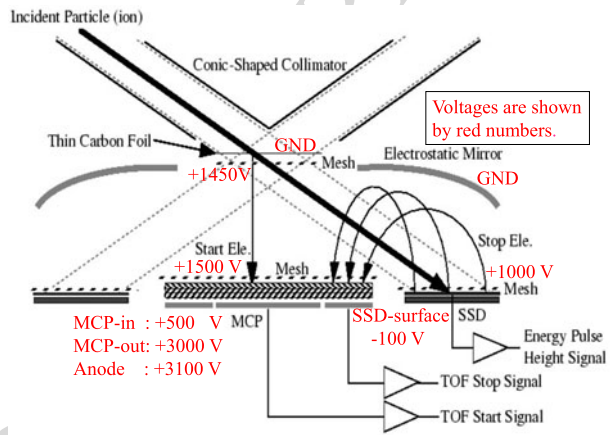
Kaguya (SELENE) (Saito et al. 2010b). The entire sensor head of HEP-ele contains high-voltage supply and front-end processing boards behind the detector section that consists of the pinslit aperture and two SSSD-ASIC assemblies. These components and data/signals are controlled/processed by two FPGAs, as schematically illustrated in the block diagram in Fig. 57. The on-board calibration signals and the bias voltages for the pulse discrimination in each ASIC are also issued via DACs from the FPGA. For preventing the intense solar irradiation near the Mercury orbit from entering the detector section through the pinslit aperture, a rectangular thermal shield is equipped in the Mio spin plane in the overall FOV of HEP-ele at the outside of the aperture (Fig. 58). Therefore, the angular area of  $\pm 4^\circ$  from the spin plane is blocked from the effective HEP-ele FOV by two SSSD-ASIC assemblies as a dead angle range.

The HEP-ion sensor has two measurement capabilities for energy and TOF analyses for the incident ions. These measurement principles, as schematically given in Fig. 59, are essentially the same as those introduced by Saito et al. (2010a). Some structures and performances have been simplified and omitted according to the weight reduction requirement from the viewpoint of the overall spacecraft mission management. The energy/TOF measurement section of the flight-model HEP-ion has five types of components: a conic-shaped collimator, an ultra-thin carbon foil with  $0.5 \mu\text{g}/\text{cm}^2$  put on electroformed mesh folder with transmission of 66%, two assemblies consisting of three SSSD-ASIC pairs and electron leading meshes, an electrostatic mirror as one of outer structures of the sensor, an MCP assembly with an electron attracting mesh, a TOF start-signal anode and six TOF stop-signal

2801 **Fig. 58** HEP-ele onboard  
2802 BepiColombo-Mio photographed  
2803 during the final works before  
2804 launch  
2805  
2806  
2807  
2808  
2809  
2810  
2811  
2812  
2813  
2814  
2815  
2816

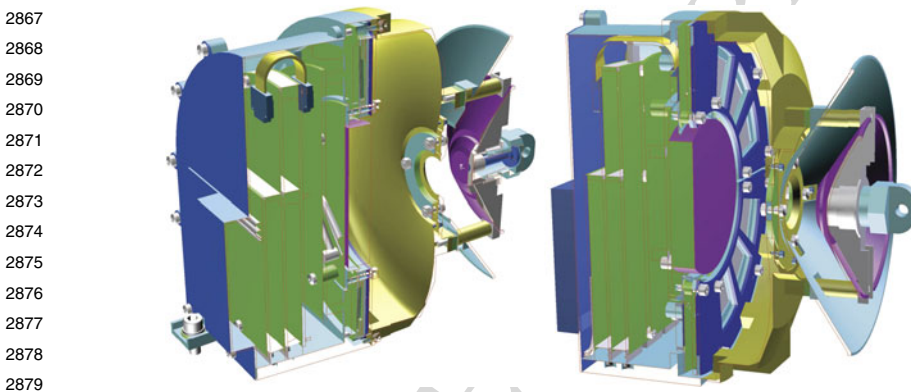
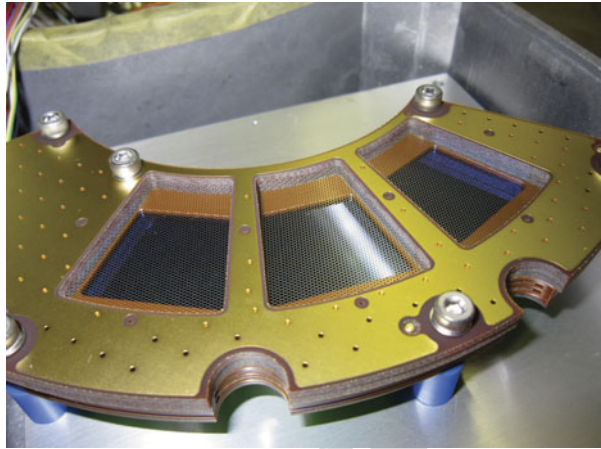


2817 **Fig. 59** Measurement principles  
2818 illustrated on a cross-section of  
2819 HEP-ion  
2820  
2821  
2822  
2823  
2824  
2825  
2826  
2827  
2828  
2829  
2830  
2831  
2832



2833 anodes. The optimal voltages in the TOF analysis unit are also shown in Fig. 59 by red. The  
2834 SSSD incident surface of the engineering-type model is presented in Fig. 60, in which the  
2835 electron leading meshes are not set up. As illustrated in Fig. 61, the number of the HEP-ion  
2836 FOV directions is six, each of which corresponds to one of six SSSD-ASIC pairs for the  
2837 energy analysis measurement mode or TOF stop-signal anodes of the MCP assembly for the  
2838 TOF analysis measurement mode. Similar to the data processing in the HEP-ele sensor  
2839 head, the energy/TOF analysis results are sorted into eight steps. Different from the collimator  
2840 of HEP-ele, the collimator system of HEP-ion is more complicated because the total  
2841 FOV configuration of HEP-ion is nearly half of a conical shape rather than a planar type.  
2842 The closure of the inner conical part of the collimator is designed to protect the ultra-thin  
2843 carbon foil with a 2-cm diameter from the acoustic vibrations/shocks during the spacecraft  
2844 launch operation. A biphenyl block sublimable in vacuum is loaded in the cylinder to keep  
2845 the inner conical collimator closed before the launch operation. Several days after the space-  
2846 craft launch, the biphenyl block is sublimated in space to release the inner conical collimator  
2847 to the measurement position by the extension of a mechanical spring(not shown in Fig. 61).  
2848 The collimator and the measurement section of HEP-ion are also blackened with the same  
2849 black paint as that used for HEP-ele (Fig. 62). Because the aperture size of the conical colli-  
2850

2851 **Fig. 60** Proto-type SSSD-ASIC  
2852 assembly for HEP-ion, which is  
2853 similar to that of the flight model



2867  
2868  
2869  
2870  
2871  
2872  
2873  
2874  
2875  
2876  
2877  
2878  
2879  
2880 **Fig. 61** Cross sections with slightly oblique cutaway of 3D drawings of HEP-ion from two directions

2881  
2882  
2883 mator of HEP-ion is much larger than that of HEP-ele, as shown in Figs. 54 and 61, the large  
2884 thermal shield for HEP-ion is installed on Mio (Fig. 63). The dead angle range is  $\pm 12.5^\circ$   
2885 with respect to the spin plane because a side stay blocks the center of the effective HEP-ion  
2886 FOV between two SSSD-ASIC assemblies. Figure 64 illustrates a block diagram of HEP-  
2887 ion, in which the TOF analysis circuit is added to the HEP-ele diagram. It should also be  
2888 noted that the numbers of the high-voltage supply units (three for HEP-i, one for HEP-e)  
2889 and the ASICs (six for HEP-i, ten for HEP-e) are different from those of HEP-ele.

### 2891 3.5.2 Operation Modes and Data Products of HEP-ele and HEP-ion

2892  
2893 Because of the severe restriction of the telemetry data allocation to HEP-ele and HEP-ion  
2894 observations, the energy/TOF analysis data need to be compressed by using accumulation  
2895 over several FOV directions and observational intervals. The measurements themselves are  
2896 quite simple compared with those of other instruments of MPPE such as MPPE-MSA. As  
2897 described in Sect. 3.5.1, HEP-ele originally had 10 FOV directions in the spinning spacecraft  
2898 frame, corresponding to the polar angles in the direction perpendicular to the spin plane, and  
2899 eight energy steps. However, the spin motion is divided into 16 sectors, which indicates that

2900

2901  
2902  
2903  
2904  
2905  
2906  
2907  
2908  
2909  
2910  
2911  
2912  
2913  
2914  
2915  
2916

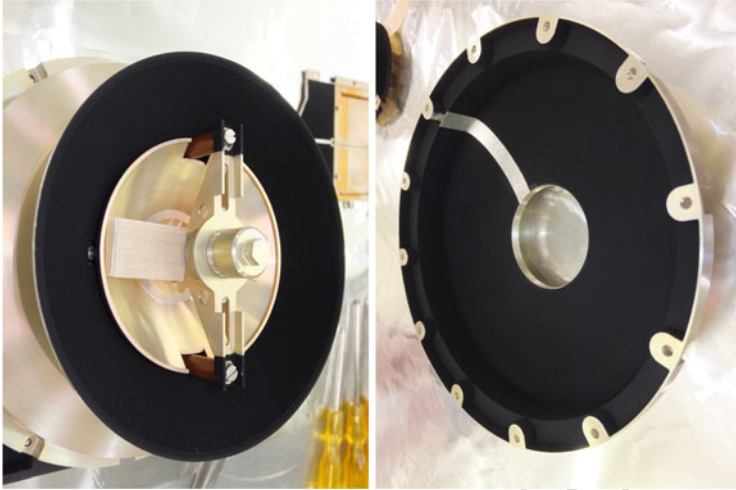
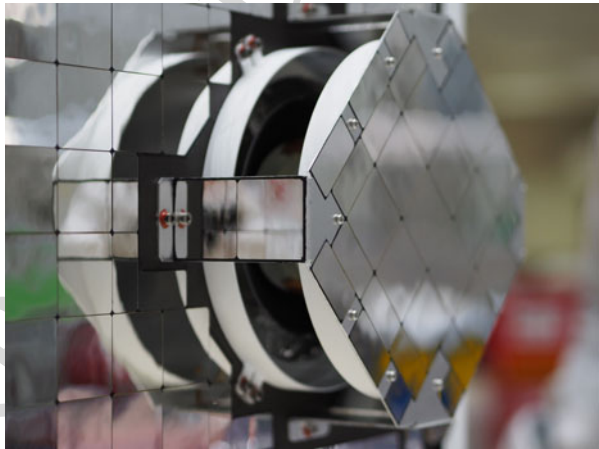


**Fig. 62** HEP-ion collimator (left) and electrostatic mirror (right) of the TOF unit blackened with conductive paint

2917  
2918  
2919  
2920  
2921

**Fig. 63** HEP-ion onboard BepiColombo-Mio photographed during the final works before launch



2922  
2923  
2924  
2925  
2926  
2927  
2928  
2929  
2930  
2931  
2932  
2933  
2934  
2935  
2936  
2937  
2938  
2939  
2940  
2941  
2942  
2943  
2944  
2945  
2946  
2947  
2948  
2949  
2950

the raw count data in  $10$  (polar angle)  $\times$   $8$  (energy)  $\times$   $16$  (sector) bins are produced with every spin motion. Whereas HEP-ion has a similar raw count data structure, the number of FOVs is six. The measurement modes of HEP-ion could be switched between the energy and TOF analyses by changing the high voltages applied in the measurement section. These count data could be compressed in MDP1 according to three spacecraft operation modes, e.g., L- and M-modes. The H-mode of HEP-i is not allocated in the current observational plan for reducing the total HEP data because the HEP-e observations and their data with the high data rates are considered to be more important. Tables 23 and 24 show the data modes for HEP-ele and HEP-ion, respectively, in which the values in round brackets indicate the angle resolutions for the polar (FOV) and sector directions. The energy channels for HEP-ele and HEP-ion and the TOF channels of HEP-ion depend on the energy/TOF binning tables selectable by operation commands.

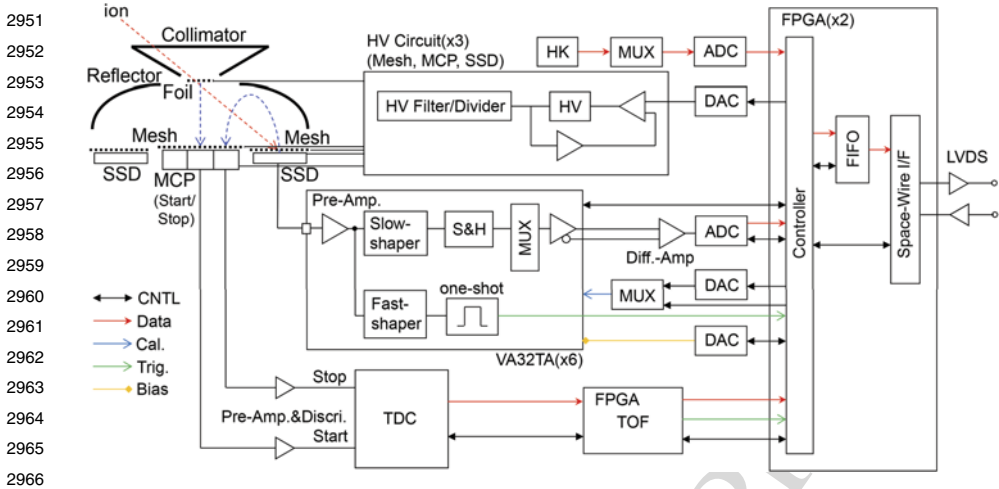


Fig. 64 Block diagram of HEP-ion

Table 23 Observation Mode of HEP-ele

L-mode	Polar FOV(57°):2 × Sector(90°):4 × Energy Step:3	48 bytes/15 spin 48 bytes/15 spin
M-mode	Polar FOV(11°):10 × Sector(45°):8 × Energy Step:4	640 bytes/1 spin 640 bytes/1 spin
H-mode	Polar FOV(11°):10 × Sector(22.5°):16 × Energy Step(95 keV):8	5120 bytes/1 spin 5120 bytes/1 spin

Table 24 Observation Mode of HEP-ion

Energy analysis mode		
L-mode	Polar FOV(60°):2 × Sector(90°):4 × Energy step(440 keV):4	64 bytes/15 spin 64 bytes/15 spin
M-mode	Polar FOV(20°):6 × Sector(45°):8 × Energy step(220 keV):8	384 bytes/1 spin 384 bytes/1 spin
TOF analysis mode		
L-mode	Polar FOV(60°):2 × Sector(90°):4 × TOF(300 ns):3 bin	48 bytes/15 spin 48 bytes/15 spin
M-mode	Polar FOV(20°):2 × Sector(45°):4 × TOF(150 ns):6 bin	96 bytes/1 spin 96 bytes/1 spin

### 3.5.3 Pre-flight Calibration of HEP

The standalone SSSD-ASIC systems of HEP-ele and HEP-ion were calibrated with a radioactive source ( $^{137}\text{Cs}$ ) emitting high-energy electrons with energies of more than 600 keV to check the basic performance including the readout capabilities of the ASIC. Figure 65 presents the pulse-height analysis results obtained with 2 of the 158 strips in the SSSD-ASIC assembly for HEP-ele. Two separate peaks are clear near the uppermost channels

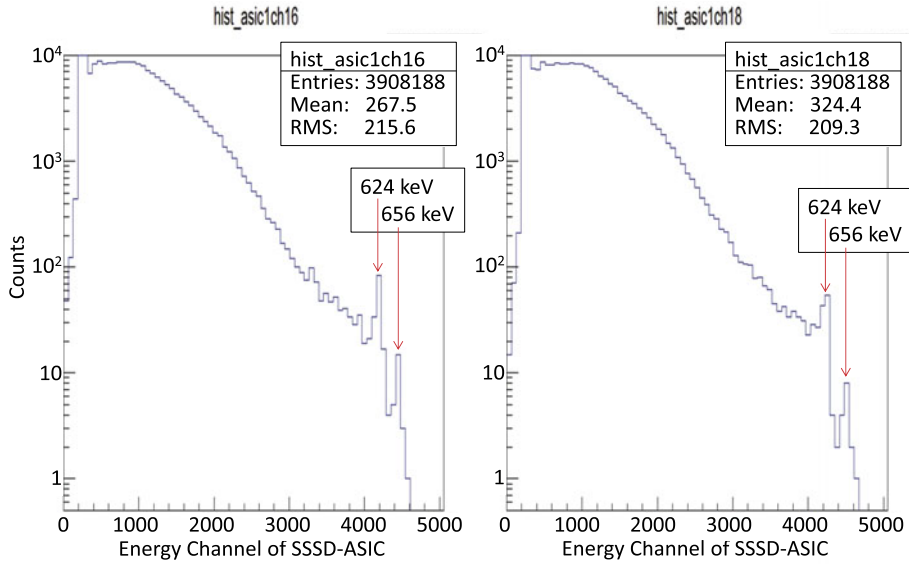
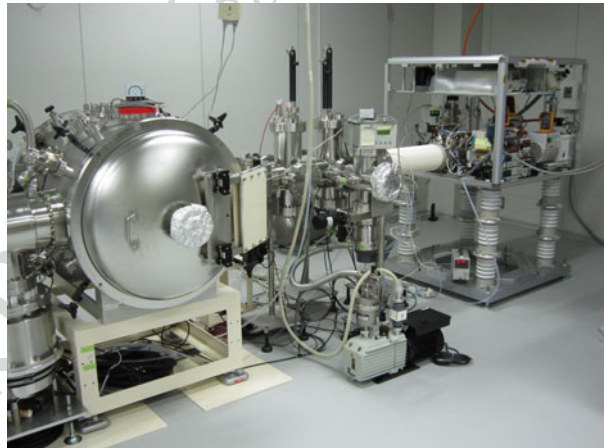


Fig. 65 Examples of pulse height analysis obtained for two strips of the SSSD-ASIC assemblies in HEP-ele

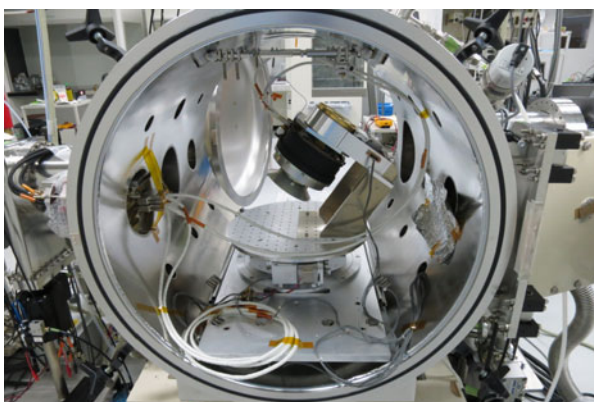
Fig. 66 Calibration facility at the Solar-Terrestrial Environment Laboratory (currently the Institute for Space-Earth Environmental research, ISEE) at Nagoya University



corresponding to electric charges produced in the depletion layer of the SSSD by the incident electrons with 624 keV and 656 keV, respectively. Broad distributions spreading over lower channels are caused by contaminations by a continuum component composed of high-energy photons (X-rays and gamma rays) and scattered electrons in a wide range of energy originating from the radioactive source used for the calibration. This type of readout signal from SSSD by ASIC could be analyzed according to the pulse heights for all  $158 \times 2 = 316$  strips in the 2 SSSD-ASIC assemblies and determines the total energy and incident direction for each of the incident electrons.

The electron/ion beamlines in the calibration facility at Nagoya University (Fig. 66) were also used to check the performance in the lower-energy ranges of the HEP-ele and HEP-ion measurements. The energy ranges used for the HEP instruments were 40–100 keV for elec-

3051 **Fig. 67** HEP-ion set on the  
3052 multi-axial turntable system in  
3053 the vacuum chamber at the  
3054 beamline calibration facility



3055  
3056  
3057  
3058  
3059  
3060  
3061  
3062  
3063  
3064

3065 trons and 60–140 keV for protons, and ions of He and N. To check the instrumental response  
3066 according to the incident angles, we rotated the HEP-ele or HEP-ion instrument around three  
3067 independent axes in the vacuum chamber during the beamline calibrations. Using a multi-  
3068 axial turntable system, the FOV direction was set parallel to or oblique by aimed angle with  
3069 respect to the charged particle beam with diameters of a few tens of millimeters at a given  
3070 energy. Figure 67 shows the HEP-ion instrument with the harness set on the turntable system  
3071 in the vacuum chamber.

3072 The histograms showing the pulse height distributions produced by irradiating electrons  
3073 with the energy of 100 keV are given in Fig. 68, in which six plots are correspondent to  
3074 incident (polar) angles identified by the strip and ASIC numbers of HEP-ele. In each plot,  
3075 two distinct peaks present a so-called pedestal (background noise level) owing to the SSSD-  
3076 ASIC characteristics and an actual signal distribution for the 100-keV electron energy de-  
3077 posits in the depletion layer of the SSSD (e.g., Mitani et al. 2018; Kasahara et al. 2009).  
3078 The channel numbers of the peak distributions in the abscissa are not always identical for  
3079 all six plots because the dark current levels measured in the 10 ASICs could be different.  
3080 These level differences among the 10 ASICs are subtracted after the pulse height analy-  
3081 ses in the HEP-ele FPGA procedures to achieve sufficient energy discrimination capability  
3082 over the entire energy range of HEP-ele. Similar calibrations have been performed for two  
3083 SSSD-ASIC assemblies in HEP-ion by emitting typical types of ion species with several  
3084 levels of energies. Figure 69 shows examples of the pulse height analyses for 140-keV pro-  
3085 tons, in which six panels correspond to six FOV directions, each of which is detected by  
3086 the corresponding ASIC. The lower portions of the energy distributions for the 140-keV  
3087 proton beams overlap with the pedestal distributions at lower channels than the proton dis-  
3088 tributions, which is different from the distributions in Fig. 68. This occurred because the  
3089 energies of ions injected into the solid state detectors with a certain thickness of the dead  
3090 layer can be reduced more significantly than those of electron cases. Similar to the HEP-  
3091 ele energy distributions in Fig. 68, the energy and pedestal peaks are not identical for six  
3092 ASICs of HEP-ion regarding the energy channels in the abscissas. These channel discrepan-  
3093 cies among the ASICs can be reduced by the onboard routine process for channel difference  
3094 subtraction in the FPGA of HEP-ion, which is also similar to the HEP-ele procedures.

3095 The HEP-ion instrument has the capability to measure the velocities of the injected par-  
3096 ticles by using the TOF unit, as described in the previous subsection. We also checked the  
3097 TOF performance with the ion beamlines at Nagoya University and JAXA. Figure 70 sum-  
3098 marizes the TOF experimental results for four different energies (60, 120, 250, 1000 keV)  
3099 and three ion species (proton, singly-charged He and N). Because the heavy ion beams were

3100

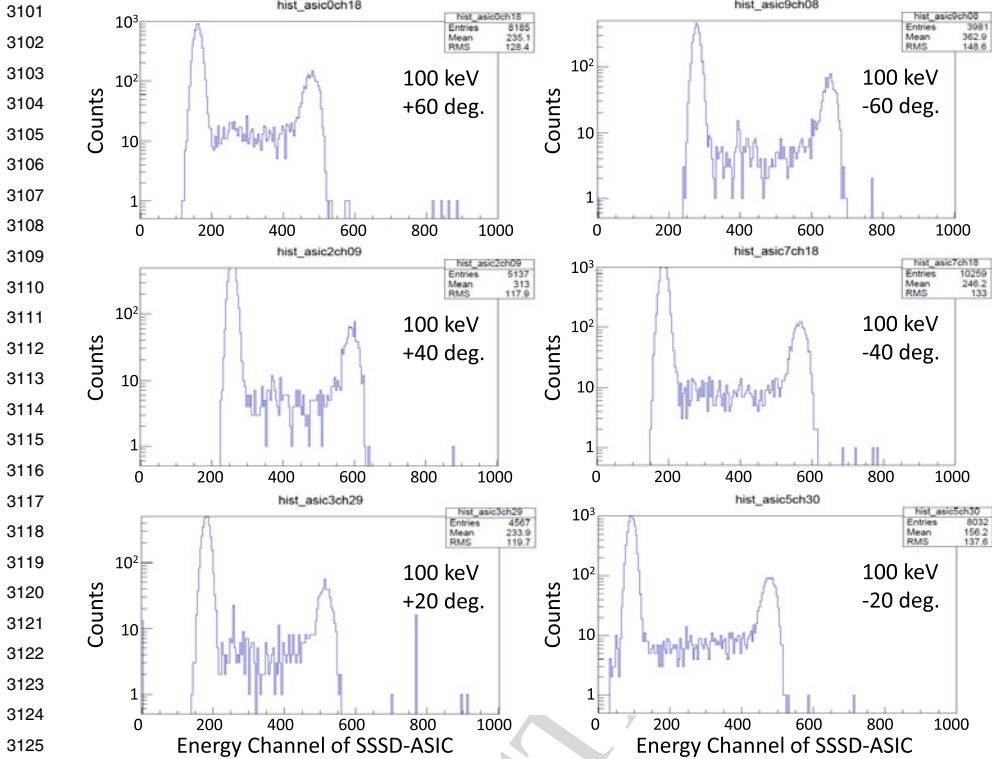


**Fig. 68** Examples of pulse height analysis for six incident (polar) angles obtained in the correspondent strips of two SSSD-ASIC assemblies in HEP-ele

not applicable beyond 150 keV owing to the JAXA high-energy beamline facility performance, the TOF distributions were measured only for H<sup>+</sup>. The incident FOV directions were changed in these measurements so that the maximum peaks were obtained in the different ASIC assemblies as indicated by different colors in the histograms.

### 3.5.4 Near-Earth Commissioning Results of HEP

The first-in-flight operations for HEP-ele and HEP-ion were conducted during the near-Earth commissioning phase of the BepiColombo mission. High-voltage up to 98.2 V was supplied to two SSSD assemblies of HEP-ele. We confirmed the normal HK status including the instrument currents and significantly low dark counts. The six HEP-ion SSSDs were also checked to be activated by the operation with the high-voltage up to 99.7 V, in which the instrument currents and HK status were confirmed to be normal. The activation of the TOF unit of HEP-ion was performed safely to obtain the normal HK status with the high-voltages supplied up to 990 V and 2271 V to the mesh system deriving the start/stop electrons and the MCP assemblies, respectively. The dark counts were measured steadily as constant MCP noise.

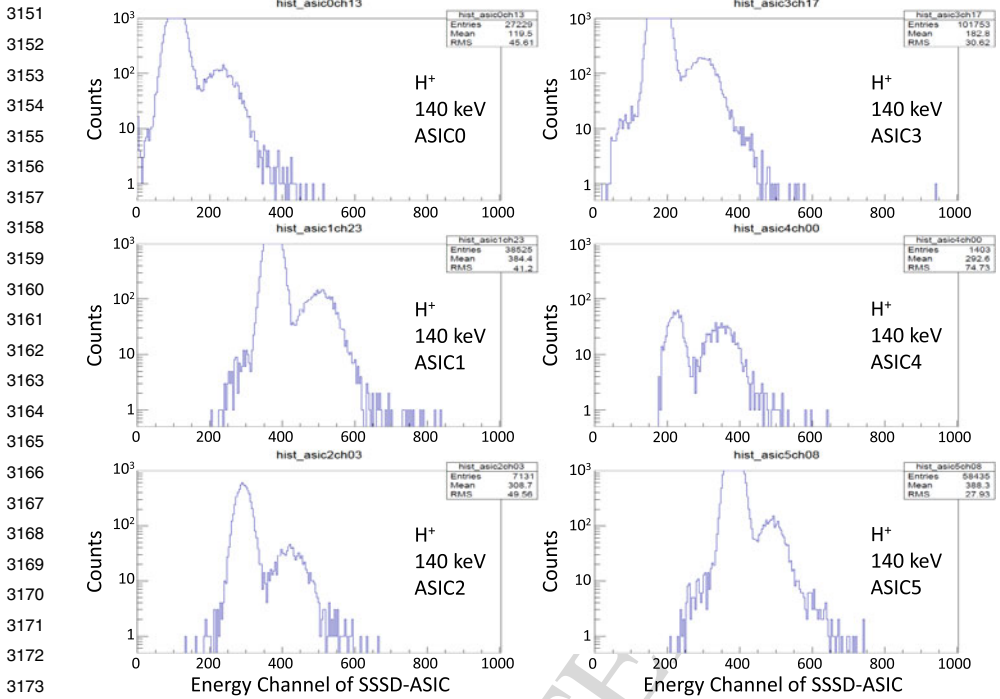


Fig. 69 Examples of pulse height analysis for six incident (polar) angles corresponding to the SSSD-ASIC pairs in HEP-ion

### 3.6 ENA

#### 3.6.1 Instrument Description of ENA

The ENA instrument is based on the surface conversion/reflection technique and consists of four subsystems, including an ion rejection system, ionization surface, photon rejection system that also performs crude energy analysis, and velocity analysis section (Kazama et al. 2009). Figures 71, 72, 73, and 74 show the concept, schematic view, flight model of the instrument, and sun shield mounted on the spacecraft, respectively.

Neutrals enter the sensor through an electrostatic charged particle deflector, which rejects ambient charged particles by a static electric field. The incoming neutrals are then converted to positive ions on an ionization surface and then pass through an electrostatic analyzer of a specific (wave) shape that effectively blocks photons. The electrostatic analyzer also provides crude energy analysis. The “wave” electrostatic analysis design is similar to that used in the MTOF sensor of the CELIAS instrument on the SOHO spacecraft (Hovestadt et al. 1995), which provides a photon rejection factor of  $2 \times 10^{-8}$ . Because the instrument must be capable of measuring masses up to Fe, no foils can be used in the following TOF section. To measure the particle velocity (mass), we used the particle reflection principle developed for and utilized in the Neutral Particle Detector (NPD) of the ASPERA-3 and -4 experiments (Barabash et al. 2006, 2007) for ESA’s Mars and Venus express missions. After exiting the electrostatic analyzer, ions originally neutrals that were converted to ions by the ionization surface are post accelerated up to an energy of 1.5 keV and impact the START

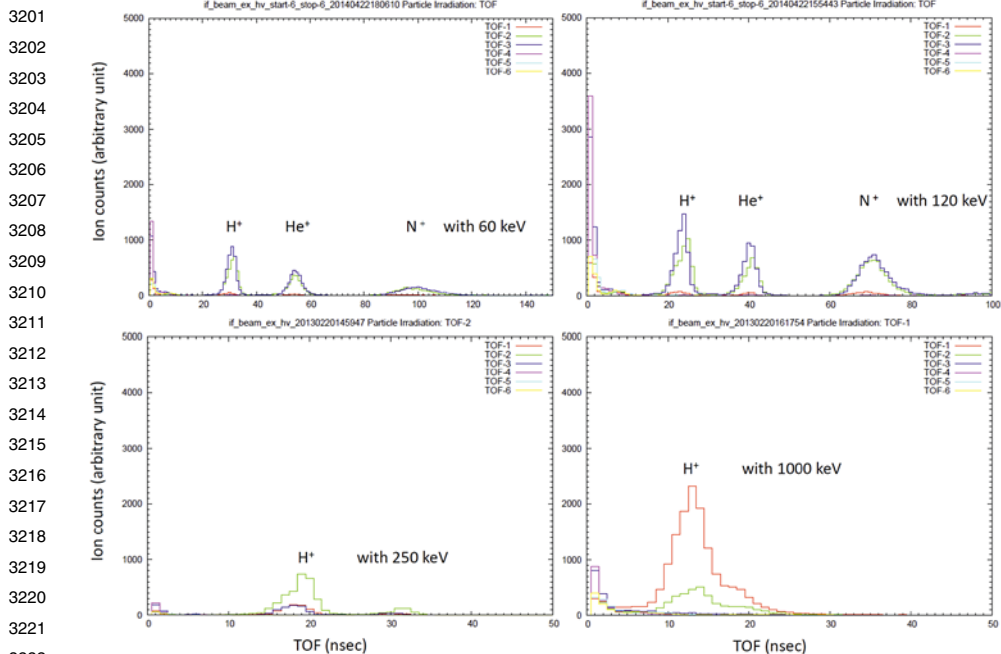


**Fig. 70** TOF profiles for ions with energies of 60, 120, 250, and 1000 keV. Only protons were available for energies beyond 150 keV because of the beamline facility performance

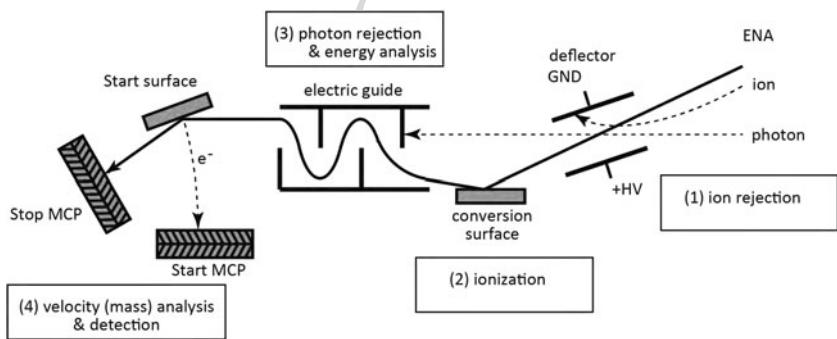


**Fig. 71** ENA measurement concept

surface under a grazing angle of  $15^\circ$ . During the impact, kinetic secondary electrons are emitted and the particles are reflected toward the STOP MCPs, where they are detected and produce a STOP pulse. The secondary electrons from the START surfaces are guided to the START MCPs and produce a START pulse. The START and STOP timing gives the particle velocity. Combining the TOF measurements and electrostatic analyzer settings one determines the LENA energy and mass. Measuring the radius and azimuth of the neutral hit on the START surface by position sensitive START MCPs enables accurate determination of the TOF length and the arrival azimuth of the incoming neutrals. Figure 75 shows the ENA

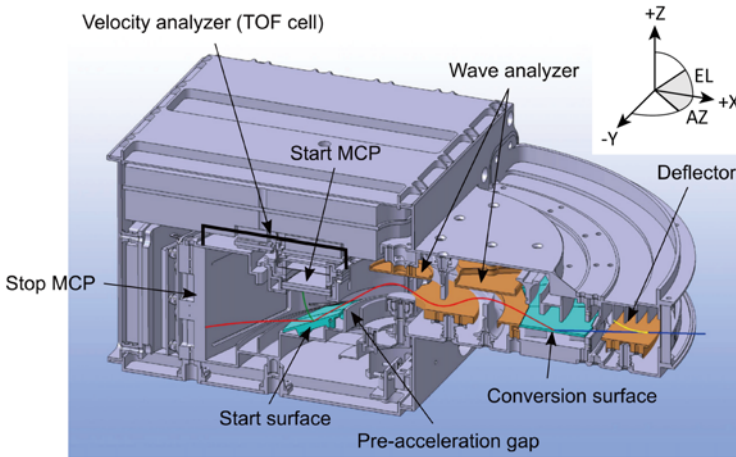


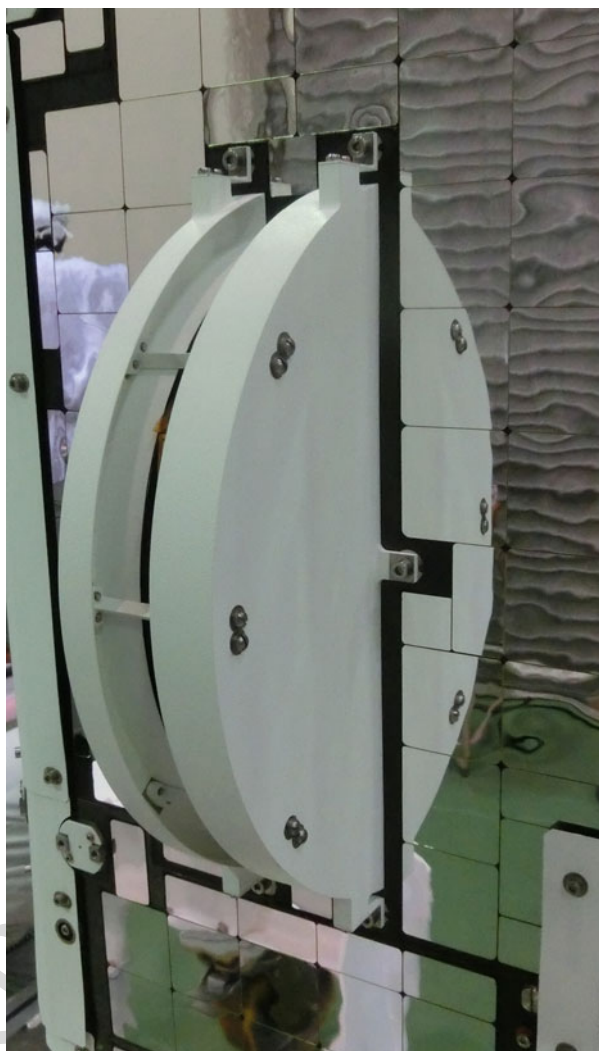
Fig. 72 Sectional view of the ENA sensor

Fig. 73 ENA flight model. The sensor is wrapped by MLI, when ENA is installed in the spacecraft



block-diagram. The instrument electronics include two boards, interface electronics (IFE) and HVPS. The DC/DC converters and digital processing are provided externally. The ENA sensor characteristics are summarized in Table 25.

Fig. 74 ENA sun shield



The ENA sensor comprises six key elements: (1) conversion surface, (2) photon absorbing surfaces, (3) START and STOP MCP assemblies, (4) START surface, (5) IFE, which provides front-end-electronics functions, sensor control, and interface with the MPPE DPU (MDP1), and (6) HVPS.

### (1) Conversion surface

After passing the electrostatic analyzer, LENAs hit a conversion surface under a grazing angle of  $15^\circ$ , where they are converted to positive ions. The surface is  $\text{Al}_2\text{O}_3$  (alumina) deposited on a polished (highly smooth) substrate, such as a silicon wafer. A photograph of the conversion surface is shown in Fig. 76. The temperature of the conversion surface is controlled to stay above  $+50^\circ\text{C}$  throughout the mission to avoid a stack of contaminating materials that would decrease the efficiency of neutral to ion conversion. The conversion surface element has two heater systems. One is operated by the heater control system on-

**Table 25** Summary of ENA performances

Field of view	15° × 160°
Angular resolution	9° × 25° (FWHM)
Energy range	10 eV–3.3 keV
Energy resolution	0.5 (ΔE/E)
Mass resolution	H, O and heavy particles
Geometric factor	10 <sup>-2</sup> cm <sup>2</sup> str eV/eV/sector
Total efficiency	~0.01
Mass	2.13 kg
Power	4.42 W (secondary side)
Dimensions	258 mm × 127 mm × 223 mm (w/o thermal shield)
Data rate	0.5 kBytes/s (nominal) after factor 4 compression

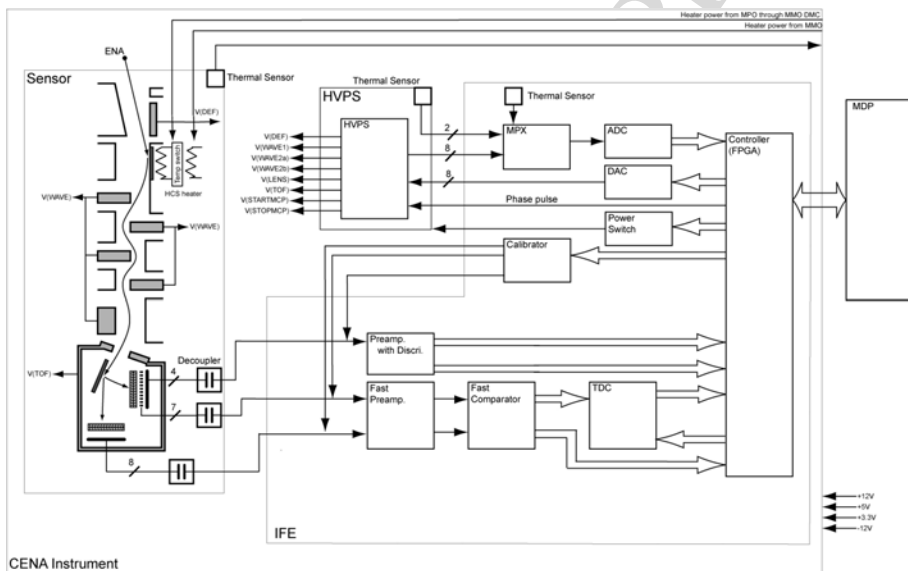


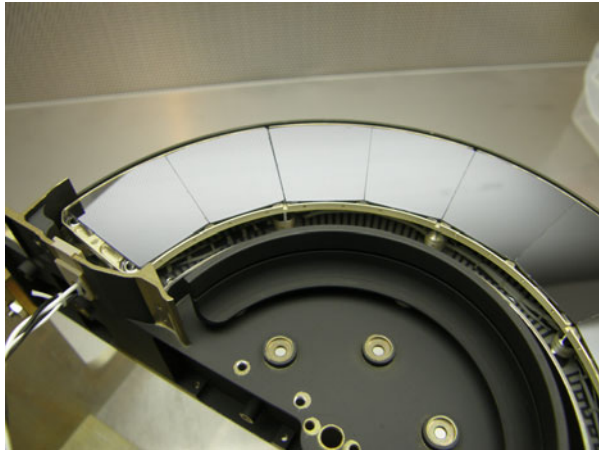
**Fig. 75** ENa block diagram

board MMO. The other is powered by MPO and is controlled by the ENA heater control and temperature monitoring system (ENA HCS) installed in the ENA instrument. This is necessary because MMO is turned off most of the time during the cruising phase to Mercury. The power for ENA HCS is separated from the other ENA electronics.

## (2) Photon absorbing surfaces

The large electrodes in the wave electrostatic analyzer are specially designed coated plates with high photon absorbing surfaces. The grooves on the plates follow the design for the PLASTIC instrument on SOHO (Galvin et al. 2008). The coating is CuS. This structure serves as a very efficient trap for photons. The total UV transmittance of the system before the TOF section is < 10<sup>-9</sup>.

3401 **Fig. 76** Conversion surfaces of  
3402 ENA



3416  
3417 **(3) START and STOP MCP assemblies**

3418 The START MCPs are used for both START timing and the determination of the START  
3419 hit position (radius and azimuth). A chevron of annular MCP plates with an outer diameter  
3420 100 mm is used. The electron cloud exiting the back of the MCP is split between a grid  
3421 and a plate discrete anode. The grid is divided into seven decoupled sectors to give seven  
3422 azimuths and seven START timings. The plate anode is divided into four concentric rings to  
3423 provide determination of the TOF length, where the TOF path length range is from 34 mm  
3424 to 60 mm. For each individual case, uncertainty of about  $\pm 5$  mm is present owing to the  
3425 different orientations of the START surface and the STOP MCP front planes. The STOP  
3426 MCPs are used for STOP timing and determination of the STOP hit position (only azimuth),  
3427 with four identical assemblies used. The anode behind each MCP assembly is divided into  
3428 two parts, giving eight independent outputs. Figure 77 shows the channel definition of the  
3429 MCP anodes.

3430  
3431 **(4) START surface**

3432 The START surface provides effective reflection of the particles (high reflection coefficient,  
3433 narrow scattering angle) and high secondary electron yield. The secondary electron  
3434 yield can be optimized by increasing the post acceleration voltage, and the reflection coefficient  
3435 can be increased by choosing materials for the START surface with high atomic  
3436 numbers. The START surface is mono-crystalline tungsten. Figure 78 shows a photograph  
3437 of the START surface installed in the electrode structure of the TOF section.

3438  
3439 **(5) Interface electronics**

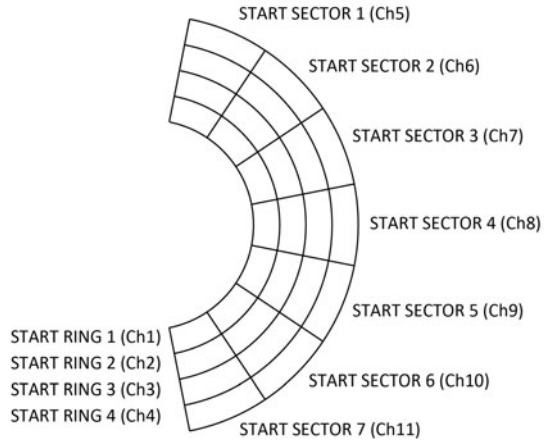
3440 The IFE has the following functions:

- 3441 – Amplification of MCP output signals
- 3442 – Measurement of the time between START and STOP signals
- 3443 – Generation of calibration pulse
- 3444 – HVPS control and monitoring its output levels
- 3445 – Communication with MDPI (reception of commands and transmission of measured  
3446 data)

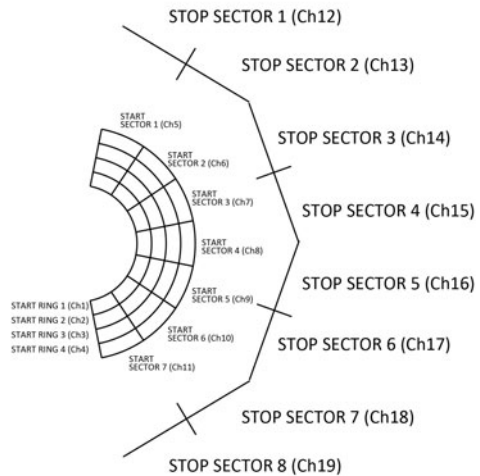
3447 IFE has 19 charge sensitive preamplifiers—shapers including seven fast preamplifiers for  
3448 seven START sectors, eight fast preamplifiers for eight STOP plates and four slow preamplifiers  
3449 for four START rings. One TOF unit accepts START signals from any of the seven  
3450

**Fig. 77** Channel definition of the MCP anodes of ENA. The lower panel showing the channel definition of the STOP MCP anodes includes the channel definition of the START MCP anode which is the same as that in the upper panel

**MMO MPPE ENA**  
**START MCP Anode Channel Definition**  
(View from START MCP input surface)



**STOP MCP Anode Channel Definition**



START sectors and STOP signals from any of the eight STOP plates. IFE also contains the necessary ADC and DAC (analog-to-digital and digital-to-analog converters) needed for HVPS control.

## (6) HVPS

One double (positive/negative) supply provides the high voltages applied to the sensor electrodes and bias voltages for MCPs, which is then regulated by optocouplers to the nominal values. Figure 79 shows a photograph of the assembled configuration of HVPS, the STOP MCP assembly, and the preamplifier/digital processing electronics boards.

3501  
3502  
3503  
3504  
3505  
3506  
3507  
3508  
3509  
3510  
3511  
3512  
3513  
3514  
3515  
3516  
3517  
3518  
3519  
3520  
3521  
3522  
3523  
3524  
3525  
3526  
3527  
3528  
3529  
3530  
3531  
3532  
3533  
3534  
3535  
3536  
3537  
3538  
3539  
3540  
3541  
3542  
3543  
3544  
3545  
3546  
3547  
3548  
3549  
3550

**Fig. 78** START surface installed in the electrode structure of the TOF section

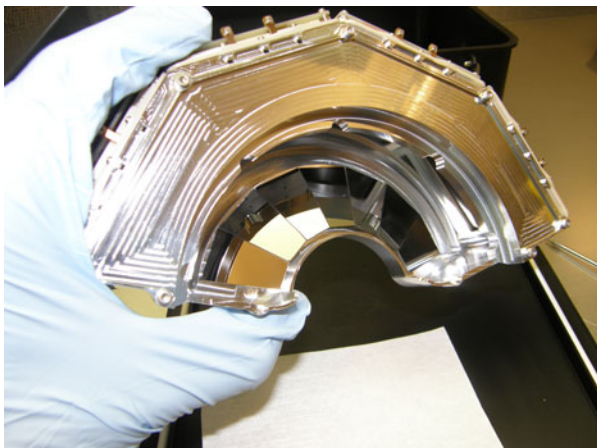
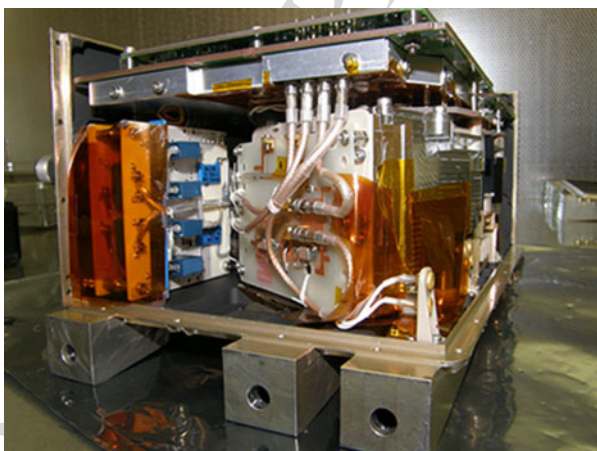


**Fig. 79** Assembled configuration of the HVPS, STOP MCP assembly, and preamplifier/digital processing electronics boards



### 3.6.2 Operation Mode and Data Products of ENA

#### Operation mode of the ENA sensor

The ENA sensor has mostly full solid angle coverage (12.0 sr FOV) for ENA detection by using spacecraft spin motion. To obtain angular resolution for the spinning direction, the spin period ( $T_s$ : nominally 4 s) is divided into 16 spin sectors, where the energy scan of 8 steps is performed for each spin sector. ENA sends a data packet with fixed size (3,072 byte = 384 byte  $\times$  8 energy steps) to MDPI every spin sector.

The ENA sensor has four operation modes: (1) coincidence mode, (2) counter mode, (3) engineering mode, and (4) table read mode. The coincidence mode provides the count and TOF values shown in Table 26. When the ENA sensor detects ENA signals, it gets four types of information such as ID of sectors (START SECTOR, START RING, and STOP SECTOR), which detect the signals, and TOF value for the time interval between the signal detection at START and STOP sectors. The ENA sensor generates raw data that contain this information in 20 bits (TOF event data, Table 27) for each event of particle detection. However, if the occurrence rate of the particle detection events is too high, the sensor cannot

**Table 26** Format of coincidence mode packet of ENA

3551			
3552	TI		48 bit
3553	packetID		8 bit (0x00)
3554	slotID		8 bit
3555	TOTAL	Incremented when signals from START SECTOR, START RING, and STOP SECTOR are detected and TOF is calculated.	16 bit
3556	COINCIDENCE		
3557	COUNT		
3558	TOTAL START		16 bit
3559	COUNT		
3560	TOTAL STOP		16 bit
3561	COUNT		
3562	COINCIDENCE	Incremented when signals from START SECTOR, START RING, and STOP SECTOR are detected and TOF is calculated.	112 bit = 7 ch × 16 bit
3563	START SECTOR		
3564	COUNT		
3564	COINCIDENCE	Incremented when signals from START SECTOR, START RING, and STOP SECTOR are detected and TOF is calculated.	128 bit = 8 ch × 16 bit
3565	STOP SECTOR		
3566	COUNT		
3567	TOF event data		N × 20 bit
3568	Remainder		Filled with zero
3569	Total		3072 bit
3570	(= (1/128) * Ts)		

3571 TI: Time indicator

3572 slotID: Incremented every energy step (= (1/128) \* Ts). Cleared by spin pulse

3573 \*1 This table shows a format for 1 energy step

3574 \*2 MDP1 will read the data every 8 energy steps

**Table 27** TOF event data

3578	START	3 bit	0: ring1, 1: ring2, 2: ring3, 3: ring4,
3579	RING		7: none
3580	START	3 bit	0: sect1, 1: sect2, 2: sect3, 3: sect4,
3581	SECTOR		4: sect5, 5: sect6, 6: sect7, 7: none
3582	STOP	1 bit	1: Difference detected in stop pulse
3583	SECTOR		numbers deduced from TDC output and
3584			FPGA count.
3585			0: No difference detected (normal)
3586		3 bit	0: sect1, 1: sect2, 2: sect3, 3: sect4,
3587			4: sect5, 5: sect6, 6: sect7, 7: sect8
3588	TOF	10 bit	0x000: This value is not generated (*).
3589			0x001-0x3ef: TOF
3590			0x3f0-0x3fc: spare
3591			0x3fd: No signal on START SECTOR
3592			0x3fe: No signal on STOP SECTOR
3593			0x3ff: No signal on both START SECTOR
3594			and STOP SECTOR

3595 \* TOF = 0x000 is dealt with no data marker by MDP1

3596 If it appears, MDP1 will not process the data appeared afterword in the packet

3597 send all of them to MDP1, where the reported data are the first 136 events per energy step.  
 3598 Therefore, the data packet of the coincidence mode contains counter values in which all  
 3599 of the corresponding events are counted. The counter mode provides the detailed counter  
 3600

**Table 28** Format of counter mode packet of ENA

3601	<b>Table 28</b> Format of counter mode packet of ENA	
3602	TI	48 bit
3603	packetID	8 bit (0x01)
3604	slotID	8 bit
3605	START RING and	448 bit = 4 ch × 7 ch × 16 bit
3606	START SECTOR	
3607	COUNT	
3608	START RING	64 bit = 4 ch × 16 bit
3609	COUNT	
3610	START SECTOR	112 bit = 7 ch × 16 bit
3611	COUNT	
3612	STOP SECTOR	128 bit = 8 ch × 16 bit
3613	COUNT	
3614	COINCIDENCE	112 bit = 7 ch × 16 bit
3615	START SECTOR	
3616	COINCIDENCE	128 bit = 8 ch × 16 bit
3617	STOP SECTOR	
3618	COUNT	Incremented when signals from START SECTOR, START RING, and STOP SECTOR are detected and TOF is calculated.
3619	TOF event data	N × 20 bit
3620	Rest	Filled with zero
3621	TOTAL	3072 bit
3622	(= (1/128) * Ts)	

\*1 Above table shows a format for 1 energy step

\*2 MDP1 will read the data every 8 energy steps

data shown in Table 28, although the maximum number of TOF event data sent to MDP1 is limited to 100 for each energy step.

When the ENA sensor is in the engineering mode, housekeeping (HK) and status data are sent to MDP1. On the other hand, the reference table of sweeping high voltages (SVs) for the energy scan is sent via the table read mode.

### Data processing in MDP1

The MDP1 receives  $24576 \text{ bit} = 3072 \text{ byte/read cycles}$ , which includes scientific data but excludes HK data. The contents of the scientific data change according to the sensor mode. After receiving the data, MDP1 decodes and reformats both types of data. The format of the data is dependent on the telemetry mode. All telemetry data transferred to the S/C must have timing information added. The time-tagging provides the acquisition time of the data.

The instrument has four telemetry modes that define the data format and data processing before transmission to ground. The MDP1 processes the data collected from the sensor and generates data sets compatible with one of the four telemetry modes. The data sets are either down-linked to ground or are stored in temporary memory on the S/C side. The telemetry modes are given below.

- (a) Mass accumulation mode
- (b) TOF accumulation mode
- (c) Count accumulation mode
- (d) Non process mode (The sensor data are downlinked with no processing in MDP1)
- (e) Idle mode (No telemetry data are generated)

3651 **Table 29** Possible combinations  
3652 of the telemetry mode with the  
3653 sensor mode of ENA

Telemetry Mode	Sensor Mode
Mass Accumulation Mode	Coincidence Mode
TOF Accumulation mode	Coincidence Mode
Count Accumulation Mode	Counter Mode
Non-Process Mode	Any
Idle Mode	Any

3658

3659

3660 There are limitations for possible combinations of the telemetry mode and the sensor mode.  
3661 Table 29 summarizes the allowable combinations.

3662

3663 In the Mass, TOF, and Count accumulation modes, the memory in the MDP1 is allocated  
3664 for count data accumulation. Data originating from the sensor is sorted by look-up tables  
3665 and is categorized into two types of accumulation matrices during a time period specified  
3666 by commands. One is the accumulation matrix as described below.

3667 **Contents:**

3668 Event data integrated during a sampling period

3669

3670 **Dimensions:**

3671 Four dimensions (E, P, C, M) for the mass accumulation mode,

3672 Two dimensions (E, TOF) for the TOF accumulation mode,

3673 Three dimensions (E, P, X) for the count accumulation mode,

3674

3675 where E is the energy group, C is the channel group, P is the phase group, M is the mass  
3676 group, TOF is time of flight, and X is the type of counters, namely START ring, START  
3677 sector, STOP plate, STOP coincidence, or START coincidence count. The other matrix is  
3678 the accumulation scaling matrix, as described below.

3679 **Contents:**

3680 Counter data summed during a sampling period

3681

3682 **Dimensions:**

3683 Three dimensions (E, P, Y) for the mass accumulation mode,

3684 Two dimensions (E, Y) for TOF accumulation mode,

3685 Not needed for the count accumulation mode,

3686

3687 where Y is the type of counters, namely total START count, total STOP count, coincidence  
3688 STOP count, coincidence START and STOP counters (seven + eight). The numbers of bins  
3689 in each element can be set by commands. Possible numbers of bins are given below.

3690  $n(C)$  1 or 7;

3691  $n(E)$  1, 2, 4, or 8;

3692  $n(P)$  1, 2, 4, 8, 16, or 32;

3693  $n(M)$  1, 2, 4, 8, 16, 32, 64 or 128;

3694  $n(\text{TOF})$  1024;

3695

3696 where  $n(\text{XX})$  means the number of bins for XX. The numbers of bins in E and P are coupled  
3697 and are not independent:

3698 If  $n(E) = 1, 2$  or  $4$  then  $n(P) = 1, 2, 4, 8, 16$ , or  $32$

3699 If  $n(E) = 8$  then  $n(P) = 1, 2, 4, 8$  or  $16$

3700



## MDP1 Data processing method on the mass accumulation mode

Data processing on MDP1 for each event consists of five steps, as given below.

3752

3753

3754

### Step 1 Obtain index of energy depending on sweep pattern

This index will later be used to obtain the actual value of the energy from the SVE table

3756

#### Energy-index:

3757

E-index = SVM-Table[SV-index, Energy-step],

3758

where SV-index is selected from table ID for the SV reference table during the observation.

3760

3761

### Step 2 Obtain derived data for mass calculation by look-up tables

3762

(a) Square root of energy:  $E_n = \text{SVE-Table}[E\text{-index}]$  (10 bit values)

3763

(b) Inv. of path length:  $L_{\text{inv}} = \text{LT}[\text{sector, ring, plate, E-index}]$  (12 bit values)

3764

(c) Flight time:  $t_1 = \text{TT}[\text{tof}]$  (10 bit values)

3765

3766

The SVE-table returns the actual particle energy corresponding to an Energy-index. Consequently, the values returned from the SVM- and SVE-tables must reflect the particle energy selected in the SV table. If  $L_{\text{inv}}$  is zero, it is regarded as an invalid event by the onboard software. When an anomaly is found on a specific START SECTOR—START RING—STOP SECTOR pair at a specific energy, it can be rejected from the onboard calculation by setting  $L_{\text{inv}} = 0$  on the LT-table. Therefore, the LT-table is designed as energy dependent. The LT-table can also compensate for a possible energy dependent energy loss on the START surface. In this case, the tof-path-length used in the mass calculation would be artificially extended for energies that have a higher relative energy loss. This was not used, however, based on the calibration results. Therefore all the path lengths used from the LT-table were the same for all energies. The TT-table returns the tof value only when  $\text{tof} \leq 0x3ef$ . If  $\text{tof} \geq 0x3f0$ , it returns 0 which is regarded as invalid event in the onboard calculation (Table 27).

3767

3768

3769

3770

3771

3772

3773

3774

3775

3776

3777

3778

3779

### Step 3 Calculate mass

Mass calculation is accomplished using 32 bit unsigned integer operations. The values of the tables in step 2 guarantee that no overflow occurs.

3780

3781

3782

$$\text{mass\_0\_5} = \left( \{ (E_n \times t_1 \times L_{\text{inv}}) / 65536 \} \times \text{Factor} \right) / 65536 \quad (1)$$

3783

3784

where Factor = 3340. If the calculated value for mass\_0\_5 is larger than 255, a value of 255 must be assigned to mass\_0\_5 prior to further processing. The value calculated here is actually proportional to the square root of the mass.

3785

3786

3787

3788

### Step 4 Bin the data according to the binning parameters set

3789

3790

$$(a) \text{ mass group } M = \text{MT}[\text{mass\_0\_5}] / \{128/n(M)\} \quad (2)$$

3791

$$(b) \text{ channel group } C = \text{sector} / \{7/n(C)\} \quad (3)$$

3792

$$(c) \text{ energy group } E = \text{Energy\_step} \text{ modulo } n(E) \quad (4)$$

3793

$$(d) \text{ phase group } P = (\text{phase} - \text{phasemin}) / \{32/n(P)\} \quad (5)$$

3794

3795

3796

Where phasemin contains the first spin phase value to be considered, whereas phasemax is the last phase value to be considered. To use all phase values, phasemin = 0, phasemax = 31. All divisions in equations (2)–(5) are integer divisions.

3797

3798

3799

3800

## 3801 **Step 5 Update the accumulation and the accumulation scaling matrix**

3802 Accumulation matrix (M, C, E, P) = Accumulation matrix (M, C, E, P) + 1

3803 Accumulation scaling matrix (E, P, Y) = Accumulation matrix (E, P, Y) + 1

3804  
3805 This calculation is required for all events in a packet.

### 3806 **Count accumulation mode**

3807 This mode is used to obtain the detailed signal count at each MCP plate and is similar to  
3808 the mass accumulation mode, except that counter data are summed. When count accumula-  
3809 tion mode is set, the sensor always needs to be set to the counter mode. In this mode, instead  
3810 of receiving coincidence events, MDP1 receives detailed total counts on each MCP anode  
3811 during one energy step. Then the total count data are summed as the accumulation matrix.  
3812 This accumulation is made over a particular time set by a command, and the contents of the  
3813 accumulation matrix are sent to S/C.

### 3814 **TOF accumulation mode**

3815 This mode is used to obtain raw TOF distributions without mass information. The pri-  
3816 mary uses of the raw TOF data are to analyze the performance of the instrument and to cali-  
3817 brate the on-board mass calculations. This mode is similar to the mass accumulation mode,  
3818 except that TOF data are accumulated instead of mass data. In TOF accumulation mode, the  
3819 mass is not calculated, and the raw TOF data are directly used for the accumulation instead  
3820 of the mass. The accumulation matrix in this mode has two dimensions: E (energy) and T  
3821 (TOF). MDP1 does not use the other parameters of P (phase) and C (channel). Because TOF  
3822 data have 10 bits, the number of TOF bins is always 1024.

### 3823 **3.6.3 Pre-flight Calibration of ENA**

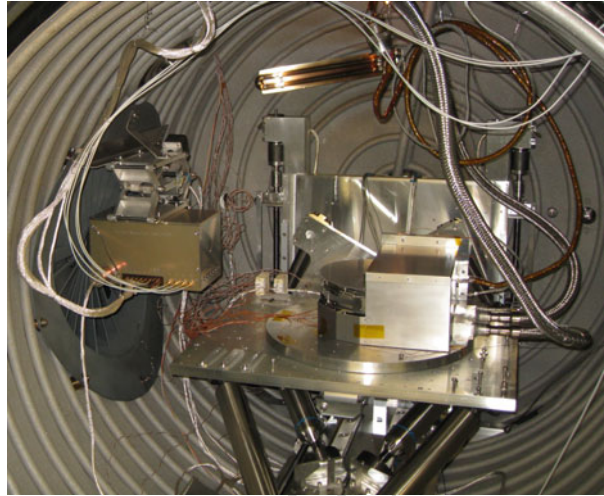
3824 The instrument was calibrated at the Messkammer für Flugzeitinstrumente und Time-of-  
3825 flight (MEFISTO) calibration facility (Marti et al. 2001) at the University of Bern. The  
3826 facility produces an energetic neutral atom beam by neutralizing a collimated ion beam on a  
3827 conversion surface (Wieser and Wurz 2005). The beam neutralizer is an integral part of the  
3828 MEFISTO facility and produces a neutral beam of known composition, well-characterized in  
3829 angle and energy. For the instrument calibration, neutral H, neutral He and neutral O beams  
3830 were produced in an energy range from 30–3000 eV per particle. During the calibration the  
3831 instrument was mounted on the MEFISTO hexapod turntable, which enabled rotation and  
3832 translation of instrument relative to the fixed energetic neutral atom beam. An additional  
3833 thermal heating/cooling plate enabled performance investigation at different temperatures  
3834 (Fig. 81).

3835 The calibration was split into four phases between 2012 and 2014 with interspersed cali-  
3836 bration data analysis phases. This approach enabled to repeat measurements that had in-  
3837 sufficient statistics and other quality problems detected during the data analysis. The cali-  
3838 bration tasks were separated into establishing energy response, angular response and mass  
3839 response.

### 3840 **Energy response**

3841 The energy response of ENA is determined by the electrostatic wave energy analysis sys-  
3842 tem and the energy loss function on the conversion surface. The latter strongly depends on  
3843 species and energy, which makes the energy response species and energy dependent. To sim-  
3844 plify operations, only 16 different energy settings were characterized, with each identified  
3845

3851 **Fig. 81** ENA at the MEFISTO  
3852 calibration facility. The neutral  
3853 beam is emitted from the beam  
3854 neutralizer on the left (gold box).  
3855 ENA (center) is encapsulated in  
3856 thermal insulation sheets to  
3857 facilitate temperature control.  
3858 The entire instrument setup can  
3859 be moved and rotated relative to  
3860 the incoming neutral beam with  
3861  $6^\circ$  of freedom

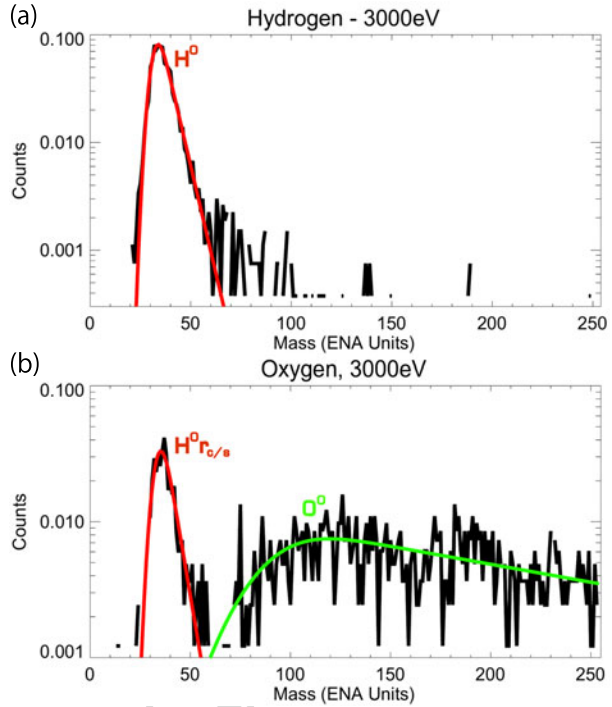


3869 **Table 30** Calibrated energy bin  
3870 centers for hydrogen and oxygen  
3871

E-Index	Nominal center energy (eV)	Hydrogen (eV)	Oxygen (eV)
0	0	0	0
1	10	20	8
2	20	37	15
3	40	67	29
4	80	120	54
5	160	215	103
6	320	387	196
7	640	693	370
8	1280	1243	699
9	2560	2228	1321
10	56	89	39
11	112	159	74
12	224	286	141
13	448	513	267
14	896	920	504
15	1792	1650	953

3872  
3873  
3874  
3875  
3876  
3877  
3878  
3879  
3880  
3881  
3882  
3883  
3884  
3885  
3886  
3887  
3888  
3889  
3890  
3891  
3892  
3893 by an index and nominal center energy for bookkeeping purposes. The actual peak energy of  
3894 each energy bin is species dependent (Table 30). The actual energy sweep in the instrument  
3895 consisted of eight energy settings selected from this table. The width of the energy pass band  
3896  $\Delta E$  for hydrogen is energy independent with  $\Delta E/E = 100\%$ , with E as the nominal center  
3897 energy. The energy pass bands for oxygen have a tail toward higher energies owing to the  
3898 more prominent energy loss at the conversion surface. The quantitative extent of this effect  
3899 needs further analysis.

3901 **Fig. 82** Typical mass spectra for  
 3902 incident neutral hydrogen (top)  
 3903 and oxygen (bottom). The black  
 3904 lines show the measured data, the  
 3905 colored lines are fitted curves.  
 3906  $H^0$ : hydrogen peak,  $O^0$ : oxygen  
 3907 peak,  $H^0_{rc/s}$ : hydrogen signal  
 3908 owing to a recoil process at the  
 3909 conversion surface. The X-axis in  
 3910 both plots is in mass bin units M  
 3911 as shown in Fig. 80 and the  
 3912 Y-axis is in arbitrary units  
 3913  
 3914  
 3915  
 3916  
 3917  
 3918  
 3919  
 3920  
 3921  
 3922  
 3923  
 3924



3925 **Table 31** Calibrated angular  
 3926 response

Start sector	0	1	2	3	4	5	6
$\theta_0$ (°)	67.1	40.8	16.9	-3.0	-24.2	-46.3	-68.1
$\beta_0$ (°)	-5.4	-5.8	-6.5	-5.3	-5.8	-5.6	-5.2
$\Delta\theta$ (°)	32.8	28.9	25.8	27.0	21.8	21.5	22.9
$\Delta\beta$ (°)	11.6	10.5	9.9	9.0	7.7	7.8	7.1

3927  
 3928  
 3929  
 3930  
 3931  
 3932  
 3933 **Angular response**

3934 The angular response was determined by rotating the instrument relative to an incident  
 3935 neutral hydrogen beam in a grid like pattern. The count rates obtained from each START  
 3936 sector were then fitted with 2D angular Gaussian profiles. Table 31 shows the bore sight  
 3937 directions and widths of each of the seven viewing directions corresponding to the seven  
 3938 START sectors.  $\theta_0$  denotes the center in azimuth,  $\beta_0$  is the center in the elevation direction,  
 3939 and  $\Delta\theta$  and  $\Delta\beta$  are the FWHM values of the fitted peak widths. The coordinate system  
 3940 used is shown in Fig. 72. The azimuthal resolution  $\Delta\theta$  varies linearly between 32.5° at  
 3941 sector 0 and 22.9° at sector 6, and the elevation resolution  $\Delta\beta$  decreases linearly between  
 3942 11.6° at sector 0 and 7.1° at sector 6. We believe this trend to be a result of a mechanical  
 3943 misalignment between the wave system and the TOF cell. The angular response is in first  
 3944 order not energy dependent.  
 3945

3946 **Mass response**

3947 The TOF values measured onboard are converted to a nearly energy independent mass  
 3948 number M in the range from 0–255. Before reporting to telemetry, M is converted to a mass  
 3949 group number compatible with the selected binning parameters by using a mass lookup  
 3950

**Table 32** Selected estimated geometric factors not including detection probability for neutral hydrogen. Values indicated with n/a are not yet available

E-Index	Nominal center energy (eV)	G for hydrogen without detection probability (cm <sup>2</sup> sr eV/eV)
0	0	n/a
1	10	n/a
2	20	n/a
3	40	$0.9 \times 10^{-7}$
4	80	$1.2 \times 10^{-7}$
5	160	$1.9 \times 10^{-7}$
6	320	$2.5 \times 10^{-7}$
7	640	$0.5 \times 10^{-6}$
8	1280	n/a
9	2560	n/a
10	56	$1.0 \times 10^{-7}$
11	112	n/a
12	224	n/a
13	448	$3.6 \times 10^{-7}$
14	896	n/a
15	1792	n/a

table and possible further division by using a constant, as shown in Fig. 80. For calibration data analysis the mass number M was used to establish the shapes of the different mass peaks in the mass spectrum. The shape of the hydrogen mass peak is shown in Fig. 82(a). Owing to its larger mass, oxygen might generate hydrogen recoils at the conversion surface, which can result in an additional hydrogen peak even when the conversion surface is hit by oxygen only (Fig. 82(b)). The intensity of the additional hydrogen signal depends mainly on the amount of water absorbed on the conversion surface. The mass spectrum to neutral helium is more complicated because both recoil hydrogen and recoil oxygen atoms appear. For the case of incident neutral oxygen, a mass comprehensive cross-talk matrix could be generated, which enables separation of the individual recoil contributions. The matrix for incident neutral helium is sparser owing to limited calibration time available for helium.

### Geometric factor

In its simplest form the geometric factor G is expressed as

$$G = \Delta E/E \times \Delta \Omega \times \Delta A \times \epsilon \tag{6}$$

where  $\Delta E/E$  is the energy resolution,  $\Delta A$  is the effective aperture area,  $\Delta \Omega = \Delta \theta \times \Delta \beta$  is the angular acceptance, and  $\epsilon$  is the detection probability. The first two factors energy response and angular response are well established. The detection probability for both START and STOP detectors is obtained from the START and STOP rates in the TOF cell (Funsten et al. 2005). Typical observed values for hydrogen are 1% at 100 eV increasing to 30% at 1000 eV. The best estimates for the geometric factor for neutral hydrogen are listed in Table 32.

### 3.6.4 Near-Earth Commissioning Results of ENA

The temperature of the conversion surface is controlled to remain above +50 °C throughout the mission to avoid a stack of contaminating materials which would decrease the efficiency

**Table 33** MPPE data mode and L-mode data products of LEP and HEP sensors

MPPE mode name	L-mode data products
1. Default Observation Mode	MEA1: Et-OMN, Et-PAP, VM, 3D-LL MEA2: Et-OMN, Et-PAP, VM MIA: Et-M1, VM-M1, 3D-LL-M1 MSA: Low [Moments, Omni E-t, TOF] HEP: L-mode
2. Exospheric Mode	MEA1: Et-OMN, Et-PAP, VM, 3D-LL MEA2: Et-OMN, Et-PAP, VM MIA: Et-M2, VM-M2, 3D-LL-M2 MSA: Low [Moments, Omni E-t, TOF] HEP: L-mode
3. Solar Wind Mode/IP Shock Local Mode	MEA1: Et-OMN, Et-PAP, VM, 3D-LL MEA2: Et-OMN, Et-PAP, VM MIA: Et-M1, VM-M1, 3D-LL-M1 MSA: Low [Moments, Omni E-t, TOF] HEP: L-mode
4. IP Shock Macro Mode/Bow Shock Mode	MEA1: Et-OMN, Et-PAP, VM, 3D-LL MEA2: Et-OMN, Et-PAP, VM MIA: Et-M1, VM-M1, 3D-LL-M1 MSA: Low [Moments, Omni E-t, TOF] HEP: L-mode
5. Reconnection Mode	MEA1: Et-OMN, Et-PAP, VM, 3D-LL MEA2: Et-OMN, Et-PAP, VM MIA: Et-M3, VM-M3, 3D-LL-M3 MSA: Low [Moments, Omni E-t, TOF] HEP: L-mode
6. Magnetospheric Mode	MEA1: Et-OMN, Et-PAP, VM, 3D-LL MEA2: Et-OMN, Et-PAP, VM MIA: Et-M3, VM-M3, 3D-LL-M3 MSA: Low [Moments, Omni E-t, TOF] HEP: L-mode

of neutral to ion conversion. So far, the temperature has been successfully maintained above +50 °C, except for some cases of short duration that did not affect the conversion performance because the temperature was still greater than that of the surrounding structures. The power for the ENA heater control and temperature monitoring system (ENA HCS) is separated from the other ENA electronics.

Except for a high-voltage unit, ENA was activated on November 25, 2018 for the first time after the launch. No problems were found during the test. The ENA function tests with the HVPS were conducted on June 27 and 28, 2019; August 20 and 22, 2019; and February 6 and 7, 2020. These tests were conducted when the spacecraft was in the solar wind. During the testing, all of the high-voltage outputs were gradually increased up to their nominal set-

**Table 34** MPPE data mode and M-mode data products of LEP and HEP sensors

MPPE mode name	M-mode data products
1. Default Observation Mode	MEA1: Et-OMNm, Et-PAP, VM, 3D-M MEA2: Et-OMNm, Et-PAP, VM MIA: 3D-L2-M1 or SW-L2-M1 MSA: Med A [Moment, 3D-VDF(A), AD(A), TOF(A)] HEP: M-mode
2. Exospheric Mode	MEA1: Et-OMNm, Et-PAP, VM, 3D-M MEA2: Et-OMNm, Et-PAP, VM MIA: 3D-L2-M2 MSA: Med D [Moment, 3D-VDF(D), AD(D), TOF(D)] HEP: M-mode
3. Solar Wind Mode/IP Shock Local Mode	MEA1: Et-OMNm, Et-PAP, VM, 3D-M MEA2: Et-OMNm, Et-PAP, VM MIA: 3D-L2-M1 or SW-L2-M1 MSA: Med C [Moment, 3D-VDF(C), AD(C), TOF(C)] HEP: M-mode
4. IP Shock Macro Mode/Bow Shock Mode	MEA1: Et-OMNm, Et-PAP, VM, 3D-M MEA2: Et-OMNm, Et-PAP, VM MIA: 3D-L2-M1 or SW-L2-M1 MSA: Med C [Moment, 3D-VDF(C), AD(C), TOF(C)] HEP: M-mode
5. Reconnection Mode	MEA1: Et-OMNm, Et-PAP, VM, 3D-M MEA2: Et-OMNm, Et-PAP, VM MIA: 3D-L2-M3 MSA: Med C [Moment, 3D-VDF(C), AD(C), TOF(C)] HEP: M-mode
6. Magnetospheric Mode	MEA1: Et-OMNm, Et-PAP, VM, 3D-M MEA2: Et-OMNm, Et-PAP, VM MIA: 3D-L2-M3 MSA: Med D [Moment, 3D-VDF(D), AD(D), TOF(D)] HEP: M-mode

tings for the actual observation. For the input surface of START and STOP MCPs,  $-2300$  V and  $-2600$  V were applied, respectively, where dark counts were successfully detected by all input channels of the pre-amplifiers. For the other electrodes, voltage sweeping for energy analysis was also tested with no problems detected. However, no valid ENA counts were identified during the testing, because the FOV of ENA is mostly blocked by MOSIF during the cruising phase. Although part of the FOV of ENA is not blocked by MOSIF, the unblocked direction is not pointed toward the Sun. In this case, faint ENA flux is expected in the solar wind.

**Table 35** MPPE data mode and H-mode data products of LEP and HEP sensors

MPPE mode name	H-mode data products
1. Default Observation Mode	N.A.
2. Exospheric Mode	MEA1: 3D-H MEA2: 3D-H MIA: 3D-H-M2 MSA: High B [Moment, 3D-VDF(B), TOF(B), EVENT(B)] HEP: H-mode
3. Solar Wind Mode/IP Shock Local Mode	MEA1: 3D-H MEA2: 3D-H MIA: SW-L-M1, 3D-L2-M1 MSA: High B [Moment, 3D-VDF(B), TOF(B), EVENT(B)] HEP: H-mode
4. IP Shock Macro Mode/Bow Shock Mode	MEA1: 3D-H MEA2: 3D-H MIA: SW-L-M1, 3D-L2-M1 MSA: High B [Moment, 3D-VDF(B), TOF(B), EVENT(B)] HEP: H-mode
5. Reconnection Mode	MEA1: 3D-H MEA2: 3D-H MIA: 3D-H-M3 MSA: High B [Moment, 3D-VDF(B), TOF(B), EVENT(B)] HEP: H-mode
6. Magnetospheric Mode	MEA1: 3D-H MEA2: 3D-H MIA: 3D-H-M3 MSA: High B [Moment, 3D-VDF(B), TOF(B), EVENT(B)] HEP: H-mode

ENA will be activated during the Earth and Venus fly-bys before the Mercury orbit insertion to measure ENAs generated by charge-exchange interactions between hot ions and cold atmospheric neutrals.

#### 4 Data Products of MPPE

To conduct coordinated observation between the MPPE sensors and to control the total telemetry data rate, the MPPE data mode is defined. The operation mode of LEP and HEP sensors are determined so that they generate the data products depending on the MPPE data mode. Because ENA generates only L-mode data with fixed data rates, it is operated independently of the MPPE data mode. Six MPPE data modes are defined: default observation mode, exospheric mode, solar wind mode/IP shock local mode, IP shock macro mode/bow shock mode, reconnection mode, and magnetospheric mode. Tables 33, 34, 35 show the

4151 MPPE data mode and the corresponding data products of LEP and HEP sensors for L-mode,  
4152 M-mode, and H-mode data, respectively.

4153  
4154

## 4155 5 Conclusion

4156  
4157

4158 All of the MPPE analyzers have concluded initial commissioning with no significant prob-  
4159 lems reported. Because MOSIF blocks most of the FOVs of the MPPE sensors, it will be  
4160 difficult for the ion sensors (MIA, MSA, and HEP-ion) to measure the solar wind during the  
4161 cruise phase before arriving at Mercury. Only the low energy electron sensors MEA1 and  
4162 MEA2 can measure part of the solar wind electron phase space density because the thermal  
4163 speed of electrons is higher than the solar wind bulk velocity. During the Earth, Venus, and  
4164 Mercury fly-bys, we expect most of the MPPE sensors to be turned on. If BepiColombo will  
4165 pass through magnetosphere, the ion sensors might also be able to measure natural counts.  
4166 Therefore, events provide good opportunities to check the analyzer functions including the  
4167 data processing software using natural data.

4168 During the Venus fly-bys scheduled in October 2020 and August 2021, we plan to use  
4169 MEA1, MEA2, MIA, MSA, HEP-ele, and ENA to make observations. MEA1 and MEA2  
4170 will be able to observe electrons in the solar wind and around Venus, and ENA might be  
4171 capable of measuring the energetic neutral atoms from Venus. Although it may be difficult  
4172 for MIA and MSA to obtain meaningful ion data, activating the instrument and operating the  
4173 analyzers will refresh the instrument operation skills and facilitate observation immediately  
4174 after arriving at Mercury. During the Mercury fly-bys scheduled in October 2021, June 2022,  
4175 June 2023, September 2024, December 2024 and January 2025, the MPPE sensors will  
4176 be activated; detailed observation plans will be considered in the future. After arriving at  
4177 Mercury in December 2025, all of the MPPE analyzers will make continuous observations  
4178 except for periods in which the operations are limited owing to the thermal constraints of  
4179 the spacecraft.

4180  
4181 **Acknowledgements** The authors thank all the members of BepiColombo mission for their unstinted efforts in  
4182 making the mission fruitful and for their valuable discussion on the specifications and operations of payload  
4183 instruments including our MPPE sensors.

4184  
4185

## 4186 Declarations

4187  
4188

4189 **Conflict of Interest** The authors declare that they have no conflict of interest.

4190  
4191

## 4192 References

4193  
4194

- 4195 T. Amano, T. Katou, N. Kitamura, M. Oka, Y. Matsumoto, M. Hoshino, Y. Saito, S. Yokota, B.L. Giles,  
4196 W.R. Paterson, C.T. Russell, O. Le Contel, R.E. Ergun, P.A. Lindqvist, D.L. Turner, J.F. Fennell,  
4197 J.B. Blake, Observational evidence for stochastic shock drift acceleration of electrons at the Earth's  
4198 bow shock. *Phys. Rev. Lett.* **124**, 065,101 (2020). <https://doi.org/10.1103/PhysRevLett.124.065101>
- 4199 B.J. Anderson, C.L. Johnson, H. Korth, M.E. Purucker, R.M. Winslow, J.A. Slavin, S.C. Solomon, R.L. Mc-  
4200 Nutt, J.M. Raines, T.H. Zurbuchen, The global magnetic field of Mercury from MESSENGER orbital  
4201 observations. *Science* **333**(6051), 1859–1862 (2011). <https://doi.org/10.1126/science.1211001>
- 4202 B.J. Anderson, C.L. Johnson, H. Korth, J.A. Slavin, R.M. Winslow, R.J. Phillips, R.L. McNutt Jr.,  
4203 S.C. Solomon, Steady-state field-aligned currents at Mercury. *Geophys. Res. Lett.* **41**(21), 7444–7452  
4204 (2014). <https://doi.org/10.1002/2014GL061677>

- 4201 S. Barabash, R. Lundin, H. Andersson, K. Brinkfeldt, A. Grigoriev, H. Gunell, M. Holmström, M. Yamauchi, K. Asamura, P. Bochsler, P. Wurz, R. Cerulli-Irelli, A. Mura, A. Milillo, M. Maggi, S. Orsini, A.J. Coates, D.R. Linder, D.O. Kataria, C.C. Curtis, K.C. Hsieh, B.R. Sandel, R.A. Frahm, J.R. Sharber, J.D. Winningham, M. Grande, E. Kallio, H. Koskinen, P. Riihelä, W. Schmidt, T. Säles, J.U. Kozyra, N. Krupp, J. Woch, S. Livi, J.G. Luhmann, S. McKenna-Lawlor, E.C. Roelof, D.J. Williams, J.A. Sauvaud, A. Fedorov, J.J. Thocaven, The Analyzer of Space Plasmas and Energetic Atoms (ASPERA-3) for the Mars Express mission. *Space Sci. Rev.* **126**(1), 113–164 (2006). <https://doi.org/10.1007/s11214-006-9124-8>
- 4202 S. Barabash, J.A. Sauvaud, H. Gunell, H. Andersson, A. Grigoriev, K. Brinkfeldt, M. Holmström, R. Lundin, M. Yamauchi, K. Asamura, W. Baumjohann, T. Zhang, A. Coates, D. Linder, D. Kataria, C. Curtis, K. Hsieh, B. Sandel, A. Fedorov, C. Mazelle, J.J. Thocaven, M. Grande, H.E. Koskinen, E. Kallio, T. Säles, P. Riihela, J. Kozyra, N. Krupp, J. Woch, J. Luhmann, S. McKenna-Lawlor, S. Orsini, R. Cerulli-Irelli, M. Mura, M. Milillo, M. Maggi, E. Roelof, P. Brandt, C. Russell, K. Szego, J. Winningham, R. Frahm, J. Scherrer, J. Sharber, P. Wurz, P. Bochsler, The Analyser of Space Plasmas and Energetic Atoms (ASPERA-4) for the Venus Express mission. *Planet. Space Sci.* **55**(12), 1772–1792 (2007). <https://doi.org/10.1016/j.pss.2007.01.014>. The Planet Venus and the Venus Express Mission, Part 2
- 4203 T.A. Cassidy, A.W. Merkel, M.H. Burger, M. Sarantos, R.M. Killen, W.E. McClintock, R.J. Vervack, Mercury’s seasonal sodium exosphere: MESSENGER orbital observations. *Icarus* **248**, 547–559 (2015). <https://doi.org/10.1016/j.icarus.2014.10.037>
- 4204 E.W. Cliver, J. Feynman, H.B. Garrett, An estimate of the maximum speed of the solar wind, 1938–1989. *J. Geophys. Res. Space Phys.* **95**(A10), 17,103–17,112 (1990). <https://doi.org/10.1029/JA095iA10p17103>
- 4205 D.C. Delcourt, S. Grimald, F. Leblanc, J.J. Berthelier, A. Millilo, A. Mura, S. Orsini, T.E. Moore, A quantitative model of the planetary  $\text{Na}^+$  contribution to Mercury’s magnetosphere. *Ann. Geophys.* **21**(8), 1723–1736 (2003). <https://doi.org/10.5194/angeo-21-1723-2003>
- 4206 D. Delcourt, Y. Saito, F. Leblanc, C. Verdeil, S. Yokota, M. Fraenz, H. Fischer, B. Fiethe, B. Katra, D. Fontaine, J.M. Illiano, J.J. Berthelier, N. Krupp, U. Buhrke, F. Bubenhausen, H. Michalik, The Mass Spectrum Analyzer (MSA) on board the BepiColombo MMO. *J. Geophys. Res. Space Phys.* **121**(7), 6749–6761 (2016). <https://doi.org/10.1002/2016JA022380>
- 4207 M.I. Desai, G.M. Mason, M.E. Wiedenbeck, C.M.S. Cohen, J.E. Mazur, J.R. Dwyer, R.E. Gold, S.M. Krimigis, Q. Hu, C.W. Smith, R.M. Skoug, Spectral properties of heavy ions associated with the passage of interplanetary shocks at 1 AU. *Astrophys. J.* **611**(2), 1156–1174 (2004). <https://doi.org/10.1086/422211>
- 4208 R.M. Dewey, J.A. Slavin, J.M. Raines, D.N. Baker, D.J. Lawrence, Energetic electron acceleration and injection during dipolarization events in Mercury’s magnetotail. *J. Geophys. Res. Space Phys.* **122**(12), 12,170–12,188 (2017). <https://doi.org/10.1002/2017JA024617>
- 4209 G.A. DiBaccio, J.A. Slavin, S.M. Imber, D.J. Gershman, J.M. Raines, C.M. Jackman, S.A. Boardsen, B.J. Anderson, H. Korth, T.H. Zurbuchen, R.L. McNutt, S.C. Solomon, MESSENGER observations of flux ropes in Mercury’s magnetotail. *Planet. Space Sci.* **115**, 77–89 (2015). <https://doi.org/10.1016/j.pss.2014.12.016>. Solar wind interaction with the terrestrial planets
- 4210 S. Fatemi, A.R. Poppe, S. Barabash, Hybrid simulations of solar wind proton precipitation to the surface of Mercury. *J. Geophys. Res. Space Phys.* **125**(4), e2019JA027706 (2020). <https://doi.org/10.1029/2019JA027706>
- 4211 L.A. Fisk, G. Gloeckler, Particle acceleration in the heliosphere: implications for astrophysics. *Space Sci. Rev.* **173**(1), 433–458 (2012). <https://doi.org/10.1007/s11214-012-9899-8>
- 4212 N.J. Fox, M.C. Velli, S.D. Bale, R. Decker, A. Driesman, R.A. Howard, J.C. Kasper, J. Kinnison, M. Kusterer, D. Lario, M.K. Lockwood, D.J. McComas, N.E. Raouafi, A. Szabo, The Solar Probe Plus mission: humanity’s first visit to our star. *Space Sci. Rev.* **204**(1), 7–48 (2016). <https://doi.org/10.1007/s11214-015-0211-6>
- 4213 H.O. Funsten, S.M. Ritzau, R.W. Harper, Negative helium ions exiting a carbon foil at keV energies. *Phys. Rev. B* **63**, 155,416 (2001). <https://doi.org/10.1103/PhysRevB.63.155416>
- 4214 H.O. Funsten, R.W. Harper, D.J. McComas, Absolute detection efficiency of space-based ion mass spectrometers and neutral atom imagers. *Rev. Sci. Instrum.* **053**, 301 (2005). <https://doi.org/10.1063/1.1889465>
- 4215 Y. Futaana, S. Barabash, M. Wieser, P. Wurz, D. Hurlley, M. Horányi, U. Mall, N. Andre, N. Ivchenko, J. Oberst, K. Retherford, A. Coates, A. Masters, J.E. Wahlund, E. Kallio, SELMA mission: how do airless bodies interact with space environment? The Moon as an accessible laboratory. *Planet. Space Sci.* **156**, 23–40 (2018). <https://doi.org/10.1016/j.pss.2017.11.002>. Dust, Atmosphere, and Plasma Environment of the Moon and Small Bodies
- 4216 A.B. Galvin, L.M. Kistler, M.A. Popecki, C.J. Farrugia, K.D.C. Simunac, L. Ellis, E. Möbius, M.A. Lee, M. Boehm, J. Carroll, A. Crawshaw, M. Conti, P. Demaine, S. Ellis, J.A. Gaidos, J. Googins, M. Granoff, A. Gustafson, D. Heirtzler, B. King, U. Knauss, J. Levasseur, S. Longworth, K. Singer, S. Turco,
- 4217
- 4218
- 4219
- 4220
- 4221
- 4222
- 4223
- 4224
- 4225
- 4226
- 4227
- 4228
- 4229
- 4230
- 4231
- 4232
- 4233
- 4234
- 4235
- 4236
- 4237
- 4238
- 4239
- 4240
- 4241
- 4242
- 4243
- 4244
- 4245
- 4246
- 4247
- 4248
- 4249
- 4250

- 4251 P. Vachon, M. Vosbury, M. Widholm, L.M. Blush, R. Karrer, P. Bochsler, H. Daoudi, A. Etter, J. Fischer, J. Jost, A. Opitz, M. Sigrist, P. Wurz, B. Klecker, M. Ertl, E. Seidenschwang, R.F. Wimmer-Schweingruber, M. Koeten, B. Thompson, D. Steinfeld, The Plasma and Suprathermal Ion Composition (PLASTIC) investigation on the STEREO observatories. *Space Sci. Rev.* **136**(1), 437–486 (2008). <https://doi.org/10.1007/s11214-007-9296-x>
- 4252
- 4253
- 4254
- 4255 D.J. Gershman, J.A. Slavin, J.M. Raines, T.H. Zurbuchen, B.J. Anderson, H. Korth, D.N. Baker, S.C. Solomon, Ion kinetic properties in Mercury’s pre-midnight plasma sheet. *Geophys. Res. Lett.* **41**(16), 5740–5747 (2014). <https://doi.org/10.1002/2014GL060468>
- 4256
- 4257
- 4258 D.J. Gershman, J.M. Raines, J.A. Slavin, T.H. Zurbuchen, T. Sundberg, S.A. Boardsen, B.J. Anderson, H. Korth, S.C. Solomon, MESSENGER observations of multiscale Kelvin–Helmholtz vortices at Mercury. *J. Geophys. Res. Space Phys.* **120**(6), 4354–4368 (2015). <https://doi.org/10.1002/2014JA020903>
- 4259
- 4260 M. Grande, Investigation of magnetospheric interactions with the Hermean surface. *Adv. Space Res.* **19**(10), 1609–1614 (1997). [https://doi.org/10.1016/S0273-1177\(97\)00374-8](https://doi.org/10.1016/S0273-1177(97)00374-8). Proceedings of the BO.1 Symposium of COSPAR Scientific Commission B
- 4261
- 4262
- 4263 H. Hasegawa, M. Fujimoto, T.D. Phan, H. Rème, A. Bologh, M.W. Dunlop, C. Hashimoto, R. TanDokoro, Transport of solar wind into Earth’s magnetosphere through rolled-up Kelvin–Helmholtz vortices. *Nature* **430**(7001), 755–758 (2004). <https://doi.org/10.1038/nature02799>
- 4264
- 4265 D. Heyner, C. Nabert, E. Liebert, K.H. Glassmeier, Concerning reconnection–induction balance at the magnetopause of Mercury. *J. Geophys. Res. Space Phys.* **121**(4), 2935–2961 (2016). <https://doi.org/10.1002/2015JA021484>
- 4266
- 4267 G.C. Ho, D. Lario, R.B. Decker, C.W. Smith, Q. Hu, Transient shocks and associated energetic particle distributions observed by ACE during cycle 23. *AIP Conf. Proc.* **1039**(1), 184–189 (2008). <https://doi.org/10.1063/1.2982443>
- 4268
- 4269
- 4270 G.C. Ho, S.M. Krimigis, R.E. Gold, D.N. Baker, J.A. Slavin, B.J. Anderson, H. Korth, R.D. Starr, D.J. Lawrence, R.L. McNutt, S.C. Solomon, MESSENGER observations of transient bursts of energetic electrons in Mercury’s magnetosphere. *Science* **333**(6051), 1865–1868 (2011). <https://doi.org/10.1126/science.1211141>
- 4271
- 4272
- 4273 D. Hovestadt, M. Hilchenbach, A. Bürgi, B. Klecker, P. Laeverenz, M. Scholer, H. Grünwaldt, W.I. Axford, S. Livi, E. Marsch, B. Wilken, H.P. Winterhoff, F.M. Ipavich, P. Bedini, M.A. Coplan, A.B. Galvin, G. Gloeckler, P. Bochsler, H. Balsiger, J. Fischer, J. Geiss, R. Kallenbach, P. Wurz, K.U. Reiche, F. Gliem, D.L. Judge, H.S. Ogawa, K.C. Hsieh, E. Möbius, M.A. Lee, G.G. Managadze, M.I. Verigin, M. Neugebauer, CELIAS—charge, element and isotope analysis system for SOHO. *Sol. Phys.* **162**(1), 441–481 (1995). <https://doi.org/10.1007/BF00733436>
- 4274
- 4275
- 4276
- 4277
- 4278 A.J. Hundhausen, T.E. Holzer, B.C. Low, Do slow shocks precede some coronal mass ejections? *J. Geophys. Res. Space Phys.* **92**(A10), 11,173–11,178 (1987). <https://doi.org/10.1029/JA092iA10p11173>
- 4279
- 4280 S.M. Imber, J.A. Slavin, MESSENGER observations of magnetotail loading and unloading: implications for substorms at Mercury. *J. Geophys. Res. Space Phys.* **122**(11), 11,402–11,412 (2017). <https://doi.org/10.1002/2017JA024332>
- 4281
- 4282 S.M. Imber, J.A. Slavin, S.A. Boardsen, B.J. Anderson, H. Korth, R.L. McNutt Jr., S.C. Solomon, MESSENGER observations of large dayside flux transfer events: do they drive Mercury’s substorm cycle? *J. Geophys. Res. Space Phys.* **119**(7), 5613–5623 (2014). <https://doi.org/10.1002/2014JA019884>
- 4283
- 4284
- 4285 W.H. Ip, The sodium exosphere and magnetosphere of Mercury. *Geophys. Res. Lett.* **13**(5), 423–426 (1986). <https://doi.org/10.1029/GL013i005p00423>
- 4286
- 4287 E. Kallio, P. Janhunen, Solar wind and magnetospheric ion impact on Mercury’s surface. *Geophys. Res. Lett.* **30**(17), 1877 (2003). <https://doi.org/10.1029/2003GL017842>
- 4288
- 4289 Y. Kasaba, T. Takashima, S. Matsuda, S. Eguchi, M. Endo, T. Miyabara, M. Taeda, Y. Kuroda, Y. Kasahara, T. Imachi, H. Kojima, S. Yagitani, M. Moncuquet, J.E. Wahlund, A. Kumamoto, A. Matsuoka, W. Baumjohann, S. Yokota, K. Asamura, Y. Saito, D. Delcourt, M. Hirahara, S. Barabash, N. Andre, M. Kobayashi, I. Yoshikawa, G. Murakami, H. Hayakawa, Mission data processor aboard the Bepi-Colombo Mio spacecraft: design and scientific operation concept. *Space Sci. Rev.* **216**(3), 34 (2020). <https://doi.org/10.1007/s11214-020-00658-x>
- 4290
- 4291
- 4292
- 4293 S. Kasahara, T. Mitani, K. Ogasawara, T. Takashima, M. Hirahara, K. Asamura, Application of single-sided silicon strip detector to energy and charge state measurements of medium energy ions in space. *Nucl. Instrum. Methods Phys. Res., Sect. A. Accel. Spectrom. Detect. Assoc. Equip.* **603**(3), 355–360 (2009). <https://doi.org/10.1016/j.nima.2009.02.004>
- 4294
- 4295
- 4296 Y. Kazama, S. Barabash, M. Wieser, K. Asamura, P. Wurz, A LENA instrument onboard BepiColombo and Chandrayaan-1. *AIP Conf. Proc.* **1144**(1), 109–113 (2009). <https://doi.org/10.1063/1.3169273>
- 4297
- 4298 R.M. Killen, A.E. Potter, P. Reiff, M. Sarantos, B.V. Jackson, P. Hick, B. Giles, Evidence for space weather at Mercury. *J. Geophys. Res., Planets* **106**(E9), 20,509–20,525 (2001). <https://doi.org/10.1029/2000JE001401>
- 4299
- 4300

- 4301 D. Lario, Advances in modeling gradual solar energetic particle events. *Adv. Space Res.* **36**(12), 2279–2288  
4302 (2005). <https://doi.org/10.1016/j.asr.2005.07.081>. Space Weather
- 4303 D. Lario, G.C. Ho, R.B. Decker, E.C. Roelof, M.I. Desai, C.W. Smith, ACE observations of energetic particles  
4304 associated with transient interplanetary shocks. *AIP Conf. Proc.* **679**(1), 640–643 (2003). <https://doi.org/10.1063/1.1618676>
- 4305 B. Lavraud, J.E. Borovsky, Altered solar wind-magnetosphere interaction at low Mach numbers: coronal  
4306 mass ejections. *J. Geophys. Res. Space Phys.* **113**(A9), A00B08 (2008). <https://doi.org/10.1029/2008JA013192>
- 4307 F. Leblanc, R. Johnson, Mercury exosphere I. Global circulation model of its sodium component. *Icarus*  
4308 **209**(2), 280–300 (2010). <https://doi.org/10.1016/j.icarus.2010.04.020>
- 4309 E. Liljeblad, T. Sundberg, T. Karlsson, A. Kullen, Statistical investigation of Kelvin–Helmholtz waves at the  
4310 magnetopause of Mercury. *J. Geophys. Res. Space Phys.* **119**(12), 9670–9683 (2014). <https://doi.org/10.1002/2014JA020614>
- 4311 S.T. Lindsay, M.K. James, E.J. Bunce, S.M. Imber, H. Korth, A. Martindale, T.K. Yeoman, MESSENGER  
4312 X-ray observations of magnetosphere–surface interaction on the nightside of Mercury. *Planet. Space Sci.*  
4313 **125**, 72–79 (2016). <https://doi.org/10.1016/j.pss.2016.03.005>
- 4314 S. Machida, Y. Saito, Y. Ito, H. Hayakawa, Instrumental characteristics of the Electron Spectrum Analyzer  
4315 (ESA) onboard the Planet-B mission and observational perspectives of the electron measurements. *Earth Planets Space* **50**(3), 207–211 (1998). <https://doi.org/10.1186/BF03352105>
- 4316 A. Marti, R. Schletti, P. Wurz, P. Bochsler, Calibration facility for solar wind plasma instrumentation. *Rev.*  
4317 *Sci. Instrum.* **72**(2), 1354–1360 (2001). <https://doi.org/10.1063/1.1340020>
- 4318 S. Massetti, S. Orsini, A. Milillo, A. Mura, E.D. Angelis, H. Lammer, P. Wurz, Mapping of the cusp plasma  
4319 precipitation on the surface of Mercury. *Icarus* **166**(2), 229–237 (2003). <https://doi.org/10.1016/j.icarus.2003.08.005>
- 4320 A. Masters, T.D. Phan, S.V. Badman, H. Hasegawa, M. Fujimoto, C.T. Russell, A.J. Coates, M.K. Dougherty,  
4321 The plasma depletion layer in Saturn’s magnetosheath. *J. Geophys. Res. Space Phys.* **119**(1), 121–130  
(2014). <https://doi.org/10.1002/2013JA019516>
- 4322 A. Milillo, P. Wurz, S. Orsini, D. Delcourt, E. Kallio, R.M. Killen, H. Lammer, S. Massetti, A. Mura,  
4323 S. Barabash, G. Cremonese, I.A. Daglis, E. De Angelis, A.M. Di Lellis, S. Livi, V. Mangano, K. Torkar,  
4324 Surface–exosphere–magnetosphere system of Mercury. *Space Sci. Rev.* **117**(3), 397–443 (2005). <https://doi.org/10.1007/s11214-005-3593-z>
- 4325 T. Mitani, T. Takashima, S. Kasahara, W. Miyake, M. Hirahara, High-energy electron experiments (HEP)  
4326 aboard the ERG (ARASE) satellite. *Earth Planets Space* **70**(1), 77 (2018). <https://doi.org/10.1186/s40623-018-0853-1>
- 4327 W. Miyake, Y. Saito, M. Harada, M. Saito, H. Hasegawa, A. Ieda, S. Machida, T. Nagai, T. Nagatsuma,  
4328 K. Seki, I. Shinohara, T. Terasawa, Mercury Ion Analyzer (MIA) onboard Mercury Magnetospheric  
4329 Orbiter: MMO. *Adv. Space Res.* **43**(12), 1986–1992 (2009). <https://doi.org/10.1016/j.asr.2009.03.011>
- 4330 T. Mukai, K. Ogasawara, Y. Saito, An empirical model of the plasma environment around Mercury. *Adv.*  
4331 *Space Res.* **33**(12), 2166–2171 (2004). [https://doi.org/10.1016/S0273-1177\(03\)00443-5](https://doi.org/10.1016/S0273-1177(03)00443-5). Mercury, Mars  
4332 and Saturn
- 4333 D. Müller, R.G. Marsden, O.C. St Cyr, H.R. Gilbert (TSO Team), Solar orbiter. *Sol. Phys.* **285**(1), 25–70  
4334 (2013). <https://doi.org/10.1007/s11207-012-0085-7>
- 4335 A. Mura, P. Wurz, H.I. Lichtenegger, H. Schleicher, H. Lammer, D. Delcourt, A. Milillo, S. Orsini, S. Mas-  
4336 setti, M.L. Khodachenko, The sodium exosphere of Mercury: comparison between observations during  
4337 Mercury’s transit and model results. *Icarus* **200**(1), 1–11 (2009). <https://doi.org/10.1016/j.icarus.2008.11.014>
- 4338 T.K.M. Nakamura, H. Hasegawa, W. Daughton, S. Eriksson, W.Y. Li, R. Nakamura, Turbulent mass transfer  
4339 caused by vortex induced reconnection in collisionless magnetospheric plasmas. *Nat. Commun.* **8**(1),  
4340 1582 (2017). <https://doi.org/10.1038/s41467-017-01579-0>
- 4341 N.F. Ness, K.W. Behannon, R.P. Lepping, Y.C. Whang, K.H. Schatten, Magnetic field observations near  
4342 Mercury: preliminary results from Mariner 10. *Science* **185**(4146), 151–160 (1974). <https://doi.org/10.1126/science.185.4146.151>
- 4343 M.N. Nishino, M. Fujimoto, T.D. Phan, T. Mukai, Y. Saito, M.M. Kuznetsova, L. Rastätter, Anomalous flow  
4344 deflection at Earth’s low-Alfvén-Mach-number bow shock. *Phys. Rev. Lett.* **101**, 065,003 (2008). <https://doi.org/10.1103/PhysRevLett.101.065003>
- 4345 K.W. Ogilvie, J.D. Scudder, R.E. Hartle, G.L. Siscoe, H.S. Bridge, A.J. Lazarus, J.R. Asbridge, S.J. Bame,  
4346 C.M. Yeates, Observations at Mercury encounter by the plasma science experiment on Mariner 10.  
4347 *Science* **185**(4146), 145–151 (1974). <https://doi.org/10.1126/science.185.4146.145>
- 4348 M. Oka, F. Otsuka, S. Matsukiyo, L.B. Wilson, M.R. Argall, T. Amano, T.D. Phan, M. Hoshino, O.L. Con-  
4349 tel, D.J. Gershman, J.L. Burch, R.B. Torbert, J.C. Dorelli, B.L. Giles, R.E. Ergun, C.T. Russell,  
4350 P.A. Lindqvist, Electron scattering by low-frequency whistler waves at Earth’s bow shock. *Astrophys. J.* **886**(1), 53 (2019). <https://doi.org/10.3847/1538-4357/ab4a81>

- 4351 E. Parker, Dynamics of the interplanetary gas and magnetic fields. *Astrophys. J.* **128**, 664 (1958). <https://doi.org/10.1086/146579>
- 4352 Y. Saito, J. Sauvaud, M. Hirahara, S. Barabash, D. Delcourt, T. Takashima, K. Asamura, Scientific objectives and instrumentation of Mercury Plasma Particle Experiment (MPPE) onboard MMO. *Planet. Space Sci.* **58**(1), 182–200 (2010a). <https://doi.org/10.1016/j.pss.2008.06.003>. Comprehensive Science Investigations of Mercury: The Scientific Goals of the Joint ESA/JAXA Mission BepiColombo
- 4353 Y. Saito, S. Yokota, K. Asamura, T. Tanaka, M.N. Nishino, T. Yamamoto, Y. Terakawa, M. Fujimoto, H. Hasegawa, H. Hayakawa, M. Hirahara, M. Hoshino, S. Machida, T. Mukai, T. Nagai, T. Nagatsuma, T. Nakagawa, M. Nakamura, Ki. Oyama, E. Sagawa, S. Sasaki, K. Seki, I. Shinohara, T. Terasawa, H. Tsunakawa, H. Shibuya, M. Matsushima, H. Shimizu, F. Takahashi, In-flight performance and initial results of Plasma Energy Angle and Composition Experiment (PACE) on SELENE (Kaguya). *Space Sci. Rev.* **154**(1), 265–303 (2010b). <https://doi.org/10.1007/s11214-010-9647-x>
- 4354 Y. Saito, S. Yokota, K. Asamura, A. Krieger, High-speed MCP anodes for high time resolution low-energy charged particle spectrometers. *J. Geophys. Res. Space Phys.* **122**(2), 1816–1830 (2017). <https://doi.org/10.1002/2016JA023157>
- 4355 M. Sarantos, J.A. Slavin, On the possible formation of Alfvén wings at Mercury during encounters with coronal mass ejections. *Geophys. Res. Lett.* **36**(4), L04107 (2009). <https://doi.org/10.1029/2008GL036747>
- 4356 J.A. Sauvaud, A. Fedorov, C. Aoustin, H.C. Seran, E.L. Comte, M. Petiot, J. Rouzaud, Y. Saito, J. Dandouras, C. Jacquy, P. Louarn, C. Mazelle, J.L. Médale, The Mercury electron analyzers for the Bepi Colombo mission. *Adv. Space Res.* **46**(9), 1139–1148 (2010). <https://doi.org/10.1016/j.asr.2010.05.022>
- 4357 D. Schriver, P.M. Trávníček, B.J. Anderson, M. Ashour-Abdalla, D.N. Baker, M. Benna, S.A. Boardsen, R.E. Gold, P. Hellinger, G.C. Ho, H. Korth, S.M. Krimigis, R.L. McNutt Jr., J.M. Raines, R.L. Richard, J.A. Slavin, S.C. Solomon, R.D. Starr, T.H. Zurbuchen, Quasi-trapped ion and electron populations at Mercury. *Geophys. Res. Lett.* **38**(23), L23103 (2011). <https://doi.org/10.1029/2011GL049629>
- 4358 N. Shimada, T. Terasawa, M. Hoshino, T. Naito, H. Matsui, T. Koi, K. Maezawa, Diffusive shock acceleration of electrons at an interplanetary shock observed on 21 Feb 1994. *Astrophys. Space Sci.* **264**(1), 481–488 (1998). <https://doi.org/10.1023/A:1002499513777>
- 4359 I. Shinohara, M. Fujimoto, Formation of thin electron current layer associated with lower hybrid drift instability and its relation to quick reconnection triggering, in *Frontiers in Magnetospheric Plasma Physics*, ed. by M. Hoshohino, Y. Omura, L. Lanzerotti. COSPAR Colloquia Series, vol. 16 (Pergamon, Elmsford, 2005), pp. 123–129. [https://doi.org/10.1016/S0964-2749\(05\)80019-8](https://doi.org/10.1016/S0964-2749(05)80019-8)
- 4360 P. Sigmund, A. Oliva, G. Falcone, Sputtering of multicomponent materials: elements of a theory. *Nucl. Instrum. Methods Phys. Res.* **194**(1), 541–548 (1982). [https://doi.org/10.1016/0029-554X\(82\)90578-X](https://doi.org/10.1016/0029-554X(82)90578-X)
- 4361 J. Simpson, J. Eraker, J. Lamport, P. Walpole, Electrons and protons accelerated in Mercury’s magnetic field. *Science* **185**, 160–166 (1974). <https://doi.org/10.1126/science.185.4146.160>
- 4362 J. Slavin, Mercury’s magnetosphere. *Adv. Space Res.* **33**(11), 1859–1874 (2004). <https://doi.org/10.1016/j.asr.2003.02.019>. Comparative Magnetospheres
- 4363 J.A. Slavin, S.M. Imber, S.A. Boardsen, G.A. DiBraccio, T. Sundberg, M. Sarantos, T. Nieves-Chinchilla, A. Szabo, B.J. Anderson, H. Korth, T.H. Zurbuchen, J.M. Raines, C.L. Johnson, R.M. Winslow, R.M. Killen, R.L. McNutt Jr., S.C. Solomon, MESSENGER observations of a flux-transfer-event shower at Mercury. *J. Geophys. Res. Space Phys.* **117**(A12), A00M06 (2012). <https://doi.org/10.1029/2012JA017926>
- 4364 J.A. Slavin, D.N. Baker, D.J. Gershman, G.C. Ho, S.M. Imber, S.M. Krimigis, T. Sundberg, Mercury’s dynamic magnetosphere, in *Mercury: The View After MESSENGER*. Cambridge Planetary Science (Cambridge University Press, Cambridge, 2018), pp. 461–496. <https://doi.org/10.1017/9781316650684.018>
- 4365 J.A. Slavin, H.R. Middleton, J.M. Raines, X. Jia, J. Zhong, W.J. Sun, S. Livi, S.M. Imber, G.K. Poh, M. Akhavan-Tafti, J. Jasinski, G.A. DiBraccio, C. Dong, R.M. Dewey, M.L. Mays, MESSENGER observations of disappearing dayside magnetosphere events at Mercury. *J. Geophys. Res. Space Phys.* **124**(8), 6613–6635 (2019). <https://doi.org/10.1029/2019JA026892>
- 4366 D.F. Smart, M.A. Shea, A simplified model for timing the arrival of solar flare-initiated shocks. *J. Geophys. Res. Space Phys.* **90**(A1), 183–190 (1985). <https://doi.org/10.1029/JA090iA01p00183>
- 4367 W.J. Sun, J.M. Raines, S.Y. Fu, J.A. Slavin, Y. Wei, G.K. Poh, Z.Y. Pu, Z.H. Yao, Q.G. Zong, W.X. Wan, MESSENGER observations of the energization and heating of protons in the near-Mercury magnetotail. *Geophys. Res. Lett.* **44**(16), 8149–8158 (2017). <https://doi.org/10.1002/2017GL074276>
- 4368 B.T. Tsurutani, R.P. Lin, Acceleration of > 47 keV ions and > 2 keV electrons by interplanetary shocks at 1 AU. *J. Geophys. Res. Space Phys.* **90**(A1), 1–11 (1985). <https://doi.org/10.1029/JA090iA01p00001>
- 4369 P. van Nes, R. Reinhard, T.R. Sanderson, K.P. Wenzel, R.D. Zwickl, The energy spectrum of 35- to 1600-keV protons associated with interplanetary shocks. *J. Geophys. Res. Space Phys.* **89**(A4), 2122–2132 (1984). <https://doi.org/10.1029/JA089iA04p02122>
- 4370 C. Wang, D. Du, J.D. Richardson, Characteristics of the interplanetary coronal mass ejections in the heliosphere between 0.3 and 5.4 AU. *J. Geophys. Res. Space Phys.* **110**(A10), A10107 (2005). <https://doi.org/10.1029/2005JA011198>

- 4401 S. Watanabe, H. Tajima, Y. Fukazawa, Y. Ichinohe, S. Takeda, T. Enoto, T. Fukuyama, S. Furui, K. Genba,  
4402 K. Hagino, A. Harayama, Y. Kuroda, D. Matsuura, R. Nakamura, K. Nakazawa, H. Noda, H. Odaka,  
4403 M. Ohta, M. Onishi, S. Saito, G. Sato, T. Sato, T. Takahashi, T. Tanaka, A. Togo, S. Tomizuka, The  
4404 Si/CdTe semiconductor Compton camera of the ASTRO-H Soft Gamma-Ray Detector (SGD). *Nucl.*  
4405 *Instrum. Methods Phys. Res., Sect. A, Accel. Spectrom. Detect. Assoc. Equip.* **765**, 192–201 (2014).  
4406 <https://doi.org/10.1016/j.nima.2014.05.127>. hSTD-9 2013—Proceedings of the 9th International Hi-  
4407 roshima Symposium on Development and Application of Semiconductor Tracking Detectors  
4408 Y.C. Whang, Magnetospheric magnetic field of Mercury. *J. Geophys. Res.* **82**(7), 1024–1030 (1977). <https://doi.org/10.1029/JA082i007p01024>  
4409 M. Wieser, P. Wurz, Production of a 10 eV–1000 eV neutral particle beam using surface neutralization. *Meas.*  
4410 *Sci. Technol.* **16**(12), 2511–2516 (2005). <https://doi.org/10.1088/0957-0233/16/12/016>  
4411 R.M. Winslow, B.J. Anderson, C.L. Johnson, J.A. Slavin, H. Korth, M.E. Purucker, D.N. Baker,  
4412 S.C. Solomon, Mercury’s magnetopause and bow shock from MESSENGER magnetometer observations.  
4413 *J. Geophys. Res. Space Phys.* **118**(5), 2213–2227 (2013). <https://doi.org/10.1002/jgra.50237>  
4414 R.M. Winslow, N. Lugaz, L.C. Philpott, N.A. Schwadron, C.J. Farrugia, B.J. Anderson, C.W. Smith, Inter-  
4415 planetary coronal mass ejections from MESSENGER orbital observations at Mercury. *J. Geophys. Res.*  
4416 *Space Phys.* **120**(8), 6101–6118 (2015). <https://doi.org/10.1002/2015JA021200>  
4417 M. Wüest, D. Evans, ISS Institute, R. von Steiger, ES Agency, *Calibration of Particle Instruments in Space*  
4418 *Physics*. ESA SR, ISSI (2007). The International Space Science Institute. [https://books.google.co.jp/](https://books.google.co.jp/books?id=hmbKNAACA AJ)  
4419 [books?id=hmbKNAACA AJ](https://books.google.co.jp/books?id=hmbKNAACA AJ)  
4420 P. Wurz, H. Lammer, Monte-Carlo simulation of Mercury’s exosphere. *Icarus* **164**(1), 1–13 (2003). [https://doi.org/10.1016/S0019-1035\(03\)00123-4](https://doi.org/10.1016/S0019-1035(03)00123-4)  
4421 M. Yagi, K. Seki, Y. Matsumoto, D.C. Delcourt, F. Leblanc, Formation of a sodium ring in Mercury’s  
4422 magnetosphere. *J. Geophys. Res. Space Phys.* **115**(A10), A10253 (2010). [https://doi.org/10.1029/](https://doi.org/10.1029/2009JA015226)  
4423 [2009JA015226](https://doi.org/10.1029/2009JA015226)  
4424 M. Yagi, K. Seki, Y. Matsumoto, D.C. Delcourt, F. Leblanc, Global structure and sodium ion dynamics in  
4425 Mercury’s magnetosphere with the offset dipole. *J. Geophys. Res. Space Phys.* **122**(11), 10,990–11,002  
4426 (2017). <https://doi.org/10.1002/2017JA024082>  
4427 D.T. Young, J.J. Berthelier, M. Blanc, J.L. Burch, A.J. Coates, R. Goldstein, M. Grande, T.W. Hill, R.E. John-  
4428 son, V. Kelha, D.J. Mccomas, E.C. Sittler, K.R. Svenes, K. Szegő, P. Tanskanen, K. Ahola, D. Anderson,  
4429 S. Bakshi, R.A. Baragiola, B.L. Barraclough, R.K. Black, S. Bolton, T. Booker, R. Bowman, P. Casey,  
4430 F.J. Crary, D. Delapp, G. Dirks, N. Eaker, H. Funsten, J.D. Furman, J.T. Gosling, H. Hannula, C. Holm-  
4431 lund, H. Huomo, J.M. Illiano, P. Jensen, M.A. Johnson, D.R. Linder, T. Luntama, S. Maurice, K.P. Mc-  
4432 cabee, K. Mursula, B.T. Narheim, J.E. Nordholt, A. Preece, J. Rudzki, A. Ruitberg, K. Smith, S. Szalai,  
4433 M.F. Thomsen, K. Viherkanto, J. Vilppola, T. Vollmer, T.E. Wahl, M. Wüest, T. Ylikorpi, C. Zinsmeyer,  
4434 Cassini plasma spectrometer investigation. *Space Sci. Rev.* **114**(1), 1–112 (2004). <https://doi.org/10.1007/s11214-004-1406-4>  
4435 T.H. Zurbuchen, J.M. Raines, J.A. Slavin, D.J. Gershman, J.A. Gilbert, G. Gloeckler, B.J. Anderson,  
4436 D.N. Baker, H. Korth, S.M. Krimigis, M. Sarantos, D. Schriver, R.L. McNutt, S.C. Solomon, MES-  
4437 SENDER observations of the spatial distribution of planetary ions near Mercury. *Science* **333**(6051),  
4438 1862–1865 (2011). <https://doi.org/10.1126/science.1211302>

4435 **Publisher’s Note** Springer Nature remains neutral with regard to jurisdictional claims in published maps and  
4436 institutional affiliations.

## 4437 Authors and Affiliations

4441 Yoshifumi Saito<sup>1</sup>  · Dominique Delcourt<sup>2</sup> · Masafumi Hirahara<sup>3</sup> · Stas Barabash<sup>4</sup> ·  
4442 Nicolas André<sup>5</sup> · Takeshi Takashima<sup>1</sup> · Kazushi Asamura<sup>1</sup> · Shoichiro Yokota<sup>6</sup> ·  
4443 Martin Wieser<sup>4</sup> · Masaki N. Nishino<sup>1</sup> · Mitsuo Oka<sup>7</sup> · Yoshifumi Futaana<sup>4</sup> ·  
4444 Yuki Harada<sup>8</sup> · Jean-André Sauvaud<sup>5</sup> · Philippe Louarn<sup>5</sup> · Benoit Lavraud<sup>5</sup> ·  
4445 Vincent Génot<sup>5</sup> · Christian Mazelle<sup>5</sup> · Iannis Dandouras<sup>5</sup> · Christian Jacquety<sup>5</sup> ·  
4446 Claude Aoustin<sup>5</sup> · Alain Barthe<sup>9</sup> · Alexandre Cadu<sup>10</sup> · Andréi Fedorov<sup>5</sup> ·  
4447 Anne-Marie Frezoul<sup>11</sup> · Catherine Garat<sup>12</sup> · Eric Le Comte<sup>5</sup> · Qiu-Mei Lee<sup>5</sup> ·  
4448 Jean-Louis Médale<sup>5</sup> · David Moirin<sup>12</sup> · Emmanuel Penou<sup>5</sup> · Mathieu Petiot<sup>5</sup> ·  
4449 Guy Peyre<sup>13</sup> · Jean Rouzaud<sup>5</sup> · Henry-Claude Séran<sup>5</sup> · Zdeněk Němeček<sup>14</sup> ·  
4450

4451 **Jana Šafránková<sup>14</sup> · Maria Federica Marucci<sup>15</sup> · Roberto Bruno<sup>15</sup> ·**  
4452 **Giuseppe Consolini<sup>15</sup> · Wataru Miyake<sup>16</sup> · Iku Shinohara<sup>1</sup> · Hiroshi Hasegawa<sup>1</sup> ·**  
4453 **Kanako Seki<sup>17</sup> · Andrew J. Coates<sup>18</sup> · Frédéric Leblanc<sup>2</sup> · Christophe Verdeil<sup>5</sup> ·**  
4454 **Bruno Katra<sup>2</sup> · Dominique Fontaine<sup>19</sup> · Jean-Marie Illiano<sup>2</sup> · Jean-Jacques Berthelie<sup>20</sup> ·**  
4455 **Jean-Denis Techer<sup>2</sup> · Markus Fraenz<sup>21</sup> · Henning Fischer<sup>21</sup> · Norbert Krupp<sup>21</sup> ·**  
4456 **Joachim Woch<sup>21</sup> · Ulrich Bührke<sup>21</sup> · Björn Fiethe<sup>22</sup> · Harald Michalik<sup>22</sup> ·**  
4457 **Haruhisa Matsumoto<sup>23</sup> · Tomoki Yanagimachi<sup>24</sup> · Yoshizumi Miyoshi<sup>3</sup> ·**  
4458 **Takefumi Mitani<sup>1</sup> · Manabu Shimoyama<sup>4</sup> · Qiugang Zong<sup>25</sup> · Peter Wurz<sup>26</sup> ·**  
4459 **Herman Andersson<sup>4</sup> · Stefan Karlsson<sup>4</sup> · Mats Holmström<sup>4</sup> · Yoichi Kazama<sup>27</sup> ·**  
4460 **Wing-Huen Ip<sup>28</sup> · Masahiro Hoshino<sup>17</sup> · Masaki Fujimoto<sup>1</sup> · Naoki Terada<sup>29</sup> ·**  
4461 **Kunihiro Keika<sup>17</sup> · BepiColombo Mio/MPPE Team<sup>30</sup>**

4462 ✉ Y. Saito  
4463 [saito@stp.isas.jaxa.jp](mailto:saito@stp.isas.jaxa.jp)  
4464

- 4465 1 Institute of Space and Astronautical Science, Japan Aerospace Exploration Agency,  
4466 3-1-1 Yoshinodai, Chuo, Sagamihara, Kanagawa 252-5210, Japan
- 4467 2 LPP-CNRS-Sorbonne Université-Ecole Polytechnique, 4 place Jussieu, 75252 Paris, France
- 4468 3 ISEE, Nagoya University, Furo-cho, Chikusa-ku, Nagoya 464-8601, Japan
- 4469 4 Swedish Institute of Space Physics, Box 812, 98128, Kiruna, Sweden
- 4470 5 IRAP, CNRS, UPS, CNES, Université de Toulouse, 9, avenue du Colonel Roche, 31028 Toulouse,  
4471 France
- 4472 6 Osaka University, 1-1 Machikaneyama-cho, Toyonaka-shi, Osaka 560-0043, Japan
- 4473 7 Space Sciences Laboratory, University of California, Berkeley, 7 Gauss Way, Berkeley, CA 94720,  
4474 USA
- 4475 8 Kyoto University, Kitashirakawa Oiwakecho, Sakyo-ku, Kyoto, 606-8502, Japan
- 4476 9 AKKA Technologies, Toulouse, France
- 4477 10 ISAE, Toulouse, France
- 4478 11 Microtec, groupe AGORA Industries, Labège, France
- 4479 12 NEXEYA, Toulouse, France
- 4480 13 COMAT, groupe AGORA Industries, Flourens, France
- 4481 14 Faculty of Mathematics and Physics, Charles University, V Holešovičkách 2, 180 00 Prague 8,  
4482 Czech Republic
- 4483 15 INAF, Istituto di Astrofisica e Planetologia Spaziali, Roma, Italy
- 4484 16 Tokai University, 4-1-1 Kitakaname, Hiratsuka-shi, Kanagawa, Japan
- 4485 17 University of Tokyo, 7-3-1 Hongo, Bunkyo, Tokyo 113-0033, Japan
- 4486 18 MSSL, University College London, Holmbury St Mary, Dorking RH5 6NT, UK
- 4487 19 LPP-CNRS-Ecole Polytechnique-Sorbonne Université, Route de Saclay, 91128 Palaiseau, France
- 4488 20 LATMOS-CNRS-IPSL, 4 place Jussieu, 75252 Paris, France
- 4489 21 MPS, Justus-von-Liebig Weg 3, 37077 Goettingen, Germany
- 4490 22 IDA, Hans-Sommer-Str. 66, 38106 Braunschweig, Germany
- 4491 23 JAXA, Sengen 2chome, Tsukuba, Ibaraki 305-8505, Japan
- 4492 24 Rikkyo University, 3-34-1 Nishi-Ikebukuro, Toshima-ku, Tokyo 171-8501, Japan
- 4493 25 Peking University, North Physics Building, Peking University, Beijing, 100871, China
- 4494 26 University of Bern, 3012, Bern, Switzerland
- 4495
- 4500

- 4501 27 Academia Sinica Institute of Astronomy and Astrophysics, No. 1, Sect. 4, Roosevelt Rd,  
4502 Taipei 10617, Taiwan
- 4503 28 IASS, National Central University, Chung-Li, 32054 Taiwan
- 4504 29 Tohoku University, Aramaki-aza-aoba, Aoba-ku, Sendai, Miyagi 980-8578, Japan
- 4505 30 <https://www.cosmos.esa.int/web/bepicolombo/mppe>
- 4506
- 4507
- 4508
- 4509
- 4510
- 4511
- 4512
- 4513
- 4514
- 4515
- 4516
- 4517
- 4518
- 4519
- 4520
- 4521
- 4522
- 4523
- 4524
- 4525
- 4526
- 4527
- 4528
- 4529
- 4530
- 4531
- 4532
- 4533
- 4534
- 4535
- 4536
- 4537
- 4538
- 4539
- 4540
- 4541
- 4542
- 4543
- 4544
- 4545
- 4546
- 4547
- 4548
- 4549
- 4550

UNCORRECTED PROOF